POLARIMETRIC DECOMPOSITION BASED ON GENERAL CHARACTERISATION OF SCATTERING FROM URBAN AREAS AND MULTIPLE COMPONENT SCATTERING MODEL

RUCHI VERMA
 March, 2012

SUPERVISORS:
Mr. Shashi Kumar
Dr. Valentyn Tolpekin
Mr. P. L. N. Raju

POLARIMETRIC DECOMPOSITION BASED ON GENERAL CHARACTERISATION OF SCATTERING FROM URBAN AREAS AND MULTIPLE COMPONENT SCATTERING MODEL
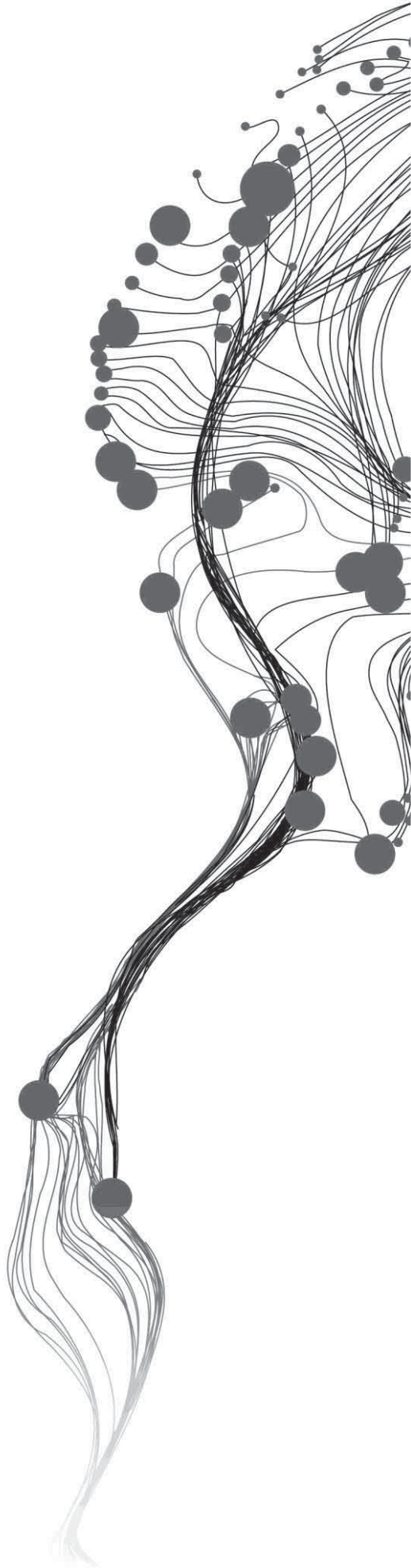
RUCHI VERMA
Enschede, The Netherlands, March, 2012

Thesis submitted to the Faculty of Geo-Information Science and Earth Observation of the University of Twente in partial fulfilment of the requirements for the degree of Master of Science in Geo-information Science and Earth Observation.
Specialization: Geoinformatics

SUPERVISORS:
Mr. Shashi Kumar
Dr. Valentyn Tolpekin
Mr. P. L. N. Raju

THESIS ASSESSMENT BOARD:
Dr. Ir. A. Stein (Chair)
Dr. Y. S. Rao (External Examiner, CSRE, IIT Bombay)

ABSTRACT

A generalised polarimetric decomposition approach for polarimetric backscatter from urban areas has been presented in this research. This approach takes into account the random orientation of the scatterers along the radar line of sight, especially in urban areas. The assumption of reflection symmetry on which the decomposition models for natural distributed areas are based, is not exhibited by urban areas. An oriented urban scatterer induces polarisation orientation angle shifts and display high response in cross-polarisation channel, which is characteristic of vegetation or canopy surface. This results in overestimation of the volume scattering power from the urban areas. A cosine squared function was used to describe the orientation of the urban scatters. Each basic scattering matrix, representing the elementary scattering mechanisms observed from different targets, was rotated by orientation angle θ around the radar line of sight. The cosine squared distribution was employed as a probability density function on the basic matrices. The coherency matrix, obtained from each basic scattering matrix, was utilised for decomposition approach for its higher sensitivity to the orientation and phase of the backscatter as well as easier physical interpretation. The Multiple Component Scattering Model decomposition was used in this research. It describes the total backscatter as a linear sum of five types of basic scattering mechanisms – surface, double bounce, volume, helix and wire scattering. This decomposition is applicable for both reflection symmetric and reflection asymmetric conditions. The urban areas are known to generate high returns in double bounce, helix and wire scattering. The ALOS PALSAR L-Band fully polarimetric data was utilised in this research for the complete analysis of the backscatter. The decomposed results obtained from the given approach were compared with the decomposition results from the deorientation technique, given by Yamaguchi using the rotation of coherency matrix, and from direct decomposition without compensating the orientation angle shifts. As expected the double bounce scattering from the urban scatterers were found to be increased, along with the decrease in the volume scattering component. The response of the various features in the decomposition utilising the cosine squared distribution was investigated. The relation of the co-pol and cross-pol response with the five scattering components was also analysed. The presented decomposition approach can be employed as a general decomposition approach which can be applied to urban areas as well as natural areas. Further improvement and development of this approach can enhance the applications of SAR Polarimetry for the urban areas.

Keywords: *SAR Polarimetry, Multiple Component Scattering Model, polarimetric decomposition, polarization orientation angle, cosine squared distribution, urban areas, coherency matrix.*

ACKNOWLEDGEMENTS

TABLE OF CONTENTS

LIST OF FIGURES

LIST OF TABLES

1. INTRODUCTION

The advancement of earth observation science has opened new avenues of research in the field of earth sciences. The observation satellites, with their unique global perspective, offer interesting possibilities for better understanding of the earth's precious environment. In the age of gradually degrading environmental conditions, climate change, rising population and vanishing resources, remote sensing has emerged as a powerful technology for acquiring information about these changes, identifying the key factors, spatial pattern and extent of the prevailing problems and their possible solutions. Observations acquired by such satellites often identify significant patterns and problems, which can easily go unnoticed from the ground. Remote sensing also provides an advantage of capturing information of inaccessible areas and its regular revision. Remote sensing offers tremendous opportunities for regular monitoring and management of resources and assists in sound decision making.

Remote Sensing utilizes the visible, infra-red and microwave region of the electromagnetic spectrum. The visible and infra-red regions (0.3-15 μm) are known as optical regions, and the microwave region (1 mm-1.3 m) is considered as non-optical region. Systems operating in optical region are being used for several decades and therefore, are more advanced and widely employed. However, their use is limited by availability of sunlight and interference of the atmospheric conditions such as haze and cloud cover especially in the tropical regions. Therefore, the use of microwave or radar remote sensing is preferred in such areas.

RADAR stands for 'Radio Detection And Ranging'. With their large spatial coverage and relatively high revisiting frequency, these systems offer interesting possibilities for various applications. Active radar remote sensing utilizes its own source of energy to illuminate the target and therefore it is not limited to day time. Radar wave is not affected much by atmospheric conditions and provides a different aspect of information of the Earth surface than that provided by optical sensors as it is sensitive to the surface properties like roughness, dielectric constant and moisture content. Advanced Radar Systems such as Polarimetric SAR, Interferometric SAR and Differential Interferometric SAR have further enhanced the information retrieval capabilities of Radar.

The radar system employs an antenna to transmit a radar signal in side looking direction with respect to the flight path, towards the earth feature and then record the backscattered signal from the earth feature. In case of a Real Aperture Radar (RAR) System, where aperture is the antenna, the amplitude of the each return signal is measured. The resolution of such systems is directly proportional to the length of the antenna. As it is impractical to utilize a very long physical antenna to enhance the resolution, Synthetic Aperture Radar (SAR) system was developed which can synthesize the effect of a long physical antenna through modified data recording and processing techniques[1].

1.1. Polarisation

Polarisation is an important property of an electromagnetic wave. An electromagnetic wave is formed by two time-varying components, electric field component and magnetic field component, which are orthogonal to each other as well as to the direction of propagation of the wave. Polarisation can be defined as the orientation and regularity of the electric or magnetic field component, in a plane orthogonal to the direction of propagation of the wave. As the magnetic field component is always perpendicular to

the electric field component, therefore only the latter is used for describing the polarisation of an electromagnetic wave.
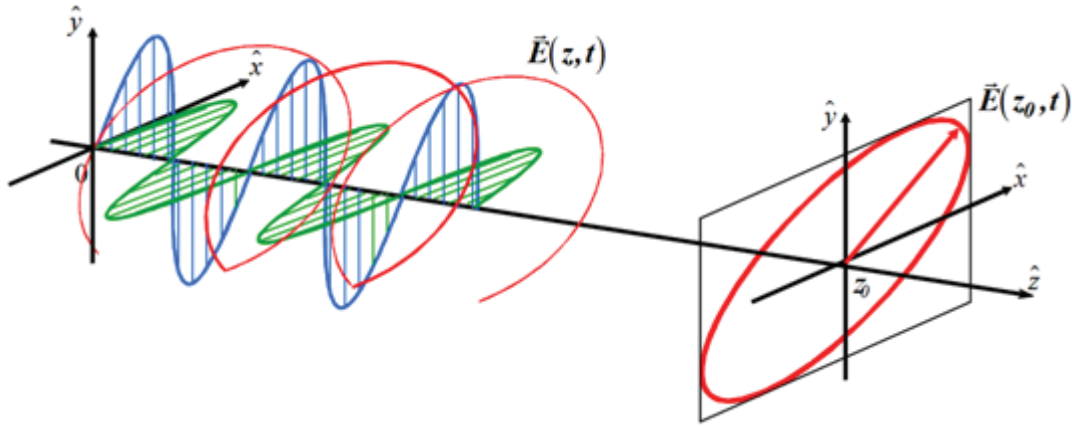
Figure 1-1 Propagation of an electromagnetic plane wave[2]

The blue and the green waves in the Figure 1-1, represent the horizontal and vertical components of the electric field, respectively. These components combine to form the net electric field vector represented by the red wave. The electric field vector of a fully polarised wave traces out a regular pattern, when visualised along the direction of propagation of the wave, which is generally an ellipse known as polarisation ellipse.
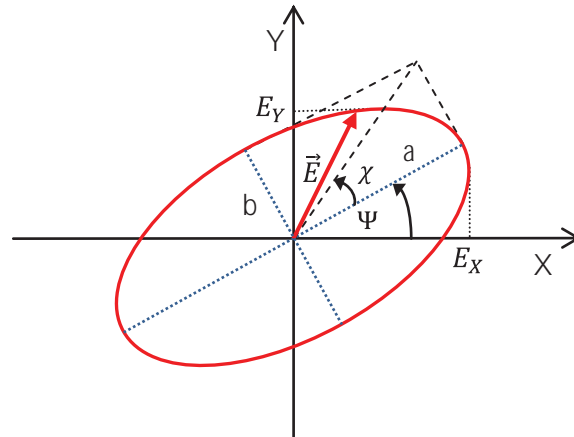
Figure 1-2 Polarisation Ellipse[2]

A polarisation ellipse is characterised by the amplitude of the wave, the orientation and the ellipticity. The amplitude of the wave is represented by the length of the electric field vector and the frequency of the wave is represented by the rate of rotation of the vector. In the above figure, a polarisation ellipse is shown with a semi-major axis of length a and a semi-minor axis of length b. Here, $\vec{E}$ denotes the electric field vector, E_X and E_Y are the horizontal and vertical components of the electric field. The angle made by the major axis of polarization ellipse, measured counter clockwise from the positive horizontal axis on the incident plane is known as the orientation angle 'Ψ' of the electromagnetic wave, which ranges between 0° to 180°. The ellipticity is a shape parameter, given by the angle 'χ' which varies from -45° to +45° and which describes the degree to which the shape of the ellipse is oval. The magnitudes and the relative phase between the two components of the electric field regulate the shape of the polarisation ellipse traced by it. On the basis of the orientation and the ellipticity, polarisation can be categorised into

linear, circular and elliptical. In case of the linear polarisation, the two components of the electric field are in phase, and the ellipticity (χ) is zero and the orientation is 45°. When the relative phase increases to $\pi/2$ radians and the ellipticity increases to 45°, with orientation remaining same at 45°, the polarisation is termed as circular polarisation. Other than these two cases, rest all is considered as elliptical polarisation [2]

1.2.   SAR Polarimetry

A SAR system illuminates continuous strips of earth's surface along one side of the flight direction. The radar signal reflected back from the earth's surface in the direction of the radar sensor is recorded. The radar antenna records the strength and the time delay of these return signals. Signal processing is required to produce radar images from this recorded signal data [3]. SAR system utilises specially designed antenna to transmit and receive a radar wave of a specific polarisation. For convenience, horizontal (H) and vertical (V) orientations are preferred for SAR systems and the channels are represented as HH for horizontal transmit and horizontal receive and HV for horizontal transmit and vertical receive. Here HH is termed as like polarized or co-pol channel and HV is termed as cross-polarized or cross-pol channel. Such SAR systems can have three levels of polarization complexity:

- Single polarized - either HH or VV or HV or VH
- Dual polarized – (HH and VV) or (HH and HV) or (HV and VV)
- Full or quad polarized – All four channels are present – HH, VV, HV, VH

Full or quad polarimetric mode preserves the full vector nature of the electromagnetic radiations and therefore, is preferred for complete analysis of the backscatter. A fully polarimetric SAR system also measures the phase difference between different polarization channels which plays an important role in polarimetric information extraction [2].

SAR polarimetry deals with the full vector nature of the electromagnetic waves. The information about the target surface can be retrieved on the basis of its response in different polarisation states.When a polarized radar wave interacts with the earth's surface, the polarization of the wave is modified depending upon the specific characteristics of the surface. This includes its geometrical structure, shape, reflectivity, orientation as well as the geophysical properties such as moisture content, surface roughness etc. [4] Therefore, the backscattered radar wave has a different polarization than that of the incident wave. Due to this reason, earth features give different response in different polarization channels and on the basis of this response, various earth features can be identified from the radar image. Features such as ice, ocean waves, soil moisture, vegetation, geological features and man-made structures are better detected in polarimetric radar images as compared to images acquired by optical sensors [3].

The polarimetric information of the target surface is stored in form of scattering matrix. The information about the pure or isolated scatterers can be directly extracted using the scattering matrix whereas for distributed scatterers, the second order statistics of the scattering matrix i.e., covariance or coherency matrix are employed which stores the complex information about the targets.

1.3.   Scattering, Covariance & Coherency Matrix

A radar wave of a specific polarization, when interacts with the target surface, experiences change in its polarization state. The wave reradiated from the target surface after this interaction will have response not

only in horizontal polarization but also in vertical polarization as well [5]. In terms of SAR polarimetry, these responses from the backscattered wave in each polarization channel are stored in the form of 2×2 scattering matrix given by

$$[S] = \begin{bmatrix} S_{HH} & S_{HV} \\ S_{VH} & S_{VV} \end{bmatrix} \qquad (1\text{-}1)$$

where each element of the matrix represents the backscatter response of the target in a particular polarization channel. The diagonal elements of the matrix represents the co-pol information, i.e. the transmitted and received radar wave have same polarization, and the off diagonal terms represents the cross-pol information, i.e. the transmitted and received radar wave have polarization orthogonal to each other. The scattering matrix describes the information of the pure target exhibiting a particular scattering mechanism. However in general, the earth features are more complex or distributed demonstrating a variety of scattering response. In such case, the information obtained from the scattering matrix is insufficient to describe the physical properties of the surface. Therefore, the second order statistics of the scattering matrix – covariance and coherency matrix, are utilized for this purpose. These matrices are obtained from the scattering matrix by using its vectorized form derived from Pauli and Lexicographic basis [2].

The lexicographic vector form assuming the reciprocity condition $S_{HV} = S_{VH}$ for monostatic case is given by

$$k_L = \begin{bmatrix} S_{HH} \\ \sqrt{2}\, S_{HV} \\ S_{VV} \end{bmatrix} \qquad (1\text{-}2)$$

The covariance matrix is obtained as $[C] = k_L k_L^{\dagger}$ which is expressed as

$$[C] = \begin{pmatrix} S_{HH}S_{HH}^{*} & \sqrt{2}\, S_{HH}S_{HV}^{*} & S_{HH}S_{VV}^{*} \\ \sqrt{2}\, S_{HV}S_{HH}^{*} & 2\, S_{HV}S_{HV}^{*} & \sqrt{2}\, S_{HV}S_{VV}^{*} \\ S_{VV}S_{HH}^{*} & \sqrt{2}\, S_{VV}S_{HV}^{*} & S_{VV}S_{VV}^{*} \end{pmatrix} \qquad (1\text{-}3)$$

where † represents complex conjugate and transpose, and * represents the complex conjugate.

Similarly, the coherency matrix is obtained as

$$\langle [T] \rangle = \langle k_p k_p^{\dagger} \rangle \qquad (1\text{-}4)$$

where $\langle\ \rangle$ represents the average over the whole data, k_p represents the Pauli vector given by

$$k_p = \frac{1}{\sqrt{2}} \begin{bmatrix} S_{HH} + S_{VV} \\ S_{HH} - S_{VV} \\ 2S_{HV} \end{bmatrix} \qquad (1\text{-}5)$$

The coherency matrix obtained from above is given by

$$\langle [T] \rangle = \begin{bmatrix} \langle |S_{HH} + S_{VV}|^2 \rangle & \langle (S_{HH} + S_{VV})(S_{HH} - S_{VV})^* \rangle & 2\langle (S_{HH} + S_{VV})S_{HV}^* \rangle \\ \langle (S_{HH} - S_{VV})(S_{HH} + S_{VV})^* \rangle & \langle |S_{HH} - S_{VV}|^2 \rangle & 2\langle (S_{HH} - S_{VV})S_{HV}^* \rangle \\ 2\langle S_{HV}(S_{HH} + S_{VV})^* \rangle & 2\langle S_{HV}(S_{HH} - S_{VV})^* \rangle & 4\langle |S_{HV}|^2 \rangle \end{bmatrix} \qquad (1\text{-}6)$$

1.4. Polarimetric Decompositions

Various mathematical and physical models have been developed for extracting the target information from the backscatter. Most of these are forward models which are usually complex and employ large number of field based input parameters to model the backscatter and are difficult to invert to provide a unique solution[6]. Another category is the decomposition models, which are comparatively easier to understand and do not require a large number of input parameters. The polarimetric decomposition theorems were developed for extracting the physical information about the target surface. These techniques are aimed on separating the polarimetric measurements from a random media into independent elements which can be associated to the various physical scattering mechanisms occurring on the ground. These techniques are broadly classified into two categories- coherent and incoherent decompositions. In case of coherent decompositions, the scattering matrix is expressed as a weighted combination of scattering response of simple or canonical objects. These types of decompositions are applicable to only pure or coherent targets which give completely polarised backscatter. Many man-made structures are examples of such pure targets whereas the natural features are represented by the distributed targets, which give a complex scattering response due to presence of speckle noise. Therefore, these scatterers cannot be analysed by exploiting the scattering matrix. For such scatterers, incoherent decompositions are employed which are aimed at separating the measured covariance or the coherency matrix as a combination of second order descriptors representing simple scattering mechanisms.[5] Different model based incoherent decompositions have been developed in past. Freeman and Durden gave a significant contribution to incoherent decompositions by proposing a three component scattering model. This model was developed for describing the polarimetric response from the natural distributed areas by considering three basic scattering mechanisms – single bounce or surface bounce, double bounce and volume scattering. The single or surface bounce scattering is modelled as first order Bragg's scattering. For a pair of orthogonal surfaces having different dielectric constants, such as ground and tree trunk or ground and wall, the modelled scattering represents double bounce. Volume scattering is modelled as the response from randomly oriented dipoles in a vegetation canopy [6][7].

(a) Surface scattering   (b) Double-bounce

(c) Volume scattering
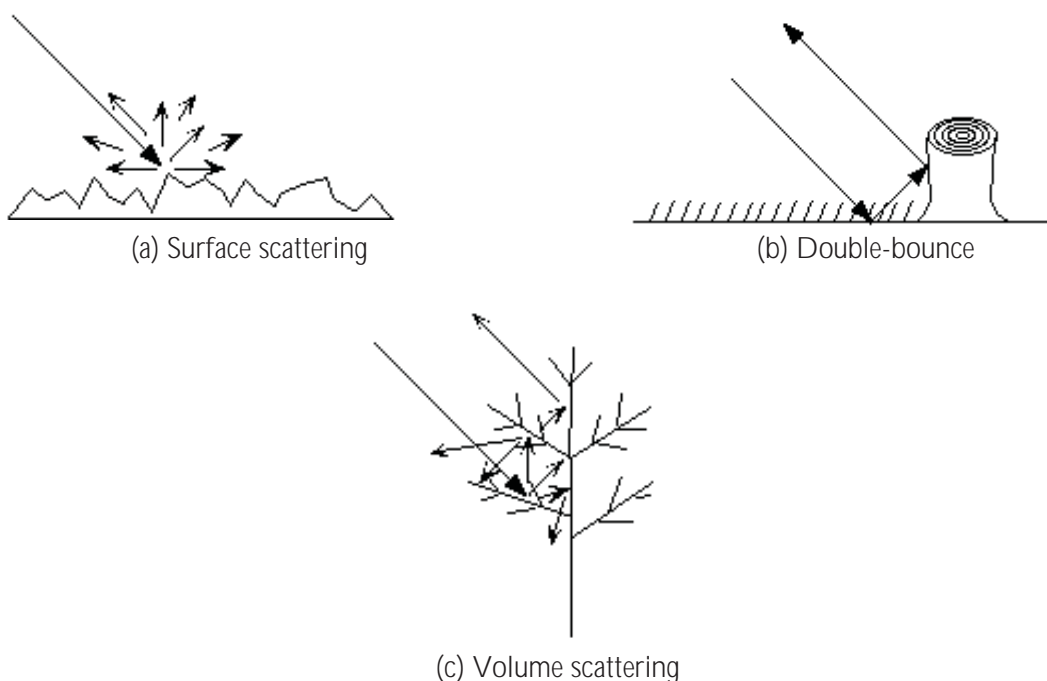
Figure 1-3 (a) Surface scattering from a rough surface (b) Double bounce scattering from a ground and tree trunk (c) Volume scattering from multiple reflections from the tree branches

1.5.   Motivation and Problem Statement

The polarimetric decomposition models were developed for natural distributed areas which are considered more homogeneous as compared to the urban areas. The natural areas are assumed to exhibit the property of reflection symmetry. In terms of SAR polarimetry, this implies that the correlation between the like polarised and cross polarised response is equal to zero. While in case of undulated terrain and presence of urban structures, this property doesn't hold [8][9][10]. Such areas are responsible for causing orientation angle shifts, which is described as the shift in the angle of rotation of incident plane along the radar line of sight. The radar cross section, which accounts for the effective scattering pixel area, is affected by these shifts and this can result in errors in the physical information extracted from such polarimetric images. Due to these shifts, the backscatter response from the oblique structures present in the urban areas is often decomposed into the volume scattering or the cross polarisation component (HV), which is characteristic in vegetation especially forest. This results in overestimation of the contribution from the volume scattering and also erroneous classification. Moreover, urban areas also exhibit two other types of scattering mechanisms, 'helix' and 'wire' scattering, from the complex shapes of the man-made structures and the edges of structures respectively, which are generally overlooked in the polarimetric decompositions[11]. Polarimetric decomposition involving urban areas requires consideration of this unique scattering behaviour to obtain accurate results.

This research is aimed at reducing the effect of the orientation angle shifts introduced by the man-made structures in urban areas, and complete decomposition of the backscatter. A cosine squared distribution was used for this purpose, which has already been used for characterizing the scattering from vegetation canopy[12]. This distribution takes into account the randomness of the orientation of the scatterers. The effectiveness of this distribution, for compensating the orientation angle shifts, was compared with the de-orientation done by rotation of coherency matrix. The coherency matrix is sensitive to the phase and orientation of the backscatter. Therefore, it was utilized in the study. The decomposition models that have been used in the past such as Freeman or Yamaguchi model, consider only 2, 3 or 4 types of scattering mechanisms which are not enough to represent scattering behaviour from urban areas. Therefore, for a complete decomposition of the polarimetric data involving urban areas, multiple component scattering model was used in order to extract the five scattering components – single bounce, double-bounce, volume, 'helix' and 'wire'.

This approach can be utilized for a general polarimetric decomposition which can enhance the applications of polarimetric SAR for urban areas. It will also provide an alternative to the optical remote sensing for various urban applications such as urban growth monitoring; human settlement pattern analysis, land use/ land cover change detection and in case of natural hazards mitigation. The urban planners and decision makers can utilize this approach for an efficient infrastructure management, tracking growth patterns and checking environmental degradation for sustainable development of the urban areas[13].

1.6.   Research Identification

1.6.1.   Research Objective

The objective of this research is to develop an approach for polarimetric decomposition based on general characterization of scattering from urban areas using cosine squared distribution, to compensate the effect of orientation angle shift, and complete decomposition of the backscatter using Multiple-Component Scattering Model.

1.6.2.   Research Questions

For the fulfilment of the objective, present study aims at answering the following questions:
1. How the cosine squared distribution describes the prominent scattering components present in urban areas i.e., double-bounce, helix and wire?
2. What is the relation between the different polarimetric response (co-pol and cross-pol) and the five scattering mechanisms?
3. Does the cosine squared distribution improve the information content and accuracy of the results of the Multiple Component Scattering Model decomposition?
4. How to validate the obtained results from the Multiple Component Scattering Model decomposition?

.

2.   LITERATURE REVIEW

2.1.   Radar Remote Sensing and SAR

Remote sensing with Radar systems employs radio waves or microwave region of the electromagnetic spectrum in the wavelength range of 1 mm to 1.3 m which is considerably longer than that of visible region. A significant property that differentiates the radar waves from the optical waves is the penetration capability. This specific property allows the radar wave to penetrate through haze, smoke, cloud cover, and extreme weather conditions, which makes it an excellent choice for the remote sensing of the tropical regions or scenarios such as flood or forest fires. The penetration capability of the radar wave increases with its wavelength. The following table lists the bands utilized for radar remote sensing in increasing order of their wavelengths as well as penetration capability.

Band	Wavelength (in *cm*)
Ka	0.75 - 1.10
K	1.10 -1.67
Ku	1.67 - 2.40
X	2.40 - 3.75
C	3.75 - 7.5
S	7.5 - 15.0
L	15.0 - 30.0
P	30.0 - 130

Table 2-1 Wavelengths of various Radar bands used for remote sensing

Radar is employed using radio waves to identify the presence of target features on the earth surface and to calculate their distance and angular position. A radar system transmits radar signals of known amplitude, phase, polarization, and wavelength and time reference. On interaction with the target surface, these properties are altered and therefore the signal scattered back towards the radar system is received with the altered properties. The radar systems are based on understanding these changes to estimate the properties of the target surface [7][1][14].

The amount of the power extracted by the target surface from the incident radar wave is described by the Radar cross section (RCS). It has the dimensions of area, but it is not related to any physical cross-section area of the target. All targets are assumed to scatter the incident radar wave isotropically. RCS is defined for discreet or isolated scatterers only.

SAR polarimetry deals with the science of acquiring, processing and analyzing the polarization state of an electromagnetic wave. These waves, because of their vector characterisation property providing the complete description of propagation and scattering phenomena, requires the wave polarization concept. In complex radar systems, the design of the antennas was made in such a way that they transmit and receive EM waves in more than single polarization [3]. Radar systems are designed to receive different polarization components at the same point of time, since the earth feature under investigation after reflecting the radio waves can change the polarization state of the transmitted wave. Some issues associated with SAR systems are complex interactions, speckle effects, topographic effects and the effect of surface roughness.

With the unique characteristics, SAR polarimetry has illustrated potential for some interesting applications dealing with the geophysical and biophysical parameters of the earth features. Estimation of surface

roughness, surface slopes, soil moisture, biomass, height of the vegetation, tree species as well as monitoring of snow cover and estimation of ice thickness, are some of the applications where SAR polarimetry has given quality results[4].

2.2. Coherency Matrix

The coherency matrix was introduced to describe the partial polarised waves of stationary electromagnetic waves. The coherency matrix is a complex Hermitian matrix containing real elements along the diagonal and complex conjugate entries in symmetric off-diagonal positions. As the name denotes, it has a more direct relationship to coherence between the elements of the k vector. The coherency matrix describes the local variations in the scattering[7].

The coherency matrix is a second order polarimetric descriptor which is obtained from the vectorized form of the scattering matrix using Pauli's basis. The Pauli matrices are given by

$$\varphi_P : \sqrt{2} \left\{ \begin{bmatrix} 1 & 0 \\ 0 & 1 \end{bmatrix}, \begin{bmatrix} 1 & 0 \\ 0 & -1 \end{bmatrix}, \begin{bmatrix} 0 & 1 \\ 1 & 0 \end{bmatrix}, \begin{bmatrix} 0 & -j \\ j & 1 \end{bmatrix} \right\} \tag{2-2}$$

The vectorised form of the scattering matrix using the Pauli format is given below.

$$k_p = \frac{1}{\sqrt{2}} \begin{bmatrix} S_{HH} + S_{VV} \\ S_{HH} - S_{VV} \\ 2S_{HV} \end{bmatrix} \tag{2-3}$$

The coherency matrix is obtained as

$$\langle [T] \rangle = \langle k_p k_p^\dagger \rangle \tag{2-4}$$

where † represents complex conjugate and transpose, ⟨ ⟩ represents the average over the whole data. The coherency matrix obtained from above is given by

$$\langle [T] \rangle = \begin{bmatrix} \langle |S_{HH} + S_{VV}|^2 \rangle & \langle (S_{HH} + S_{VV})(S_{HH} - S_{VV})^* \rangle & 2\langle (S_{HH} + S_{VV})S_{HV}^* \rangle \\ \langle (S_{HH} - S_{VV})(S_{HH} + S_{VV})^* \rangle & \langle |S_{HH} - S_{VV}|^2 \rangle & 2\langle (S_{HH} - S_{VV})S_{HV}^* \rangle \\ 2\langle S_{HV}(S_{HH} + S_{VV})^* \rangle & 2\langle S_{HV}(S_{HH} - S_{VV})^* \rangle & 4\langle |S_{HV}|^2 \rangle \end{bmatrix} \tag{2-5}$$

Lee et al.[15] described the interpretation of the off-diagonal terms of the coherency matrix. The $\langle (S_{HH} - S_{VV})S_{HV}^* \rangle$ i.e. the $[T_{23}]$ element of the coherency matrix is affected by the polarisation orientation angle shifts as well as the phase difference between the like polarised responses i.e. HH and VV. The real part of $\langle (S_{HH} - S_{VV})S_{HV}^* \rangle$ contains the information about the polarisation orientation angle shifts induced by terrain slopes in azimuth direction and the man-made structures, whereas the imaginary part of $\langle (S_{HH} - S_{VV})S_{HV}^* \rangle$ contains the information about the helicity as described by the polarimetric Sphere, Diplane and Helicity decomposition theory of Kroagager. Helicity is demonstrated in returns from the vegetation and very rough surfaces. The phase of $\langle (S_{HH} - S_{VV})S_{HV}^* \rangle$ was also found to be affected by the terrain azimuthal slopes. This also resulted in increase in the real part of $\langle (S_{HH} - S_{VV})S_{HV}^* \rangle$. The term $\langle (S_{HH} + S_{VV})(S_{HH} - S_{VV})^* \rangle$ represents the correlation between the surface scattering and the double bounce scattering. The eigen values of both the covariance matrix and the coherency matrix are always real and are identical. The sum of the diagonal elements of each matrix is also same and represents the total power of the backscattered wave.

2.3.   Orientation Angle Shifts

The orientation angle is the angle made by the major axis of polarization ellipse with the horizontal axis on the incident plane. It ranges between 0º to 180º. The oriented urban structures or the irregular terrain causes rotation of the backscatter wave around the radar line of sight which results in shifts in the polarisation orientation angle. These shifts can also occur due to radar look angle and by terrain slopes in the range and azimuth directions[16]. The orientation angle shift is defined as the angle which rotates the the incidence plane about the line of sight to the surface normal. This shift is given by the following expression

$$\tan \theta = \frac{\tan \omega}{-\tan \gamma \cos \varphi + \sin \varphi}$$ (2-6)

where $\tan \omega$ is the azimuth slope, $\tan \gamma$ is the slope in ground range direction and φ is the radar look angle. The radar geometry in relation to the orientation of the ground surface is described below in Figure 2-1.
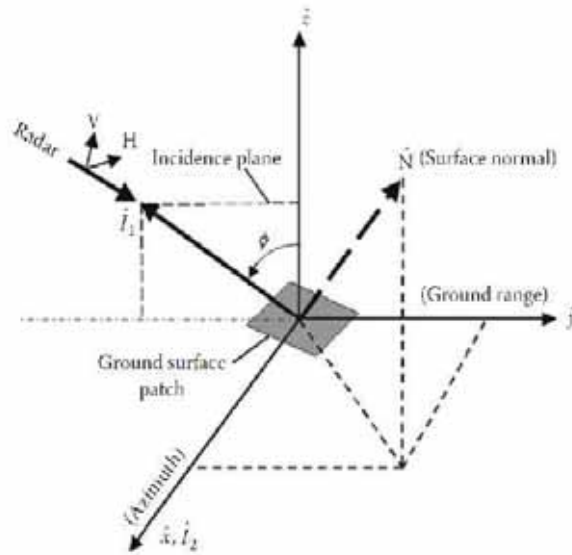
Figure 2-1 Radar geometry depicting the orientation of the ground surface

In the above figure, the unit vector pairs (x,y) represent the horizontal plane with x as the azimuth direction and y as the range direction. The (y,z) pair represent the radar incidence plane. The radar line of sight is in opposite direction of the incident signal along I_1 . The radar look angle is denoted by N represents the surface normal for the ground patch. For a calibrated polarimetric SAR system, the horizontal polarisation is parallel to the horizontal plane (x,y) and the vertical polarisation is parallel to the incidence plane (y, z). A horizontal ground surface patch has its surface normal in the incidence plane and thus does not produces any shifts in the orientation angles. But if the surface patch is tilted in the azimuth direction, then its surface normal is no longer in the incidence plane. This induces polarisation angle shift which is defined as the angle by which the incidence angle is rotated about the line of sight by to the surface normal [7]. The oriented urban scatterer also behaves like the ground patch and causes such shifts.

Kimura et al. [17][9] studied the polarisation angle shifts from the built-up areas. The scattering in built-up areas was attributed to three types of components – single bounce scattering from ground, roof or wall; double bounce scattering from ground-wall pair; triple bounce scattering from wall-ground-wall. These interactions are demonstrated in Figure 2-2. The contribution of the double bounce scattering was

demonstrated by the phase difference between the HH and HV polarisations. The surface bounce scattering and triple bounce scattering was found to be increased, due to which the orientation angles derived from X-band had lower absolute values than L-band.
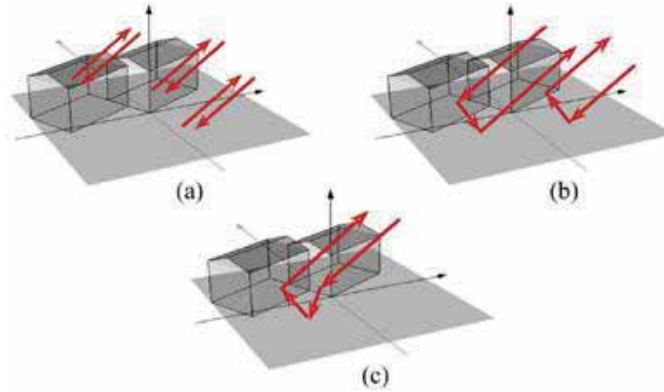
Figure 2-2 Scattering from urban structures

The shifts in the orientation angle affect the radar cross section of the effective scattering pixel area. When the target rotates with respect to incident radar wave, then it will have a different RCS defined by the implicit area needed at that specific orientation to account for the energy extracted from the incident wave and to reradiate it isotropically.

Iribe et al. [18] analysed the orientation angle shifts in the urban areas and found out that it is affected by the relation between the target rotation angle and the flight direction. Even in case of same target, the induced orientation angle shifts changed according to the radar look direction. The orientation angle shifts derived from the urban scatterers were considered to be reliable because of the coherent nature of such targets

Lee et al. [19] proposed two approaches to compensate the PolSAR data for azimuthal slope variations - first, by estimating orientation angles using DEM obtained from InSAR and second, by estimating the orientation angles directly from the PolSAR data. These techniques were based on the principle that the orientation induced by the topographic slopes can be compensated by rotating the data about the radar line of sight by the negative of the estimated orientation angle. Orientation angles obtained from the circular polarisation technique were found to be more accurate as compared to those obtained from C-band Interferometric DEM. The orientation angles obtained from the PolSAR data were found to be appropriate for compensating the effect of the azimuthal slopes.
Lee et al. [16] reviewed the various algorithms used for estimation of orientation angle and supported the use of circular polarization algorithm for the estimation of orientation angle shifts. It was observed that the electromagnetic waves with short wavelength are more sensitive to small scatterers present with a resolution cell, and also are less penetrative. Therefore, orientation angles can be easily estimated from L and P band, but not from C-band. Though orientation angles derived from L-band are found to contain noise and are less sensitive to terrain under vegetation canopy. Polarimetric calibration is also an essential requirement for estimating accurate polarisation orientation angle shifts, provided it should not be based on the assumption of reflection symmetry.

A concept of deorientation was introduced to reduce the effect of the randomness of the orientation of the scatterers[20]. The target orientation is turned to a specific fixed state with minimum cross-polarisation, using a transformation of the target scattering vector. From this fixed state, the deorientation

angle is extracted which gives the deviation of the target orientation from this state. A set of new parameters from lexicographical vectorization of the target scattering vector was defined to indicate the ratio and phase difference of the co-pol terms and the significance of the cross-pol term. These parameters and the entropy were applied to a classification of random terrain surface which resulted in distinguishing some special orientation details and spatial distribution of the targets.

Lee et al. [121] studied the effect of orientation angle compensation on the coherency matrix and scattering-model-based decompositions by Freeman–Durden[1] and Yamaguchi *et al.* [8]*.* It was concluded that the orientation angle compensation decreases the volume scattering power and increases the double bounce power, with slight modification in the surface power. The helix scattering component was found to be roll-invariant. This was explained by analysing the effect of orientation angle compensation on the 9 coherency matrix elements. It was observed that the $[T_{11}]$ element is roll invariant, $[T_{33}]$ decreased and $[T_{22}]$ increased and their sum was constant as the span was invariant under unitary transformation. In case of the element $[T_{23}]$, the real part becomes zero after deorientation and the imaginary part is rotational invariant. The magnitude of $[T_{13}]$ was found to decrease with decrease in $[T_{33}]$ and that of element $[T_{12}]$ was found to be increased with increasing$[T_{22}]$, though this behaviour was not consistent.

The compensation of the orientation angle shifts leads to decrease in the volume scattering contribution followed by increase in the double bounce scattering contribution. In the decomposed images, this results in decrease in the number of pixels exhibiting negative power values.

2.4.   Cosine Squared Distribution

Arii et al. [12] proposed a general characterization of polarimetric scattering from vegetation canopies using probability density function based on power of cosine squared functions which takes into account the random orientation of the vegetation canopy. The randomness in the orientation of the individual scatterers in case of vegetation can be described by two extreme cases – the uniform distribution and the delta function. The uniform distribution, which was used in the volume scattering model given by Freeman and Durden in is based on the assumption that vegetation or canopy contributing to the volume scattering can be represented by a cloud of uniformly randomly distributed thin cylinders. This distribution function is given by

$$p_{\text{uniform}}(\theta) = \frac{1}{2\pi}$$
(2-7)

The following figure shows the orientation of the uniformly randomly distributed scatterers along with the graph of the distribution.
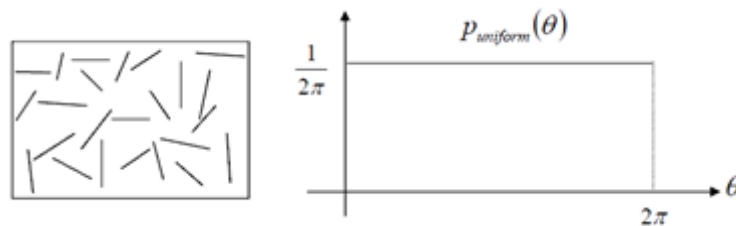
Figure 2-3 Orientation of scatterers in uniform distribution and its plot

This distribution may be appropriate for complicated vegetation as in a rainforest. The second extreme case is the delta function, which describes the orientation of the individual scatterers having exactly same orientation, with no variance. The delta function is given by

$$p_{\text{delta}}(\theta) = \frac{1}{2}\delta\big(\theta - (\theta_0 + m\pi)\big), \quad m = 0,1 \tag{2-8}$$

where θ_0 is the mean orientation angle. The plot of this function is given in figure
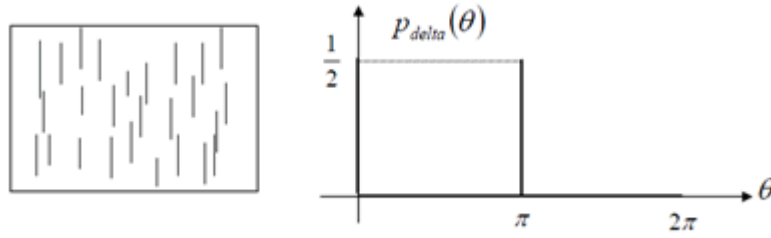
Figure 2-4 Orientation of scatterers in delta distribution and its plot

An intermediate case can be a cosine squared distribution, which has two peaks with π radian interval. It can be applied to any symmetrical shape as if it has a peak probability at a certain angle, then another peak probability exists at π radians from the first angle. This function assigns more probability to the vertical orientation than to the horizontal orientation. This probability density function is given by

$$p_{\text{cos\_sq}}(\theta) = \frac{1}{\pi}\cos^2\theta \tag{2-9}$$

The plot of this pdf is illustrated in Fig. 2-5
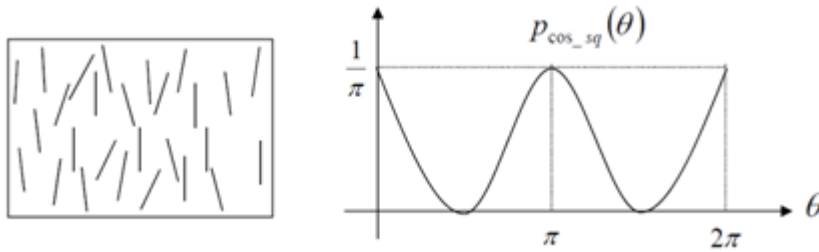
Figure 2-5 Orientation of scatterers in cosine squared distribution and its plot

Arii employed an nth power cosine squared distribution to model the deviation of the orientation of the scatterers from negligible randomness (represented by delta function) in the orientation to a highly uniform randomness [12]. This function is given by

$$p(\theta, \theta_0, n) = \frac{\left|\{\cos^2(\theta - \theta_0)\}^n\right|}{\int_0^{2\pi}|\{\cos^2(\theta - \theta_0)\}^n|\,d\theta} \tag{2-10}$$

where θ_0 is the mean orientation angle which varies from 0 to 2π. Here, if $n = 0$, then the above function describes a uniform distribution and if n is infinitely large then it describes the distribution of a surface which has a same orientation everywhere.
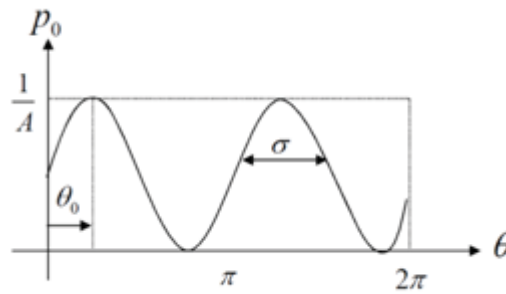
Figure 2-6 Nth power cosine squared distribution

As the distribution has two peaks, the standard deviation of the distribution was calculated from $\frac{-\pi}{2}$ to $\frac{\pi}{2}$ radian with zero mean, i.e. $\theta_0 = 0$ to measure the width of each peak. The standard deviation of the function uniquely and continuously incorporates all the cases from a delta function to a uniform distribution. Therefore, n was completely replaced by the standard deviation of the cosine squared distribution which will limit the range of parameter from (0 - ∞) to (0 – 0.91).[22] Elementary covariance matrices were derived for different types of the elementary scatterers. Arii adopted a non-negative Eigen value decomposition (NNED). Low randomness was observed from the longer wavelengths. Scattering from the C-band was predominantly generated from more vertically oriented needles, whereas in case of L and P band, appreciable amount of double bounce was present due to interaction of the longer wavelengths with large branches which were horizontally oriented. The mean orientation angle was found to be more sensitive to the shift of the scattering centre than the randomness. It was concluded that when the canopy scattering is not dominant, the inferred canopy randomness is low.

2.5. Polarimetric Decompositions

The polarimetric decomposition theory was first given by Huygen, but has its roots in work of Chandrashekhar on scattering of light by small anisotrophic particles.[23][6][24] In case of radar remote sensing, multivariate statistical description is required by the target of interest in radar images due to presence of a combination of coherent speckle noise and random vector scattering effects from different types of surfaces. Therefore, a concept of average or dominant scattering mechanism was generated for classification or inversion of the radar data. The objective of the polarimetric target decomposition theories is to express the average scattering mechanism as a sum of independent elementary scattering mechanisms to associate the physical scattering mechanisms with each component.

Two major categories of target decomposition theories that were developed are Coherent target decompositions and Incoherent Target Decompositions[5]. The coherent target decompositions are used to characterise the completely polarised scattering waves from the coherent targets for which the polarimetric information can be completely described by the scattering matrix. Significant coherent decompositions were contributed by Pauli, Krogager, Touzi and Cameron. Krogager proposed a coherent three component decomposition of the complex Sinclair matrix associated with canonical scattering mechanisms [25]. Sphere, dipole, diplane and helix were described as the canonical objects. The dipole or thin wire target and the diplane were described as a function of the orientation angle about the radar line of sight. Based on these targets the scattering matrix was decomposed into sphere, diplane and helix

components. This technique could resolve the different types of scatterers present within a single SAR resolution cell.

The second category is the incoherent decompositions which are based on the use of covariance or coherency matrix for characterising the complex scattering behaviour of natural distributed targets. Freeman and Durden in [4] [5], developed a new method to fit a model using the three basic scattering mechanisms namely the volume scattering modelled from a cloud of randomly oriented dipoles, the even or double-bounce scattering modelled from a pair of orthogonal surfaces with different dielectric constants and the single bounce scattering or Bragg scattering modelled from a moderate rough surface [4]. For modelling the volume scattering contribution, a uniform distribution was utilised as a probability density function to describe the orientation of the thin cylinder like dipoles. The newly developed model estimated the contribution to total backscatter from each of these scattering mechanisms without using any ground measurements. The number of input parameters (backscatter measurements) was equal to that of output parameters (three scattering components and two parameters describing them). The co-polarized and cross-polarized radar returns were assumed to be uncorrelated and therefore, the backscatter was reciprocal. This model was applied to C, L and P bands of AIRSAR data taken over various types of terrain. The model fitted well for tropical rainforests. An increase in the surface scattering was found for L and P bands for low incidence angles. Single bounce and double bounce scattering was found to be dominant as compared to volume scattering for urban areas. The study concluded that the three component scattering model decomposition can provide features that can distinguish between various surface cover types and can also estimate their present state(flooded or non-flooded).

Yamaguchi et al. added one more component – helix scattering, to the three component scattering model - helix scattering, to incorporate the correlations between the co-pol and the cross-pol response, which appears in complex scattering from urban areas and disappears for natural distributed scatterers. The concept of the helix scattering was developed by Krogager for his sphere, diplane and helix coherent decomposition. In addition to this, asymmetric volume scattering covariance matrix was introduced by employing a sine function as the probability density function to account for the orientation of the randomly oriented dipoles. To avoid the negative powers while implementing the decomposition algorithm, a power ratio was used in the algorithm, which states that the co-pol and the cross-pol channel powers are in the ratio 2:1. This four component scattering model decomposition was formulated for non- reflection symmetry cases, but it automatically includes the reflection symmetric case also. This decomposition algorithm was applied to L-band Pi-SAR images of Niigata city in Japan. The building blocks and bridges, which were oriented parallel to the SAR flight path illustrated dominant double bounce scattering. Helix scattering appeared dominant in the building blocks for which the orientation was not parallel to the flight path, and therefore, these were associated with predominant cross-pol response. Strong helix component was observed to be generated from facets of man-made structures due to complex multiple scattering. The physical randomness of the scatterers is well accounted by the four component decomposition algorithm. This algorithm was also developed using coherency matrix approach for better quantitative interpretation of PolSAR images. The results obtained were similar to that of the covariance matrix approach. Another concept to this decomposition was added to address some issues existing in polarimetric images of the urban areas. The building blocks, whose main scattering centre is at an oblique direction with respect to the radar line of sight, are known to display dominant cross-pol component as compared to the co-pol component. This cross-pol response is generated by multiple scattering occurring in such areas. Such areas are often decomposed into volume scattering which is contributed by the cross-pol component. Yamaguchi employed a simple and effective method i.e., rotation of coherency matrix and minimization of the cross-polarised component to retrieve orientation

angle. On implementation of the four component scattering model decomposition on the rotated coherency matrix, a clear discrimination between oriented urban structures and vegetation was obtained. The oriented urban structures, which were earlier decomposed into volume scattering component, were correctly decomposed into double bounce scattering component on applying the deorientation.

Moriyama et al. [26] proposed a polarimetric scattering model fit for urban areas. In this model, the scattering response from urban areas was represented by three types of elementary scattering mechanisms – odd bounce, even bounce and cross scattering. The single bounce, triple bounce and Bragg's surface scattering from a moderately rough surface is modelled as odd bounce scattering model. The even bounce scattering model describes the scattering from dihedral corner reflectors such as orthogonal pair of wall and ground. The remaining scattering component from the urban areas is described by the cross scattering model, which consists of the cross-polarised generated from the oriented dihedral corner reflectors and the thin wire targets present in urban areas. Even the oriented street patterns generated cross-polarised response. The polarimetric correlation coefficients were found to be beneficial for discriminating urban features from the natural features. This technique was applied to X-band PiSAR data and was compared with Freeman three component scattering model. The accuracy of this model was found to be dependent on the orientation of the street pattern. The even bounce scattering was found to be dominant in urban areas.

Zhang et al. [27] proposed Multiple Component Scattering Model for polarimetric decomposition which extends the four component scattering model by including a fifth component - wire scattering which is observed from the edges, eaves and window frames present in the urban areas. The wire scattering is modelled by a thin wire scatterer described as the function of the orientation angle around radar line of sight. The helix and the wire components are related to the cross-polarised response. The double bounce, helix and wire scattering components were found to be predominant in urban structures, especially for the structures having their edges parallel to the flight path. This decomposition represents a general case which considers both reflection symmetry and asymmetry conditions.

2.6.   Literature Review Summary

It can be concluded from the above literature that the urban structures exhibit specific scattering mechanisms and affects the total backscatter. These effects need to be considered during the polarimetric decomposition involving urban areas. Also, the assumption of reflection symmetry, on which most of the polarization decompositions are based, is not true in case of urban areas. Though the decomposition methods have been used individually for natural and man-made areas, but a generalized method for decomposition has still not been used, which can give accurate results for both. Moreover, two characteristic scattering mechanisms, 'helix' and 'wire' scattering are not explored much. The multiple component scattering model is required to obtain these components.

3.   STUDY AREA

The study area chosen for this research is situated in Uttarakhand state in northern part of India. This region falls in the Himalayan biogeographical zone in the country. The north eastern part of the image contains high mountains with rugged terrain. The central part of the study area is covered by the Rajaji National Park, which is characterised by tropical broadleaf forests. The study area also covers the dense deciduous forests of the Barkot forest area. The major urban areas that fall in this study area are Dehradun, Rishikesh and Haridwar along with some small towns such as Raiwala, Bhaniyawala, Raipur, Jogiwala, Kishanpur, Jawalpur etc. In general, these urban areas contained randomly distributed human settlements along with vegetation and agricultural patches. The footprint of the data of the study area is given in Figure 3-1.

3.1.   Scientific Significance of the Study Area

This area was selected for the study due to its diverse land cover types and varying topography. This area includes urban areas along with agricultural and forest areas as well as water bodies. Prominent man-made structures such as large building blocks present in the city of Haridwar, represented strong urban scatterers exhibiting double bounce, helix and wire scattering. Such scatterers were also present in the cities of Dehradun and Rishikesh, though much smaller in size and along with lots of vegetation. Therefore these areas acted as suitable sites for analysing whether the volume scattering from vegetation is discriminated from such small urban scatterers. Volume scattering was contributed mainly from the forest areas present in the scene. The water bodies i.e. the river Ganges flowing near the Haridwar and Rishikesh served as sites illustrating Bragg's surface scattering from the smooth surface. The high mountains and rugged terrain in the eastern zone of the image were used to observe the variation of scattering powers with topography.

INDIA

UTTARAKHAND
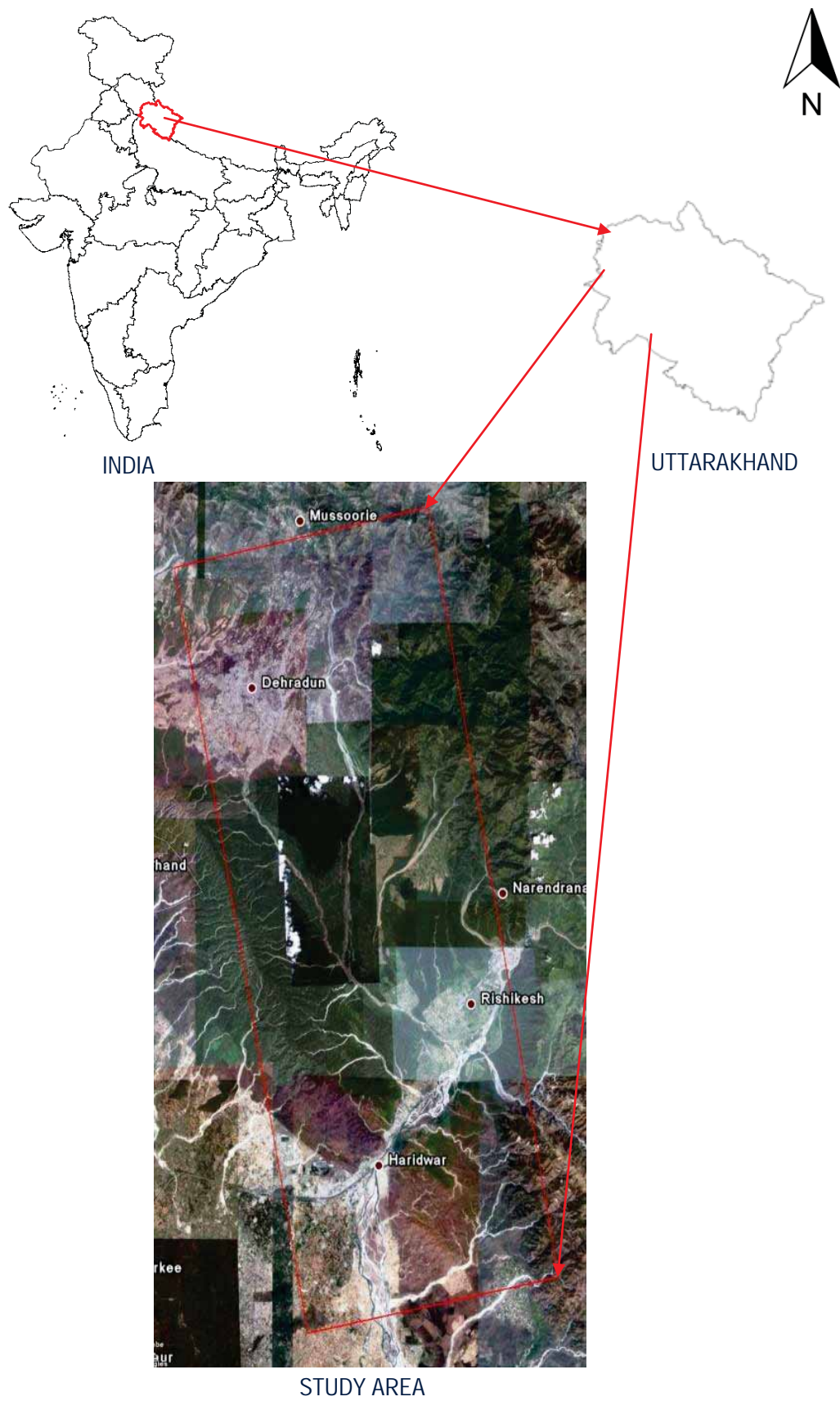
STUDY AREA

4.   MATERIALS AND METHODOLOGY

In this chapter, the dataset used and the software tools utilized for the study are described in the first section. The following section describes the detailed methodology employed to meet the objective of the presented research. The overview of the methodology adopted for this research has been shown in the Figure 4.1
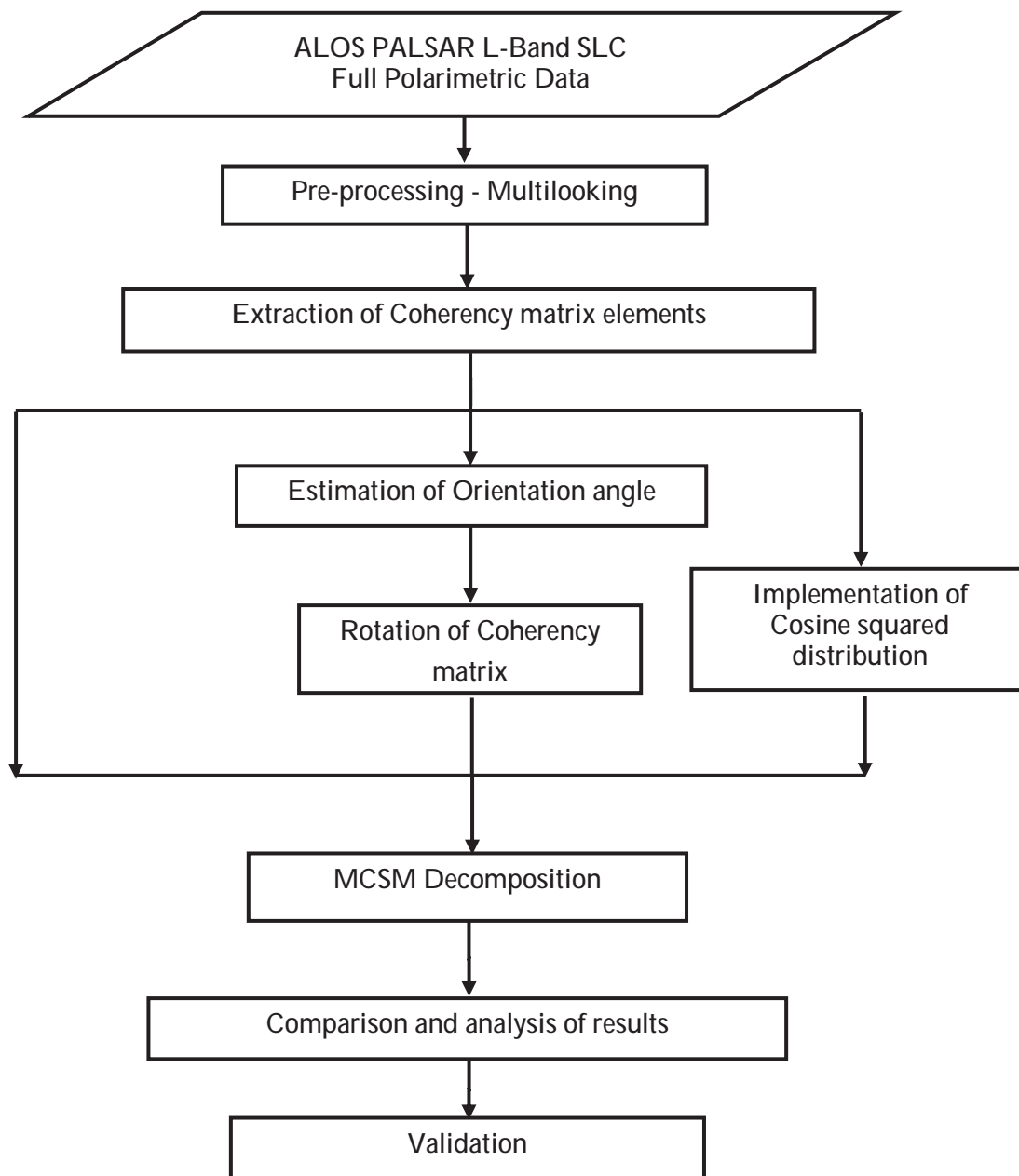
Figure 4-1 Methodology Flow Diagram

4.1. Data and Tools

4.1.1. Data

ALOS PALSAR L-Band fully polarimetric SLC data has been used in this study. The ALOS (Advanced Land Observation Satellite) is one of the largest Japanese satellite PALSAR (Phase Array L-Band Synthetic Aperture Radar), one of the three remote sensing instruments on board ALOS, was jointly developed by Japan Aerospace Exploration Agency (JAXA) and Japan Resources Observation System Organization (JAROS). PALSAR is a fully polarimetric instrument which operates in a fine-beam mode with single, dual and full polarisation. The description of the dataset is provided in Table 4-1.

Description of the Dataset	
Sensor	ALOS/PALSAR
Wavelength	23.5 cm
Date	5/25/2010
Polarisation	HH+HV+VV+VH
Mode	Ascending
Orbit Number	23086
Row Number	60.00
Swath Width	30 km
Incidence Angle	25.8°

Table 4-1 Description of the dataset

The L-band fully polarimetric data was in was in SLC (single look complex) format level 1.1 in which each pixel in the image contains a complex value, containing the amplitude and phase associated with the polarimetric scattering response of the scatterers represented by a single SAR resolution cell. The dataset contained four image files in SLC format (.SLC) for each polarisation channel, corresponding parameter file (.PAR) for each image, one meta file (.meta) and one product header file in text format (.txt) containing the data characteristics. The dataset also included one KML file, representing the footprint of the image, which was utilised to visualize the study area on Google Earth. The characteristics of the dataset are given below in Table 4-2.

Data Characteristics	
Pixel Spacing in Range Direction in SLC format	9.368 m
Pixel Spacing Azimuth Direction in SLC format	3.792 m
Ground Pixel resolution (Range)	3.792 m
Ground Pixel resolution (Azimuth)	18.737 m
Ground Resolution	20 m
Centre Latitude	30.1371880
Centre Longitude	78.1534530

Table 4-2 Characteristics of the ALOS PALSAR Dataset

The L-band, having wavelength 23.5 cm, has good penetration capability which was required for the utilised study area due to presence of forest and other vegetation. The orientation angle shifts can be better estimated from the L-band data. The fully polarimetric data was used in this research as it preserves

the complete vector nature of the electromagnetic wave and therefore it was beneficial for complete analysis of scattering behaviour of different features.

4.1.2.   Tools

The following softwares were used for this research.

PolSARpro version 4.2.0 - This is open source software which is capable of handling multi-polarization SAR data and it was employed for polarimetric processing and analysis.

ENVI version 4.8 with its module SARscape was utilised for visualization, processing and analysis.

Microsoft Excel 2007 was utilized for comparative analysis.

4.2.   Methodology

In this study, the methodology employed is based on the use of polarisation coherency matrix since it is highly sensitive to the orientation of the scatterers and it is closely associated to the physical scattering mechanisms occurring on the target surface. As the dataset was available in SLC format, therefore the first step was to convert the dataset into a standard format and extracting the coherency matrix elements. Pre-processing was carried out to convert the data from slant range to ground range using the multilooking process. From the multi looked data the coherency matrix elements were extracted. The second step was to estimate the orientation angle shifts occurring due to the oriented urban scatterers and the rugged terrain in the image. The third step involved the use of mean orientation angle obtained from the previous step, to rotate the coherency matrix elements on the basis of deorientation theory. As an alternate step, the basic coherency matrices were derived for each elementary scattering mechanism, using the cosine squared distribution as a probability density function to describe the orientation of the scatterers. In the fourth step, the decomposition algorithm using Multiple Component Scattering Model (MCSM) was developed for both direct decomposition and for cosine squared distribution. The detailed mathematical modelling of the decomposition algorithm has been described in the next chapter. Finally, the results from three decomposition methods i.e. direct MCSM decomposition, MCSM decomposition with deoriented coherency matrix elements and MCSM decomposition using the cosine squared distribution, were compared and analysed.

4.2.1.   Pre-processing-Multilook Setup

The available ALOS PALSAR L-Band fully polarimetric data was in SLC (single look complex) format level 1.1 which implies that the data was in the form of the scattering matrix for single polarization channel (HH, HV, VH and VV), in terms of the complex scattering coefficient. The data also had speckle and was not geocoded. This data was in the slant range format, due to which it was compressed. Therefore, the resolution in azimuth and the range direction were different, 3 m and 21 m respectively. Slant range to ground range conversion was performed to equalize these resolutions. The multi look setup was generated by using 6 looks in the azimuth direction and 1 look in the range direction, which lead to increase in the azimuth resolution from 3 m to approximately 22m. This resulted in the creation of an image with square pixels due to equalization of the azimuth and range resolution. This process was carried out to improve the radiometric accuracy of the measurements and to reduce the speckle, though it also reduced the spatial resolution.
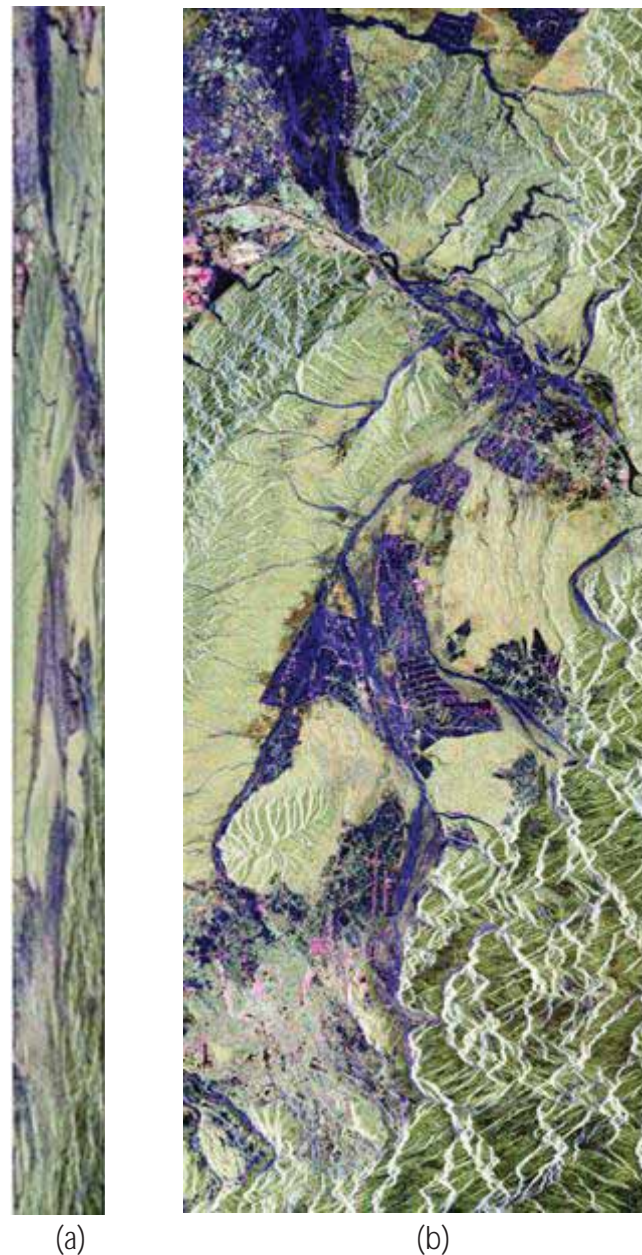
<center>(a)   (b)</center>

Figure 4-2 Pauli Colour Coded Image with HH-VV as Red, HV as Green, HH+VV as Blue (a) Single Look Complex (SLC) and (b) Multi looked Image

4.2.2. Polarisation Synthesis – Estimation of Coherency Matrix

The coherency matrix elements are extracted from the multi looked data, which contains the complex information about the different scatterers present in the image.

4.2.3. Direct MCSM Decomposition

The Multiple Component Scattering Model was proposed by L. Zhang et al. in 2008. The total backscatter from the distributed as well as isolated earth features is considered as the contribution of five types of physical scattering mechanisms - surface, double bounce, volume, helix and wire scattering. Each type of scattering mechanisms corresponds to a specific scattering behaviour of scatterers based on their geophysical parameters such as surface roughness, dielectric constant, geometrical structure, shape, orientation and reflectivity. These different types of scatterers can be represented by specific scattering matrices. From these basis scattering matrix, its second order statistics i.e. the covariance and the coherency matrices are formulated by using the Lexicographic and the Pauli basis vectors. The multiple component scattering model describes the total received backscatter as a linear combination of five types of elementary scattering mechanisms.[27]

The equation for MCSM using coherency matrix can be written as

$$[T] = f_s [T_s] + f_d [T_d] + f_v [T_v] + f_h [T_h] + f_w [T_w] \tag{4-1}$$

Here $[T]$ is the coherency matrix representing the total scattering and $[T_s], [T_d], [T_v], [T_h], [T_w]$ are the individual coherency matrices of the five components. Here f_s, f_d, f_v, f_h, f_w represent the expansion coefficients for each component.

In the first step, the basic coherency matrices, representing the five elementary scattering mechanisms, are substituted directly in this model to obtain the expressions for individual scattering powers corresponding to each elementary scattering mechanism.

I.   Surface Scattering

It consists of a first order Bragg surface scatterer modelling [2] from slightly rough surface in which the cross-polarized component is negligible. In case of the urban scatterers, similar scattering matrix is used for representing the odd bounce scattering which involves single bounce and triple bounce scattering [25]. The single bounce scattering is observed from the building roofs and vertical walls. The trihedral structures formed by wall-ground-wall exhibit triple bounce scattering. The coherency matrix for surface scattering is given by

$$\langle [T_s] \rangle = \begin{bmatrix} 1 & \beta^* & 0 \\ \beta & |\beta|^2 & 0 \\ 0 & 0 & 0 \end{bmatrix}, \quad \text{where } \beta = \frac{R_H - R_V}{R_H + R_V} \text{ and } |\beta| < 1 \tag{4-2}$$

where R_H, R_V are the Fresnel reflection coefficients for horizontally and vertically polarized wave.

II.   Double Bounce Scattering

This type of scattering behaviour is displayed by a dihedral corner reflector such as ground-tree trunk backscatter [2]. The coherency matrices is given by

$$\langle [T_d] \rangle = \begin{bmatrix} |\alpha|^2 & \alpha & 0 \\ \alpha^* & 1 & 0 \\ 0 & 0 & 0 \end{bmatrix}, \text{ where } \alpha = \frac{e^{2j\gamma_H} R_{TH} R_{GH} + e^{2j\gamma_V} R_{TV} R_{GV}}{e^{2j\gamma_H} R_{TH} R_{GH} - e^{2j\gamma_V} R_{TV} R_{GV}} \quad \text{and } |\alpha| < 1 \tag{4-3}$$

where R_{GH}, R_{TH} and R_{GV}, R_{TV} represents the reflection coefficients of the ground and tree trunk surface for horizontal and vertical polarization. This model is generalized by incorporating propagation factors $e^{2j\gamma_H}, e^{2j\gamma_V}$, where the complex coefficients γ_H and γ_V represent any propagation attenuation and phase change effects [7].

III.   Volume Scattering

Volume scattering mechanism corresponds to the multiple scattering processes occurring within a medium such as vegetation or forest canopy. This scattering is modelled by considering the vegetation canopy as a

cloud of randomly oriented thin cylinder like scatterers [2]. The covariance matrix for volume scattering is given by

$$[C_v] = \frac{1}{8}\begin{bmatrix} 3 & 0 & 1 \\ 0 & 2 & 0 \\ 1 & 0 & 3 \end{bmatrix} \tag{4-4}$$

The coherency matrix $[T]$ can be derived from the covariance matrix $[C]$ by using following relation

$$[T] = [A] \times [C] \times [A^T] \tag{4-5}$$

where $[A]$ is a similarity transformation matrix given by

$$[A] = \begin{bmatrix} \frac{1}{\sqrt{2}} & \frac{1}{\sqrt{2}} & 0 \\ 0 & 0 & 1 \\ \frac{1}{\sqrt{2}} & -\frac{1}{\sqrt{2}} & 0 \end{bmatrix} \tag{4-6}$$

The coherency matrix for volume scattering obtained from above method is given by

$$[T_v] = \begin{bmatrix} 2 & 0 & 0 \\ 0 & 1 & 0 \\ 0 & 0 & 1 \end{bmatrix} \tag{4-7}$$

IV.   Helix Scattering

This type of scattering behaviour is observed from the complex shapes of the man-made structures and sharp targets [8]. A complete circular polarised return is generated from a set of four dipoles oriented at an angle of 45º with a spacing of λ/8 wavelength in the range direction or a pair of dihedral corner reflectors oriented at 45º with a spacing of λ/4 wavelength in the range direction[25]. A left handed and a right handed circular polarization are generated by a helix target. The corresponding coherency matrix is given by

$$\langle[T_h]\rangle = \frac{1}{2}\begin{bmatrix} 0 & 0 & 0 \\ 0 & 1 & \pm j \\ 0 & \mp j & 1 \end{bmatrix} \tag{4-8}$$

V.   Wire Scattering

The edges of the buildings and other structures in urban areas contribute to the wire scattering component [27]. Wire scattering is modelled from the response of thin wire or dipole target describes by the function of the orientation angle about the radar line of sight[25]. For wire scattering mechanism,

$$[S_w] = \begin{bmatrix} \gamma & \rho \\ \rho & 1 \end{bmatrix}, \text{ where } \gamma = \frac{S_{HH}}{S_{VV}}, \rho = \frac{S_{HV}}{S_{VV}}$$

The coherency matrix is given by

$$\langle[T_w]\rangle = \frac{1}{2}\begin{bmatrix} |\gamma+1|^2 & (\gamma+1)(\gamma-1)^* & 2(\gamma+1)\rho^* \\ (\gamma-1)(\gamma+1)^* & |\gamma-1|^2 & 2(\gamma-1)\rho^* \\ 2(\gamma+1)^*\rho & 2\rho(\gamma-1)^* & 4|\rho|^2 \end{bmatrix} \tag{4-9}$$

VI.   MCSM Decomposition Algorithm

By substituting the values from each coherency matrix, following expression is obtained.

$$[T] = f_s \begin{bmatrix} 1 & \beta^* & 0 \\ \beta & |\beta|^2 & 0 \\ 0 & 0 & 0 \end{bmatrix} + f_d \begin{bmatrix} |\alpha|^2 & \alpha & 0 \\ \alpha^* & 1 & 0 \\ 0 & 0 & 0 \end{bmatrix} + \frac{f_v}{4} \begin{bmatrix} 2 & 0 & 0 \\ 0 & 1 & 0 \\ 0 & 0 & 1 \end{bmatrix} + \frac{f_h}{2} \begin{bmatrix} 0 & 0 & 0 \\ 0 & 1 & \pm j \\ 0 & \mp j & 1 \end{bmatrix}$$

$$+ \frac{f_w}{2} \begin{bmatrix} |\gamma + 1|^2 & (\gamma + 1)(\gamma - 1)^* & 2(\gamma + 1)\rho^* \\ (\gamma - 1)(\gamma + 1)^* & |\gamma - 1|^2 & 2(\gamma - 1)\rho^* \\ 2(\gamma + 1)^*\rho & 2\rho(\gamma - 1)^* & 4|\rho|^2 \end{bmatrix}$$

(4-10)

The total backscattered power or the Span is given by the sum of the diagonal elements of the coherency matrix.

$$P = T_{11} + T_{22} + T_{33}$$

The individual scattering powers for the five scattering mechanisms can be obtained from the above equation as

$$P_s = f_s(1 + |\beta|^2)$$
$$P_d = f_d(1 + |\alpha|^2)$$
$$P_v = f_v$$
$$P_h = f_h$$
$$P_w = f_w(1 + |\gamma|^2 + 2|\rho|^2)$$

(4-11)

The expansion coefficients for each scattering mechanism can be obtained by comparing the individual elements of the matrices

First, by comparing the T_{23} element

$f_h = 2 \, \text{Im}(T_{23})$ and $f_w = \frac{\text{Re}(T_{23})}{(\gamma - 1)\rho^*}$

This implies $P_h = f_h$ and $P_w = \frac{Re(T_{23})}{(\gamma-1)\rho^*}(1 + |\gamma|^2 + 2|\rho|^2)$

(4-12)

The volume scattering power is determined depending upon the magnitude balance of the co-polarized component HH verses VV, as given in [10][28]

$$10 \log \left[\frac{\langle |S_{VV}|^2 \rangle}{\langle |S_{HH}|^2 \rangle} \right] \Longrightarrow 10 \log \left[\frac{T_{11} + T_{22} - 2Re(T_{12})}{T_{11} + T_{22} + 2Re(T_{12})} \right]$$

(4-13)

For $10 \log(\langle |S_{VV}|^2 \rangle / \langle |S_{HH}|^2 \rangle) < -2dB$

$$\langle [T_v] \rangle = \frac{1}{30} \begin{bmatrix} 15 & 5 & 0 \\ 5 & 7 & 0 \\ 0 & 0 & 8 \end{bmatrix}$$

For $-2dB < 10 \log(\langle |S_{VV}|^2 \rangle / \langle |S_{HH}|^2 \rangle) < 2dB$

$$\langle [T_v] \rangle = \frac{1}{4} \begin{bmatrix} 2 & 0 & 0 \\ 0 & 1 & 0 \\ 0 & 0 & 1 \end{bmatrix}$$

For $10 \log(\langle |S_{VV}|^2 \rangle / \langle |S_{HH}|^2 \rangle) > 2dB$

$$\langle [T_v] \rangle = \frac{1}{30} \begin{bmatrix} 15 & -5 & 0 \\ -5 & 7 & 0 \\ 0 & 0 & 8 \end{bmatrix}$$

(4-14)

Depending upon the coherency matrix used for the volume scattering model, P_v can be obtained from following expressions.

$$P_v = 4T_{33} - 2P_h - 8f_w|\rho|^2 \quad \text{or} \quad P_v = \frac{15}{4}T_{33} - \frac{15}{8}P_h - \frac{15}{2}f_w|\rho|^2$$

(4-15)

Once the helix, wire and volume scattering powers are known, the remaining equations containing the coefficients for surface and double bounce power can be written as

$$S = f_s + f_d|\alpha|^2 = T_{11} - \frac{P_v}{2} - \frac{f_w}{2}(|\gamma + 1|^2)$$

$$D = f_s|\beta|^2 + f_d = T_{22} - T_{33} - \frac{f_w}{2}(|\gamma - 1|^2 - 4|\rho|^2)$$

$$C = f_s\beta^* + f_d\alpha = T_{12} - \frac{f_w}{2}(\gamma + 1)(\gamma - 1)^* \tag{4-16}$$

The expression for D and C also changes according to the coherency matrix used for volume scattering. The surface scattering and the double bounce scattering power is estimated by using assumptions based on the sign of the $\mathrm{Re}\langle S_{HH} S_{VV}^*\rangle$ term. In terms of coherency matrix elements, the $\mathrm{Re}\langle S_{HH} S_{VV}^*\rangle$ term can be estimated from the expression

$$C_0 = T_{11} - T_{22} - T_{33} + P_h \tag{4-17}$$

If the surface scattering is dominant, then $\mathrm{Re}\langle S_{HH} S_{VV}^*\rangle > 0$ i.e. $C_0 > 0$. In this case the double bounce scattering is considered to be negligible. Therefore, α is assumed to be zero. The values of S and C changes to $S = f_s$ and $C = f_s\beta^*$. The surface scattering power and the double bounce power is given by

$$P_s = f_s(1 + |\beta|^2) = S + \frac{|C|^2}{S}$$

$$P_d = f_d(1 + |\alpha|^2) = D - \frac{|C|^2}{S} \tag{4-18}$$

Similarly, if $Re\langle S_{HH} S_{VV}^*\rangle < 0$, then $\beta = 0$ (zero surface scattering), as the double bounce scattering is dominant. Therefore, the surface scattering power P_s and the double bounce scattering power P_d are estimated as

$$P_s = f_s(1 + |\beta|^2) = S - \frac{|C|^2}{D} \tag{4-19}$$

$$P_d = f_d(1 + |\alpha|^2) = D + \frac{|C|^2}{D}$$

In this way, all the five decomposed scattering power images are obtained. The algorithm for the Multiple Component Scattering Decomposition for estimating individual scattering powers is given in the following flowchart.

$$P_h = 2|\text{Im}(T_{23})|; \quad P_w = \frac{\text{Re}(T_{13})}{(\gamma - 1)\rho^*}(1 + |\gamma|^2 + 2|\rho|^2)$$

$$10 \log\left[\frac{T_{11} + T_{22} - 2\text{Re}(T_{12})}{T_{11} + T_{22} + 2\text{Re}(T_{12})}\right]$$

-2 dB   2 dB

$P_v = \frac{15}{4}T_{33} - \frac{15}{8}P_h - \frac{15}{2}f_w|\rho|^2$	$P_v = 4T_{33} - 2P_h - 8f_w|\rho|^2$	$P_v = \frac{15}{4}T_{33} - \frac{15}{8}P_h - \frac{15}{2}f_w|\rho|^2$
$S = T_{11} - \frac{P_v}{4} - \frac{f_w}{2}(|\gamma + 1|^2)$	$S = T_{11} - \frac{P_v}{4} - \frac{f_w}{2}(|\gamma + 1|^2)$	$S = T_{11} - \frac{P_v}{2} - \frac{f_w}{2}(|\gamma + 1|^2)$
$D = T_{22} - \frac{7}{30}P_v - \frac{P_h}{2} - \frac{f_w}{2}|\gamma - 1|^2$	$D = T_{22} - T_{33} + \frac{f_w}{2}(|\gamma - 1|^2 - 4|\rho|^2)$	$D = T_{22} - \frac{7}{30}P_v - \frac{P_h}{2} - \frac{f_w}{2}|\gamma - 1|^2$
$C = T_{12} \pm \frac{P_v}{6} + \frac{f_w}{2}(\gamma + 1)(\gamma - 1)^*$	$C = T_{12} - \frac{f_w}{2}(\gamma + 1)(\gamma - 1)^*$	$C = T_{12} \pm \frac{P_v}{6} + \frac{f_w}{2}(\gamma + 1)(\gamma - 1)^*$

$$P_v + P_h + P_w > T_p \quad \xrightarrow{\text{Yes}} \quad P_s = P_d = 0$$

No

$$C_0 = T_{11} - T_{22} - T_{33} + P_h$$

Single-bounce scattering   Double-bounce scattering

$$P_s = S + \frac{|C|^2}{S}$$
$$P_d = D - \frac{|C|^2}{S}$$

Yes $C_0 > 0$ No

$$P_d = D + \frac{|C|^2}{D}$$
$$P_s = S - \frac{|C|^2}{D}$$

$P_s > 0, P_d > 0,$	$P_s > 0, P_d < 0,$	$P_s < 0, P_d > 0$

P_s, P_d, P_v, P_h, P_w	$P_v, P_h, P_w \quad P_d = 0$	$P_v, P_h, P_w \quad P_s = 0$	$P_s = P_d = 0$
$T_p = P_s + P_d + P_v + P_h + P_w$	$P_s = TP - P_v - P_h - P_w$	$P_d = TP - P_v - P_h - P_w$	$P_v = TP - P_w - P_h$

Figure 4-3 MCSM Algorithm

4.2.4. MCSM Decomposition after Rotation of Coherency Matrix

In the second step, the rotated coherency matrix elements are used in place of the directly estimated coherency matrix elements from the data, as an input for the above model to analyse the effect of deorientation on the individual scattering powers obtained from the decomposition.

I. Estimation of Orientation Angle Shifts

The orientation angle shift (θ) was estimated using the following algorithm[29][16][10]

$$\theta = \begin{cases} \eta, & if \ \eta \leq \pi/4 \\ \eta - \pi/2, & if \ \eta > \pi/4 \end{cases}$$

where,

$$\eta = \frac{1}{4}\left[\tan^{-1}\left(\frac{-4\,\mathrm{Re}\,(\langle(\tilde{S}_{HH}-\tilde{S}_{VV})\tilde{S}_{HV}^*\rangle)}{-\langle|\tilde{S}_{HH}|^2-|\tilde{S}_{VV}|^2\rangle+4\langle|\tilde{S}_{HV}|^2\rangle}\right)+\pi\right]$$ (4-20)

where 'π' is added to unwrap the phase to extract useful information corresponding to surface slope and building alignment in azimuth direction.

II. Deorientation

The deorientation theory is aimed at rotating the target to a specific fixed orientation with minimisation of the cross-polarisation [20]. The coherency matrix will be rotated by using the estimated mean orientation angle θ_0 along the radar line of sight

$$[T(\theta_0)] = [R_p(\theta_0)][T][R_p(\theta_0)]^\dagger$$ (4-21)

where $[R_p(\theta_0)]$ represents the unitary rotation matrix given by

$$[R_p(\theta_0)] = \begin{bmatrix} 1 & 0 & 0 \\ 0 & \cos 2\theta_0 & \sin 2\theta_0 \\ 0 & -\sin 2\theta_0 & \cos 2\theta_0 \end{bmatrix}$$ (4-22)

After the rotation, the elements of the coherency matrix becomes

$$[T(\theta_0)] = \begin{bmatrix} T_{11}(\theta_0) & T_{12}(\theta_0) & T_{13}(\theta_0) \\ T_{21}(\theta_0) & T_{22}(\theta_0) & T_{23}(\theta_0) \\ T_{31}(\theta_0) & T_{32}(\theta_0) & T_{33}(\theta_0) \end{bmatrix}$$

The deorientation was performed using the mean of the orientation angle shifts $\theta_0 = 0.277$ from the estimated orientation angle shift image.

III. MCSM Decomposition Algorithm

The MCSM Decomposition algorithm provided in Figure 4-3 is used in this case. The only difference is the rotated coherency matrix is used for decomposition.

4.2.5. MCSM Decomposition after Implementation of Cosine Squared Distribution

Finally, the basic coherency matrices obtained from mathematical modelling after implementation of the cosine squared distribution on each matrix element are used as input to the multiple component scattering model decomposition algorithm

I. Implementation of Cosine Squared Distribution

For compensating the effect of orientation angle shifts, each of the basic scattering matrices is rotated by orientation angle θ around the radar line of sight. Each rotated scattering matrix is then used to derive the coherency matrix. After this the cosine squared distribution is implemented on each element of the coherency matrix. Then the resultant matrices for each type of scattering mechanism are used in the multiple component scattering model decomposition

a) Surface Scattering

The scattering matrix for single bounce or surface scattering is given by

$$[S_s] = \begin{bmatrix} R_H & 0 \\ 0 & R_V \end{bmatrix}$$

On rotation by angle θ around the radar line of sight, the scattering matrix becomes

$$\begin{bmatrix} S_{HH} & S_{HV} \\ S_{VH} & S_{VV} \end{bmatrix} = \begin{bmatrix} \cos\theta & -\sin\theta \\ \sin\theta & \cos\theta \end{bmatrix} [S_s] \begin{bmatrix} \cos\theta & \sin\theta \\ -\sin\theta & \cos\theta \end{bmatrix}$$

$$\begin{bmatrix} S_{HH} & S_{HV} \\ S_{VH} & S_{VV} \end{bmatrix} = \begin{bmatrix} R_H\cos^2\theta + R_V\sin^2\theta & (R_H - R_V)\cos\theta\sin\theta \\ (R_H - R_V)\cos\theta\sin\theta & R_H\sin^2\theta + R_V\cos^2\theta \end{bmatrix}$$

From the above matrix, the coherency matrix is obtained as

$$\langle [T_s] \rangle = \langle k_p k_p^\dagger \rangle$$

where the Pauli vector is given by

$$k_p = \frac{1}{\sqrt{2}} \begin{bmatrix} R_H + R_V \\ (R_H - R_V)\cos 2\theta \\ (R_H - R_V)\sin 2\theta \end{bmatrix}$$

The coherency matrix obtained from above is given by

$$\langle [T_s] \rangle$$

$$= \frac{1}{2} \begin{bmatrix} |R_H + R_V|^2 & (R_H + R_V)(R_H - R_V)^*\cos 2\theta & (R_H + R_V)(R_H - R_V)^*\sin 2\theta \\ (R_H + R_V)^*(R_H - R_V)\cos 2\theta & |R_H - R_V|^2\cos^2 2\theta & |R_H - R_V|^2\frac{\sin 4\theta}{2} \\ (R_H + R_V)^*(R_H - R_V)\sin 2\theta & |R_H - R_V|^2\frac{\sin 4\theta}{2} & |R_H - R_V|^2\sin^2 2\theta \end{bmatrix}$$

Dividing the matrix by $|R_H + R_V|^2$, we get

$$\langle [T_s] \rangle = \frac{1}{2} \begin{bmatrix} 1 & \beta^*\cos 2\theta & \beta^*\sin 2\theta \\ \beta\cos 2\theta & |\beta|^2\cos^2 2\theta & |\beta|^2\frac{\sin 4\theta}{2} \\ \beta\sin 2\theta & |\beta|^2\frac{\sin 4\theta}{2} & |\beta|^2\sin^2 2\theta \end{bmatrix} , \qquad \text{where} \quad \beta = \frac{R_H - R_V}{R_H + R_V} \quad \text{and} \quad |\beta| < 1$$

(5.28)

The probability density function describing the scatterer's orientation is $p(\theta)$. The expected value of any function $f(\theta)$ is given by [2]

$$\langle f \rangle = \int_0^{2\pi} f(\theta)\, p(\theta)\, d\theta \tag{4-23}$$

On applying this probability density function $p(\theta) = \cos^2\theta$ on each element of $\langle [T_s] \rangle$, we get

$$\langle [T_s] \rangle = \frac{1}{4} \begin{bmatrix} 2 & \beta^* & 0 \\ \beta & |\beta|^2 & 0 \\ 0 & 0 & |\beta|^2 \end{bmatrix} \tag{4-24}$$

b) Double Bounce Scattering

For double bounce scattering mechanism, the scattering matrix is given by

$$[S_d] = \begin{bmatrix} e^{2j\gamma_H} R_{GH} R_{TH} & 0 \\ 0 & e^{2j\gamma_V} R_{GV} R_{TV} \end{bmatrix}$$

.

On rotation by angle θ around the radar line of sight, the scattering matrix becomes

$$\begin{bmatrix} S_{HH} & S_{HV} \\ S_{VH} & S_{VV} \end{bmatrix} = \begin{bmatrix} \cos\theta & -\sin\theta \\ \sin\theta & \cos\theta \end{bmatrix} [S_d] \begin{bmatrix} \cos\theta & \sin\theta \\ -\sin\theta & \cos\theta \end{bmatrix}$$

$$\begin{bmatrix} S_{HH} & S_{HV} \\ S_{VH} & S_{VV} \end{bmatrix}$$
$$= \begin{bmatrix} e^{2j\gamma_H}R_{GH}R_{TH}\cos^2\theta + e^{2j\gamma_V}R_{GV}R_{TV}\sin^2\theta & \left(e^{2j\gamma_H}R_{GH}R_{TH} - e^{2j\gamma_V}R_{GV}R_{TV}\right)\cos\theta\sin\theta \\ \left(e^{2j\gamma_H}R_{GH}R_{TH} - e^{2j\gamma_V}R_{GV}R_{TV}\right)\cos\theta\sin\theta & e^{2j\gamma_H}R_{GH}R_{TH}\sin^2\theta + e^{2j\gamma_V}R_{GV}R_{TV}\cos^2\theta \end{bmatrix}$$

The Pauli vector is given by

$$k_p = \frac{1}{\sqrt{2}}\begin{bmatrix} \left(e^{2j\gamma_H}R_{GH}R_{TH} + e^{2j\gamma_V}R_{GV}R_{TV}\right) \\ \left(e^{2j\gamma_H}R_{GH}R_{TH} - e^{2j\gamma_V}R_{GV}R_{TV}\right)\cos 2\theta \\ \left(e^{2j\gamma_H}R_{GH}R_{TH} - e^{2j\gamma_V}R_{GV}R_{TV}\right)\sin 2\theta \end{bmatrix}$$

The coherency matrix is obtained as

$$\langle [T_d]\rangle = \frac{1}{2}\begin{bmatrix} |\alpha|^2 & \alpha\cos 2\theta & \alpha\sin 2\theta \\ \alpha^*\cos 2\theta & \cos^2 2\theta & \frac{\sin 4\theta}{2} \\ \alpha^*\sin 2\theta & \frac{\sin 4\theta}{2} & \sin^2 2\theta \end{bmatrix}$$

On applying this probability density function $p(\theta) = \cos^2\theta$ on each element of $\langle [T_d]\rangle$, we get

$$\langle [T_d]\rangle = \frac{1}{4}\begin{bmatrix} 2|\alpha|^2 & \alpha & 0 \\ \alpha^* & 1 & 0 \\ 0 & 0 & 1 \end{bmatrix}, \text{ where } \alpha = \frac{e^{2j\gamma_H}R_{TH}R_{GH} + e^{2j\gamma_V}R_{TV}R_{GV}}{e^{2j\gamma_H}R_{TH}R_{GH} - e^{2j\gamma_V}R_{TV}R_{GV}} \text{ and } |\alpha| < 1 \qquad (4\text{-}25)$$

c) Volume Scattering

For volume scattering mechanism,

$$[S_v] = \begin{bmatrix} S_H & 0 \\ 0 & S_V \end{bmatrix}$$

where S_H and S_V are the complex scattering coefficients.

Assuming that the scatterers are randomly oriented about the radar look direction with an angle θ from the vertical, the scattering matrix from a particular scatterer can be found out by rotating into a coordinate system with vertical along the scatterer's standard orientation. The scattered field can be estimated by rotating back to the radar coordinate system.

$$\begin{bmatrix} S_{HH} & S_{HV} \\ S_{VH} & S_{VV} \end{bmatrix} = \begin{bmatrix} \cos\theta & -\sin\theta \\ \sin\theta & \cos\theta \end{bmatrix} S \begin{bmatrix} \cos\theta & \sin\theta \\ -\sin\theta & \cos\theta \end{bmatrix}$$

$$\begin{bmatrix} S_{HH} & S_{HV} \\ S_{VH} & S_{VV} \end{bmatrix} = \begin{bmatrix} S_H\cos^2\theta + S_V\sin^2\theta & (S_H - S_V)\cos\theta\sin\theta \\ (S_H - S_V)\cos\theta\sin\theta & S_H\sin^2\theta + S_V\cos^2\theta \end{bmatrix}$$

The Lexicographic vector is given by

$$k_l = \begin{bmatrix} S_H\cos^2\theta + S_V\sin^2\theta \\ \sqrt{2}(S_H - S_V)\cos\theta\sin\theta \\ S_H\sin^2\theta + S_V\cos^2\theta \end{bmatrix}$$

On applying this probability density function $p(\theta) = \cos^2\theta$ on each element of covariance matrix $\langle [C_v]\rangle$, we get

$$\langle [C_v]\rangle = \frac{1}{8}\begin{bmatrix} 5 & 0 & 1 \\ 0 & 2 & 0 \\ 1 & 0 & 1 \end{bmatrix} \qquad (4\text{-}26)$$

The coherency matrix $[T]$ can be derived from the covariance matrix $[C]$ by using following relation

$$[T] = [A] \times [C] \times [A^T] \qquad (4\text{-}27)$$

where $[A]$ is a similarity transformation matrix given by

$$[A] = \begin{bmatrix} \frac{1}{\sqrt{2}} & \frac{1}{\sqrt{2}} & 0 \\ 0 & 0 & 1 \\ \frac{1}{\sqrt{2}} & -\frac{1}{\sqrt{2}} & 0 \end{bmatrix} \qquad (4\text{-}28)$$

The coherency matrix obtained using above method is

$$\langle [T_v] \rangle = \frac{1}{8} \begin{bmatrix} 2 & 0 & 0 \\ \frac{1}{\sqrt{2}} & 1 & \sqrt{2} \\ \frac{3}{2} & \frac{1}{\sqrt{2}} & 5 \end{bmatrix} \qquad (4\text{-}29)$$

d) Helix Scattering

The corresponding scattering matrices are

$$[S_{lh}] = \frac{1}{2}\begin{bmatrix} 1 & j \\ j & -1 \end{bmatrix} \quad , \quad [S_{rh}] = \frac{1}{2}\begin{bmatrix} 1 & -j \\ -j & -1 \end{bmatrix}$$

where $[S_{lh}]$ and $[S_{rh}]$ represent the left handed and the right handed scattering matrix. This can also be written as

$$[S_h] = \begin{bmatrix} 1 & \pm j \\ \pm j & -1 \end{bmatrix}$$

The corresponding coherency matrix is given by

$$\langle [T_h] \rangle = \frac{1}{2}\begin{bmatrix} 0 & 0 & 0 \\ 0 & 1 & \pm j \\ 0 & \mp j & 1 \end{bmatrix} \qquad (4\text{-}30)$$

As the helix scattering component is roll-invariant, therefore the cosine squared distribution is not applied here.

e) Wire Scattering

For wire scattering mechanism,

$$[S_w] = \begin{bmatrix} \gamma & \rho \\ \rho & 1 \end{bmatrix}, \text{ where } \gamma = \frac{S_{HH}}{S_{VV}}, \ \rho = \frac{S_{HV}}{S_{VV}}$$

On rotation by angle θ around the radar line of sight, the scattering matrix becomes

$$\begin{bmatrix} S_{HH} & S_{HV} \\ S_{VH} & S_{VV} \end{bmatrix} = \begin{bmatrix} \cos\theta & -\sin\theta \\ \sin\theta & \cos\theta \end{bmatrix}[S_w]\begin{bmatrix} \cos\theta & \sin\theta \\ -\sin\theta & \cos\theta \end{bmatrix}$$

$$\begin{bmatrix} S_{HH} & S_{HV} \\ S_{VH} & S_{VV} \end{bmatrix} = \begin{bmatrix} \sin^2\theta + \gamma\cos^2\theta - \rho\sin2\theta & \rho\cos2\theta + \frac{\sin2\theta}{2}(\gamma-1) \\ \rho\cos2\theta + \frac{\sin2\theta}{2}(\gamma-1) & \cos^2\theta + \gamma\sin^2\theta + \rho\sin2\theta \end{bmatrix}$$

$$k_p = \frac{1}{\sqrt{2}}\begin{bmatrix} \gamma+1 \\ \cos2\theta\,(\gamma-1) - 2\rho\sin2\theta \\ \sin2\theta\,(\gamma-1) + 2\rho\cos2\theta \end{bmatrix}$$

$\langle [T_w] \rangle =$

$$\frac{1}{2}\begin{bmatrix} |\gamma+1|^2 & (\gamma+1)(\cos2\theta\,(\gamma-1)-2\rho\sin2\theta)^* & (\sin2\theta\,(\gamma-1)+2\rho\cos2\theta)^*(\gamma+1) \\ (\cos2\theta\,(\gamma-1)-2\rho\sin2\theta)(\gamma+1)^* & |\cos2\theta\,(\gamma-1)-2\rho\sin2\theta|^2 & 2(\rho^*\cos^2 2\theta\,(\gamma-1)-\rho\sin^2 2\theta\,(\gamma-1)^*)+\frac{\sin4\theta}{2}(|\gamma-1|^2-|\rho|^2) \\ (\sin2\theta\,(\gamma-1)+2\rho\cos2\theta)(\gamma+1)^* & 2(\rho\cos^2 2\theta\,(\gamma-1)^* - \rho^*\sin^2 2\theta\,(\gamma-1))+\frac{\sin4\theta}{2}(|\gamma-1|^2-4|\rho|^2) & |\sin2\theta\,(\gamma-1)+2\rho\cos2\theta|^2 \end{bmatrix}$$

On applying the probability density function $p(\theta) = \cos^2\theta$ on each element of $\langle [T_w] \rangle$, we get

$$\langle [T_w] \rangle = \frac{1}{4}\begin{bmatrix} 2|\gamma+1|^2 & (\gamma+1)(\gamma-1)^* & 2(\gamma+1)\rho^* \\ (\gamma-1)(\gamma+1)^* & 4|\rho|^2 - 8|\rho| + |\gamma-1|^2 & 2(\gamma-1)\rho^* - 2\rho(\gamma-1)^* \\ 2(\gamma+1)^*\rho & 2\rho(\gamma-1)^* - 2(\gamma-1)\rho^* & 4|\rho|^2 + 8|\rho| + |\gamma-1|^2 \end{bmatrix} \qquad (4\text{-}31)$$

II. MCSM Decomposition Algorithm

$$[T] = \frac{f_s}{4}\begin{bmatrix} 2 & \beta^* & 0 \\ \beta & |\beta|^2 & 0 \\ 0 & 0 & |\beta|^2 \end{bmatrix} + \frac{f_d}{4}\begin{bmatrix} 2|\alpha|^2 & \alpha & 0 \\ \alpha^* & 1 & 0 \\ 0 & 0 & 1 \end{bmatrix} + \frac{f_v}{8}\begin{bmatrix} 2 & 0 & 0 \\ \frac{1}{\sqrt{2}} & 1 & \sqrt{2} \\ \frac{3}{2} & \frac{1}{\sqrt{2}} & 5 \end{bmatrix} + \frac{f_h}{2}\begin{bmatrix} 0 & 0 & 0 \\ 0 & 1 & \pm j \\ 0 & \mp j & 1 \end{bmatrix}$$

$$+ \frac{f_w}{4}\begin{bmatrix} 2|\gamma+1|^2 & (\gamma+1)(\gamma-1)^* & 2(\gamma+1)\rho^* \\ (\gamma-1)(\gamma+1)^* & 4|\rho|^2 - 8|\rho| + |\gamma-1|^2 & 2(\gamma-1)\rho^* - 2\rho(\gamma-1)^* \\ 2(\gamma+1)^*\rho & 2\rho(\gamma-1)^* - 2(\gamma-1)\rho^* & 4|\rho|^2 + 8|\rho| + |\gamma-1|^2 \end{bmatrix}$$

$$(4\text{-}32)$$

Comparing the individual elements of the matrices, following equations are obtained

$$[T_{11}] = \frac{f_s}{2} + \frac{f_d}{2}|\alpha|^2 + \frac{f_v}{4} + \frac{f_w}{2}|\gamma+1|^2$$

$$[T_{22}] = \frac{f_s}{4}|\beta|^2 + \frac{f_d}{4} + \frac{f_v}{8} + \frac{f_h}{2} + \frac{f_w}{4}(4|\rho|^2 - 8|\rho| + |\gamma-1|^2)$$

$$[T_{33}] = \frac{f_s}{4}|\beta|^2 + \frac{f_d}{4} + 5\frac{f_v}{8} + \frac{f_h}{2} + \frac{f_w}{4}(4|\rho|^2 + 8|\rho| + |\gamma-1|^2)$$

$$[T_{12}] = \frac{f_s}{4}\beta^* + \frac{f_d}{4}\alpha + \frac{f_w}{4}(\gamma+1)(\gamma-1)^*$$

$$[T_{13}] = \frac{f_w}{2}(\gamma+1)\rho^*$$

$$[T_{23}] = \pm j\frac{f_h}{2} + \frac{f_w}{2}\big((\gamma-1)\rho^* - \rho(\gamma-1)^*\big) + \frac{\sqrt{2}}{8}f_v \qquad (4\text{-}33)$$

Total Backscattered Power in this case is given by

$$P = T_{11} + T_{22} + T_{33}$$

$$P = \frac{f_s}{2}(1 + |\beta|^2) + \frac{f_d}{2}(1 + |\alpha|^2) + f_v + f_h + f_w(1 + |\gamma|^2 + 2|\rho|^2) \qquad (4\text{-}34)$$

Therefore the individual scattering powers can be obtained as

$$P_s = \frac{f_s}{2}(1 + |\beta|^2)$$

$$P_d = \frac{f_d}{2}(1 + |\alpha|^2)$$

$$P_v = f_v$$

$$P_h = f_h$$

$$P_w = f_w(1 + |\gamma|^2 + 2|\rho|^2) \qquad (4\text{-}35)$$

On comparing the T_{23} element, we get

$$f_h = 2\,\text{Im}(T_{23}) \qquad (4\text{-}36)$$

On comparing the T_{13} element, we get

$$f_w = \frac{2\,(T_{13})}{(\gamma+1)\rho^*} \qquad (4\text{-}37)$$

Therefore, using eq. (4-35) and eq. (4-36)

$$P_h = 2\,Im(T_{23}) \qquad (4\text{-}38)$$

$$P_w = \frac{2\,(T_{13})}{(\gamma+1)\rho^*}(1 + |\gamma|^2 + 2|\rho|^2) \qquad (4\text{-}39)$$

Also,

$$P_v = 4\sqrt{2}\,\text{Re}(T_{23}) - 2\sqrt{2}f_w\big((\gamma-1)\rho^* - \rho(\gamma-1)^*\big) \qquad (4\text{-}40)$$

The remaining components are obtained as given in the following flowchart for MCSM algorithm.

$$P_h = 2|\text{Im}(T_{23})|; \quad P_w = \frac{2(T_{13})}{(\gamma+1)}(1 + |\gamma|^2 + 2|\rho|^2)$$

$$P_v = 4\sqrt{2}\,\text{Re}(T_{23}) - 2\sqrt{2}\,f_w((\gamma-1)\rho^* - \rho(\gamma-1)^*)$$

$$S = T_{11} - \frac{P_v}{4} - \frac{f_w}{2}(|\gamma+1|^2)$$
$$D = 2T_{22} - \frac{P_v}{4} - P_h - \frac{f_w}{2}(4|\rho|^2 - 8|\rho| + |\gamma-1|^2)$$
$$C = 2T_{12} - \frac{f_w}{2}(\gamma+1)(\gamma-1)^*$$

$$P_v + P_h + P_w > T_p$$

Yes

$$P_s = P_d = 0$$

No

$$C_0 = T_{11} - T_{22} - T_{33} + P_h$$

Single-bounce scattering

$$P_s = S + \frac{|C|^2}{S}$$
$$P_d = D - \frac{|C|^2}{S}$$

Yes

$$C_0 > 0$$

No

Double-bounce scattering

$$P_d = D + \frac{|C|^2}{D}$$
$$P_s = S - \frac{|C|^2}{D}$$

$$P_s > 0, P_d > 0, \qquad P_s > 0, P_d < 0, \qquad P_s < 0, P_d > 0$$

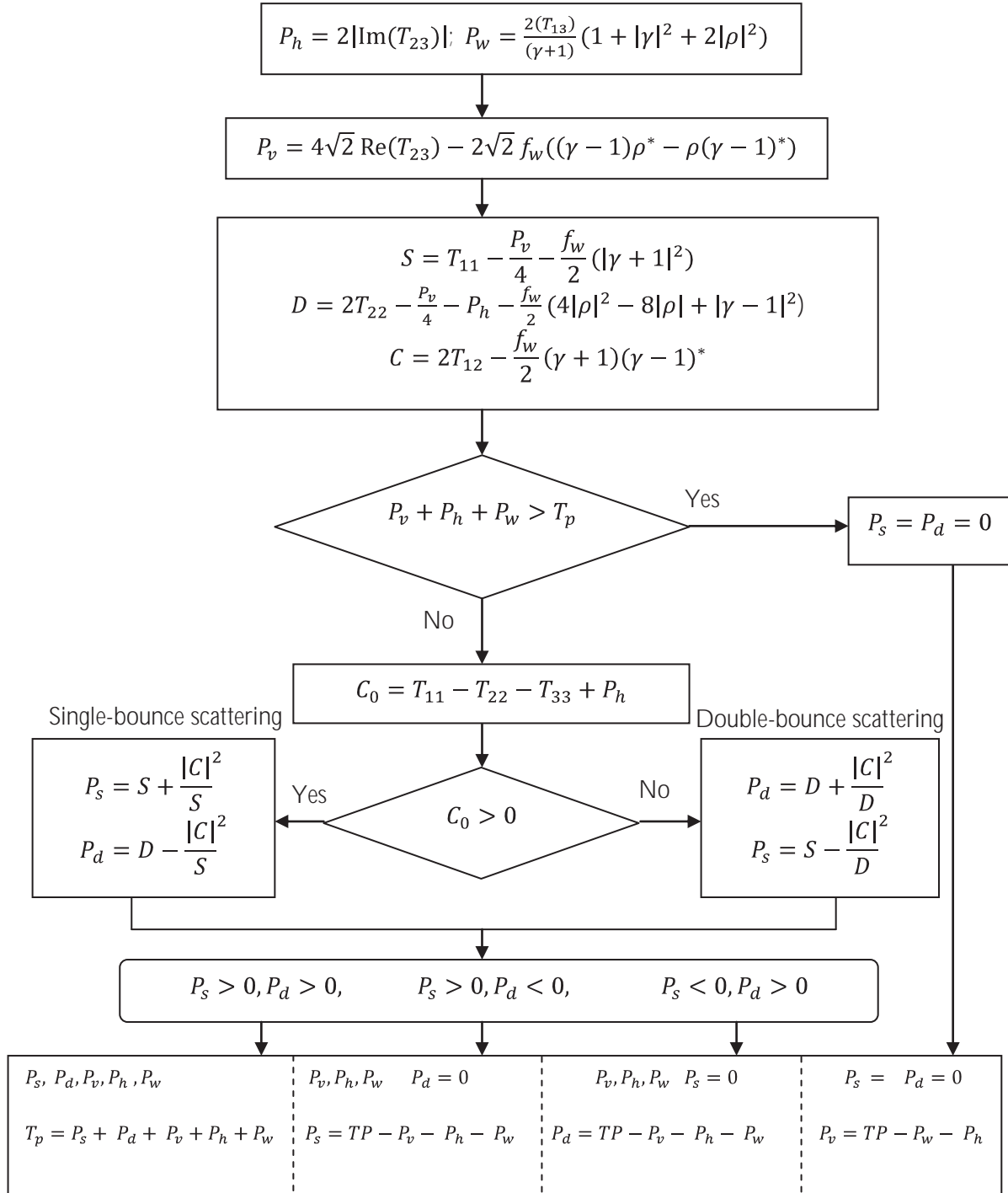| P_s, P_d, P_v, P_h , P_w	$P_v, P_h, P_w \quad P_d = 0$	$P_v, P_h, P_w \quad P_s = 0$	$P_s = \quad P_d = 0$
$T_p = P_s + P_d + P_v + P_h + P_w$	$P_s = TP - P_v - P_h - P_w$	$P_d = TP - P_v - P_h - P_w$	$P_v = TP - P_w - P_h$

Figure 4-4 MCSM Algorithm using Cosine squared distribution

4.2.6. Analysis

I. Sampling Plan

One of the objectives of the study was to analyse the scattering behaviour of different features with respect to each scattering mechanisms. Therefore, the sampling plan adopted for this study was stratified random sampling which considers each feature as a single strata or group. From each of these strata, samples can be extracted using simple random sampling to represent the characteristics of whole population. In this study, the urban features in Haridwar, Rishikesh and Dehradun are considered as individual strata representing the population of the urban areas. Along with these, the Barkot forest area was considered as individual strata from where random samples were extracted.

II. Techniques

a) Transect Analysis

A transect containing about 500 pixels was selected from an urban patch in the Haridwar region from the geocoded power images. The backscatter values of the pixels along this transect were plotted. The variations in the power values of the pixels were analysed. The backscatter response was compared to the earth features, represented by the corresponding pixels, using Google Earth.

b) Regression Analysis

The variation of the five scattering powers and the co-pol and the cross-pol responses is analysed using regression analysis using linear model. A random sample of 100 pixels were selected from the urban areas, from each of the three diagonal coherency elements and the corresponding scattering power images obtained from the MCSM decomposition using cosine squared distribution. Correlation coefficient is used to observe the fitness of the linear model to the relationship between the co-pol and cross-pol response and the corresponding scattering powers. The correlation coefficient gives the magnitude of the correlation between the two observed variables. The correlation coefficient is expressed as

$$\text{r} = \frac{n\Sigma(xy) - (\Sigma x)(\Sigma y)}{\sqrt{n(\Sigma x^2) - (\Sigma x)^2}\sqrt{n(\Sigma y^2) - (\Sigma y)^2}} \tag{4-50}$$

In equation x and y represents the two variables under study and n represents the total number of observations in the sample. The value of correlation coefficient r ranges from -1 to 1.

For measuring the fitness of the regression line modelled using the linear model, to the observed correlation between the variables, the coefficient of determination is used. This coefficient is given by

$$r^2 = 1 - \frac{c_p}{c_o} \tag{4-51}$$

In equation c_p represents the deviation from the original observed values for y variable from those predicted by the regression model, whereas c_o represents the original observed values for y variable. The coefficient of determination varies from 0 to 1.

Finally, the quality of the regression analysis is analysed using the residual analysis. Since, all the observations present in the regression model plot, does not always fall on the modelled regression line. Therefore such observations are analysed using the residual plots. The vertical difference in such observations and the modelled regression line is known as residual. Residual plot is a graphical representation of the residuals verses the corresponding y variable.

c) Comparison of Double bounce and Volume Scattering Powers

As an expected outcome of the present research, the double bounce scattering power should be increased and the volume scattering power should be decreased on implementation of the cosine squared distribution. Therefore, samples of 100 pixels were extracted from the double bounce power images and the volume scattering power images obtained from the three decomposition techniques. These samples were plotted for the three decomposition techniques. The observed plots were compared and analysed for understanding the changes introduced by the cosine squared distribution.

d) Patch Analysis

To analyse the improvement in the information content and accuracy of the MCSM decomposed results obtained after implementation of the cosine squared distribution, a small patch was selected from the urban area in the Haridwar city present in the image. This patch was selected due to dominance of the urban scatterers as compared to the natural features. The scattering contribution i.e. the pixel values from each of the five components was extracted from the three decomposition results. The total contribution of the five scattering powers i.e., P_s, P_d, P_v, P_h and P_w from the patch was plotted in the form of a pie chart for the three decomposition methods.

4.2.7. Validation

The validation of the obtained results was carried out by analysing the decomposed results on the basis of the concept of orientation compensation and the scattering behaviour of the urban scatterers. As stated earlier in , orientation compensation results in increase in the double bounce scattering contribution and decrease in the volume scattering contribution. This fact was analysed by comparing these two scattering powers from the MCSM decomposition results obtained from the direct, deoriented and the cosine squared distribution method. For physical validation of the obtained results, specific urban features were selected on the basis of their orientation angle and known scattering behaviour. Comparative analysis of these features was carried out to check whether the decomposition results represent the actual physical scattering behaviour of these urban features.

5.   RESULTS AND ANALYSIS

This chapter presents the results obtained from the methods described in the previous chapters. First, each of the obtained results from the major steps of the methodology has been described, along with the observations made from them. This is followed by the comparison and analysis carried out to obtain appropriate answers to the research questions.

5.1.   Orientation Angle Shifts

The orientation angle shift image and the corresponding histogram are given below in Figure 6-1.

(a)   (b)
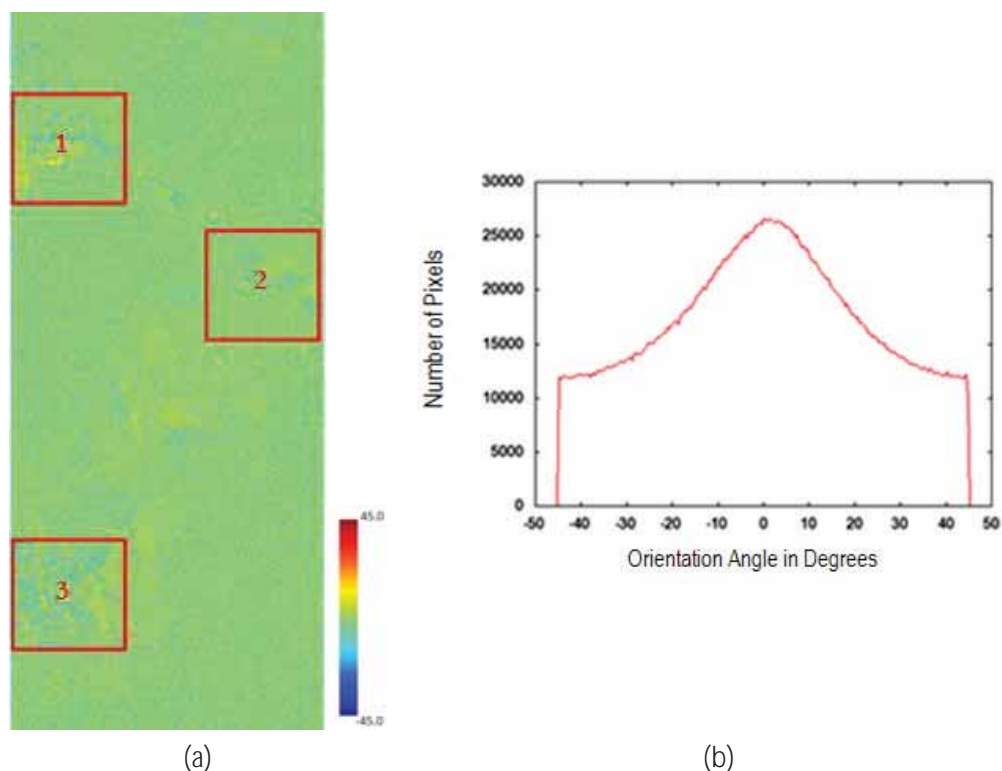
Figure 5-1: (a) Orientation angle shift image (b) corresponding histograms representing the orientation angle shifts in degrees.

From the histogram of the orientation angle shift image, it can be seen that the orientation angle shifts lie between -45º to +45º which is the expected range for this parameter. It was observed that the orientation angle shifts were more prominent in the urban areas of Haridwar (box1), Rishikesh (box2), and Dehradun (box3), which are highlighted in the above image. In the Haridwar city, high orientation angle shifts were observed from the edges of the large building blocks, while from the roofs of these building blocks, medium shifts were observed. An interesting observation was that the small urban settlements present near to the large building block were found to be generating alternate high and low orientation angle shift values. Similarly, high values were observed from small urban settlements present in the Dehradun city. The bridges present near Haridwar and Rishikesh city were also responsible for high values for shifts. These were approximately in range of 20º to 40º. The mean orientation angle was found to be equal to -0.277.

5.2.   Deorientation

The deorientation of the coherency matrix resulted in the decrease in the values of T_{33} element and slight increase in that of T_{22} element. But, some pixels from the urban areas demonstrated opposite behaviour i.e., the value of T_{33} element increased and that of T_{22} element decreased. This is illustrated in the Figure 6-2 which shows a small patch in the urban area in T_{33} element, where the response from the feature increased after deorientation.
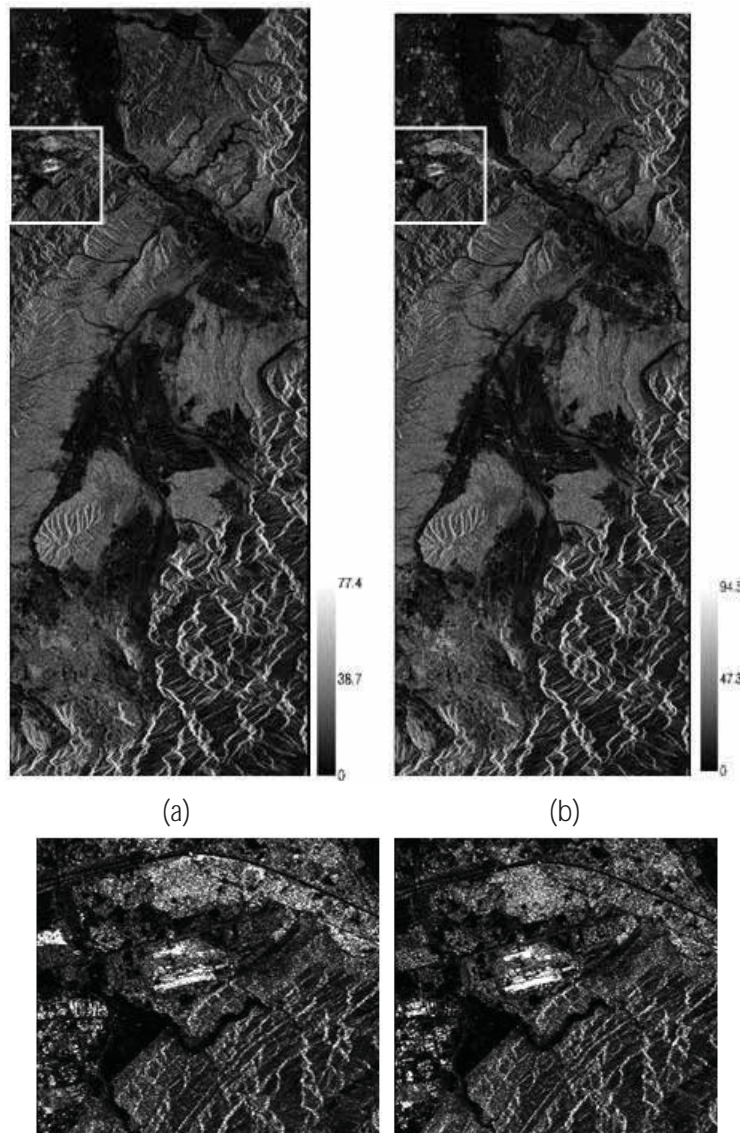

(a)   (b)

Figure 5-2: Coherency matrix element T33 (a) Before deorientation (b) After deorientation. A small urban patch displaying (c) bright response before deorientation(d)dark response after deorientation

On rotation the real part of T_{23} became zero and the imaginary part of T_{23} remained same. There was no consistent change in the values of T_{13} and T_{12}.

5.3.   Multiple Component Scattering Model Decomposition

5.3.1.   Direct Decomposition

In the surface scattering power, the flat terrain and agricultural patches produced brighter returns including the Dehradun airport runway. The high mountains in the lower portion of the image also produced high surface power. While in case of double bounce power, the urban structures and some part of the vegetation displayed brighter tones.
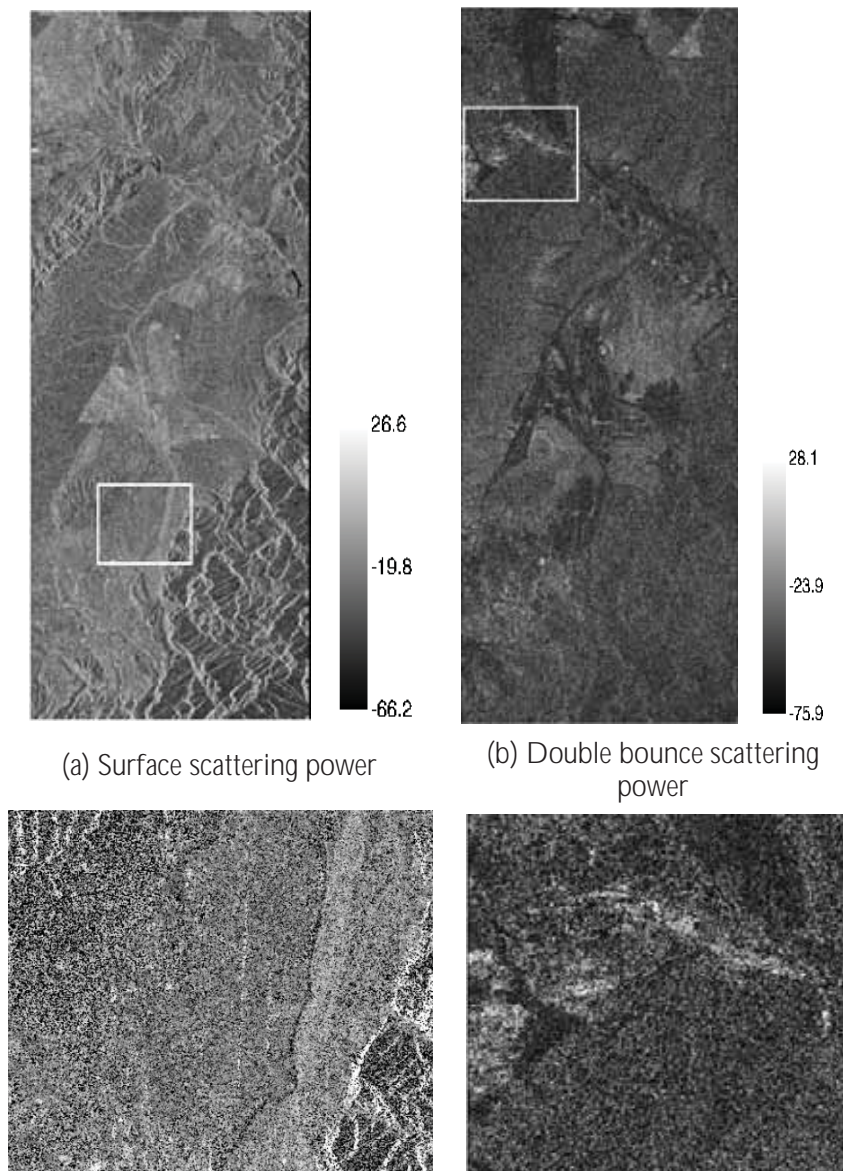
.

(a) Surface scattering power

(b) Double bounce scattering power

Figure 5-3 (a) Surface scattering power (b) Double bounce scattering power (c)Airport runway displaying bright response in surface scattering power image (d)Urban area (Haridwar city) displaying bright response in double bounce scattering power image.
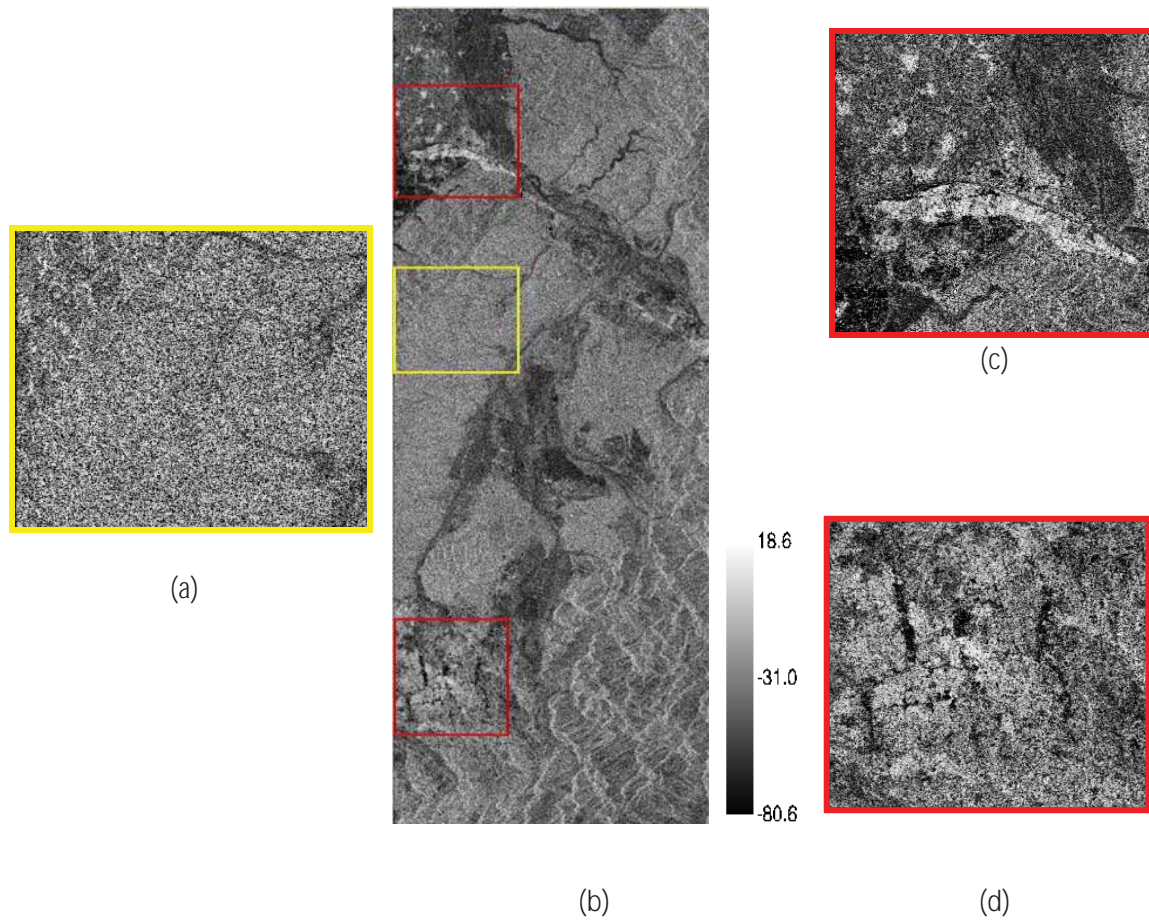
Figure 5-4 (a) Forest feature displaying bright response in volume scattering power image (b) Volume scattering power. Bright response is also observed from urban area in (c) Haridwar (d) Dehradun

In case of the volume scattering power, as expected, the returns from the forests were high as displayed in yellow box (a). In addition to this, bright response was also observed from the urban areas in Haridwar (c) and Dehradun (d) displayed in the red boxes. These were the same areas ehich displayed high values of orientation angle shifts. Another significant observation was the black pixels present in the image, which were more concentrated in the urban areas. These black pixels represented -NaN(Not a Number) values.
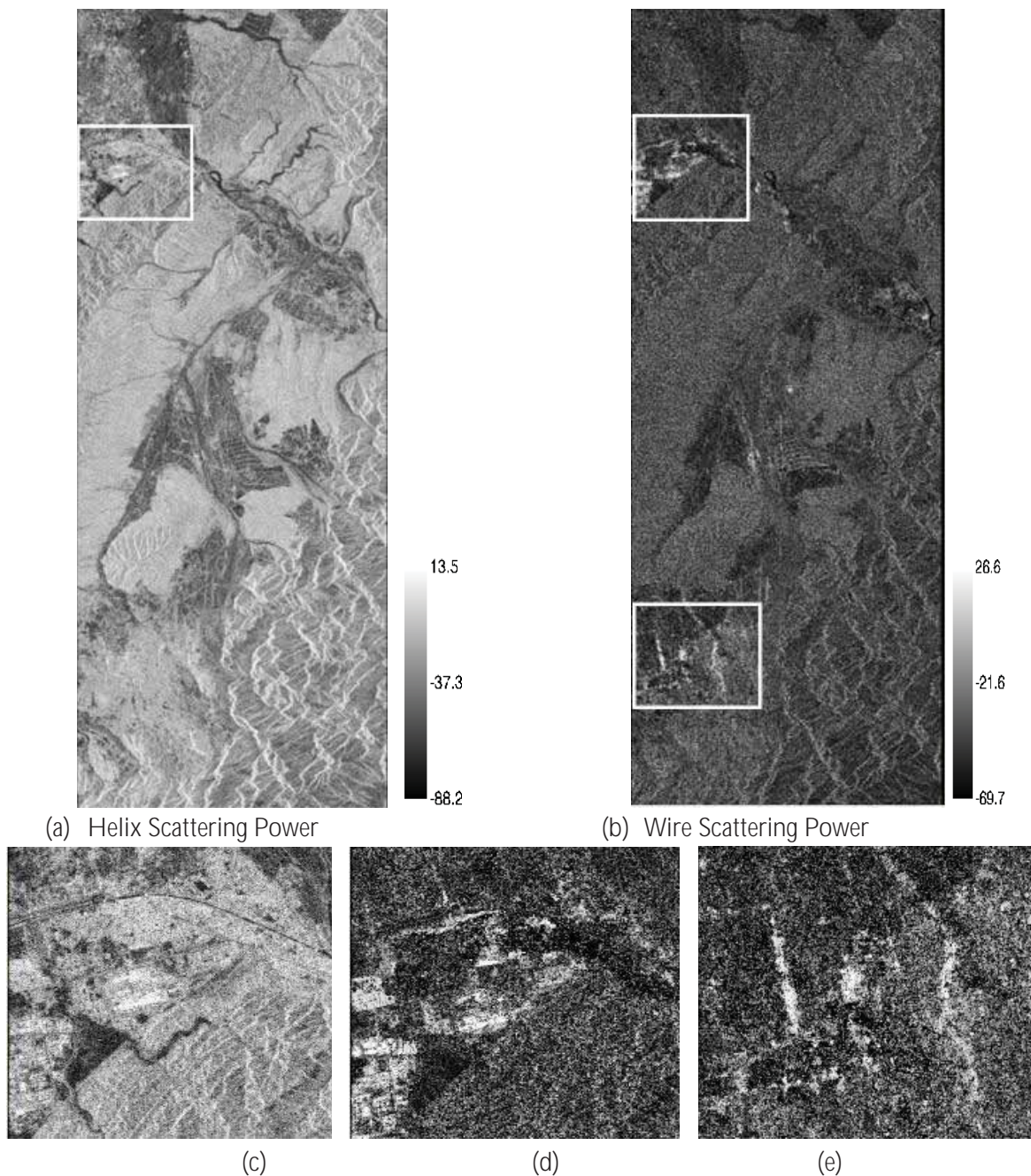
(a) Helix Scattering Power	(b) Wire Scattering Power

(c)	(d)	(e)

Figure 5-5 (a) Helix scattering power (b) Wire scattering power (c)Urban area (Haridwar) displaying bright response in helix scattering power image. Clearly visible urban areas (d) Haridwar and, (e) Dehradun in wire scattering power image

The helix power image illustrated bright response in case of urban areas. The overall response in the wire scattering power was quite low, except for the urban scatterers which were highlighted in the decomposed image

5.3.2.   MCSM Decomposition after Deorientation

The rotation of the coherency matrix makes the real part of the T_{23} term zero. This makes the wire scattering power zero. Therefore, wire scattering power was not obtained for deoriented results. The volume scattering power was found to be quite high even for the urban scatterers. The helix scattering power is roll-invariant, therefore its behaviour was same as described in previous section. However, the number of negative pixels was quite low.
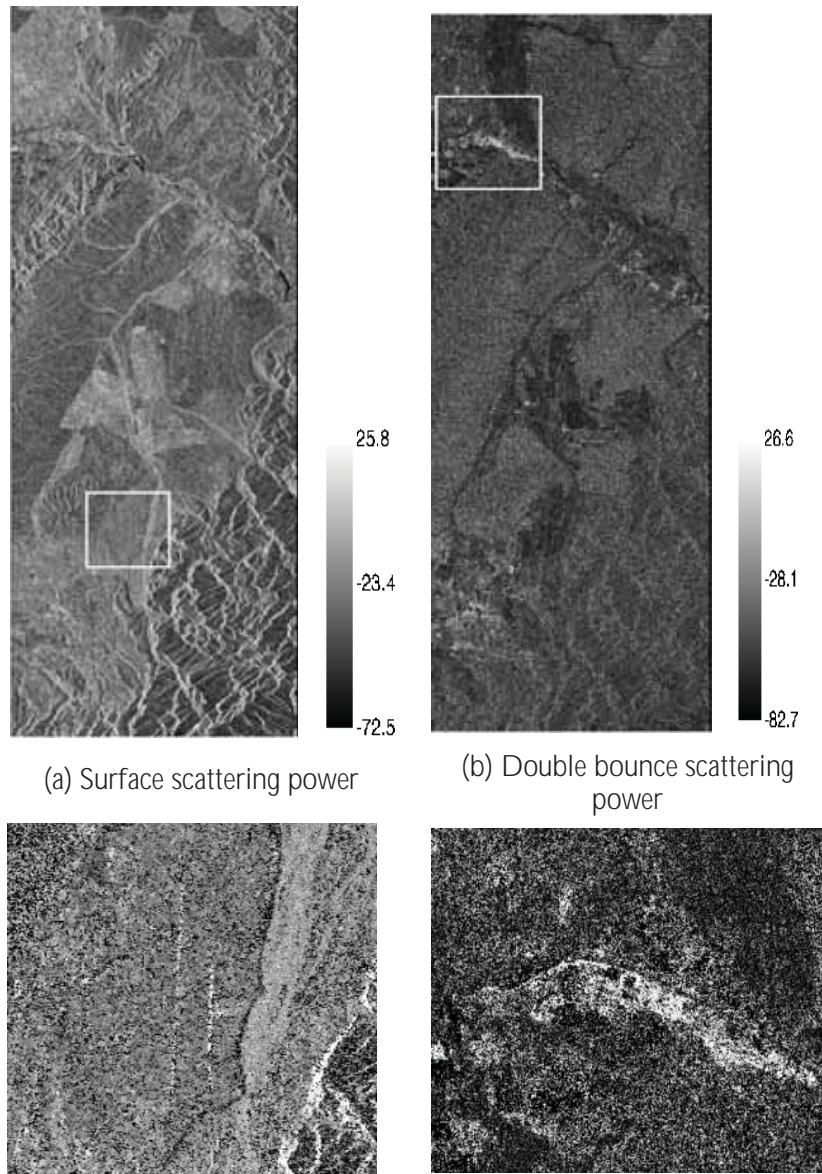

(a) Surface scattering power

(b) Double bounce scattering power

Figure 5-6 (a) Surface scattering power (b) Double bounce scattering power (c)Airport runway displaying bright response in surface scattering power image (d)Urban area (Haridwar city) displaying bright response in double bounce scattering power image.
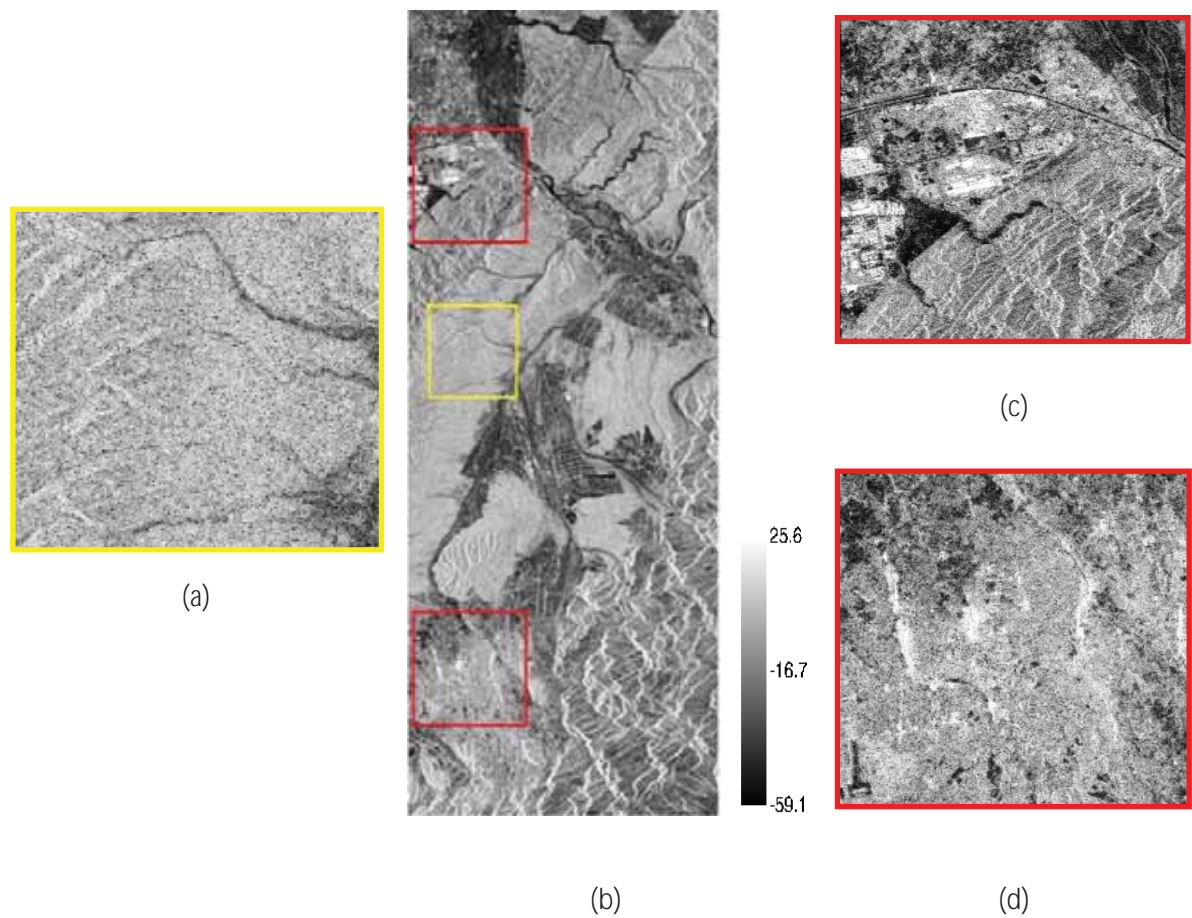
(a)

(b)

(c)

(d)

Figure 5-7 a) Forest feature displaying bright response in volume scattering power image (b) Volume scattering power. Bright response is also observed from urban area in (c) Haridwar (d) Dehradun

5.3.3.   MCSM Decomposition after Implementation of Cosine Squared Distribution

The surface scattering power was found to be increased. The volume scattering contribution was found to be very low, whereas the wire scattering contribution was quite high. The double bounce power was also found to be high.
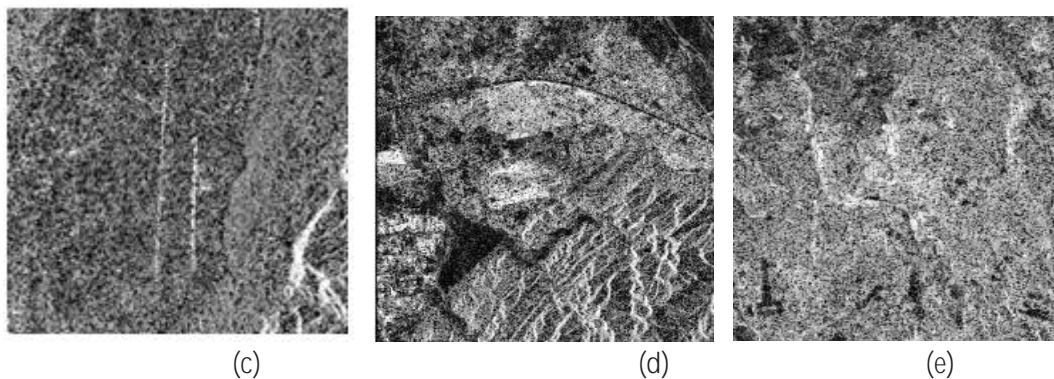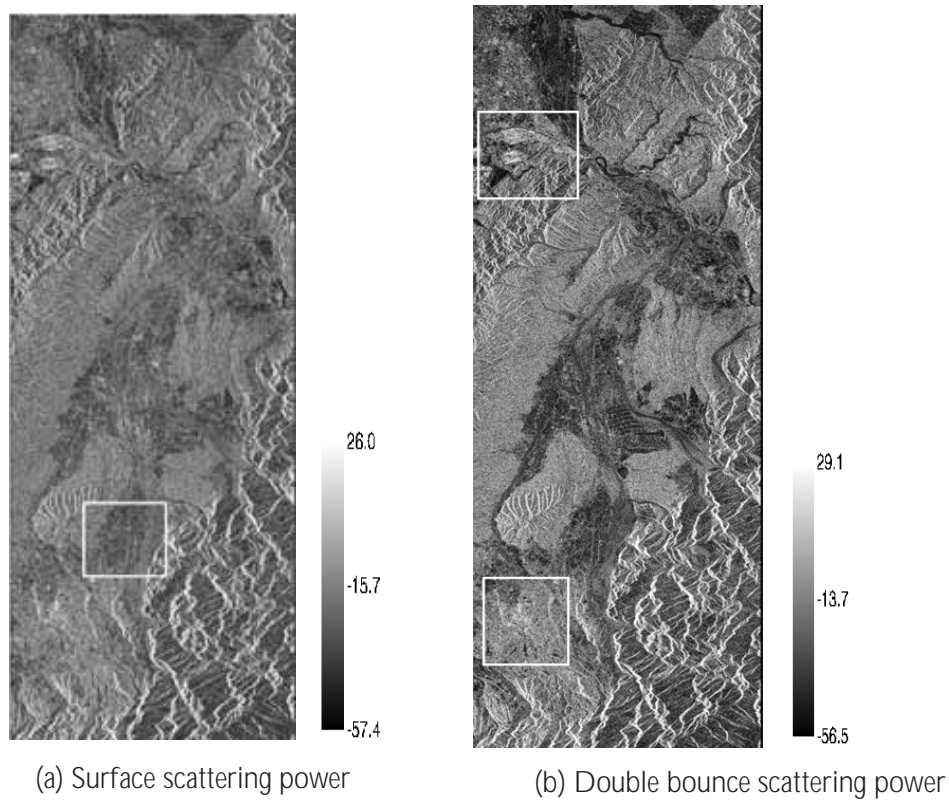

(a) Surface scattering power   (b) Double bounce scattering power

(c)   (d)   (e)

Figure 5-8 (a) Surface scattering power (b) Double bounce scattering power (c)Airport runway displaying bright response in surface scattering power image (d)Urban area (Haridwar city) and (e) Dehradun city displaying bright response in double bounce scattering power image.
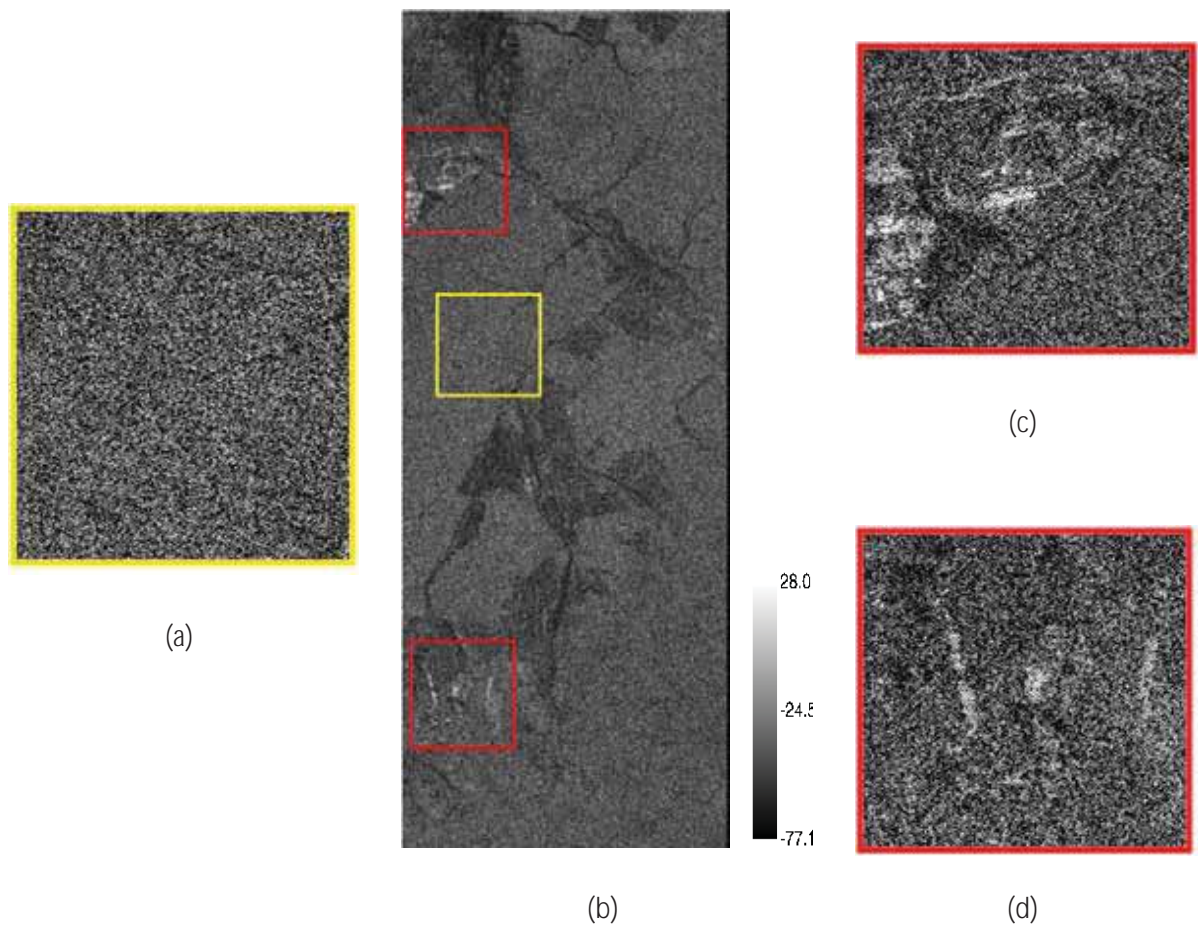
Figure 5-9 (a) Forest feature displaying bright response in volume scattering power image (b) Volume scattering power. Bright response is also observed from urban area in (c) Haridwar (d) Dehradun
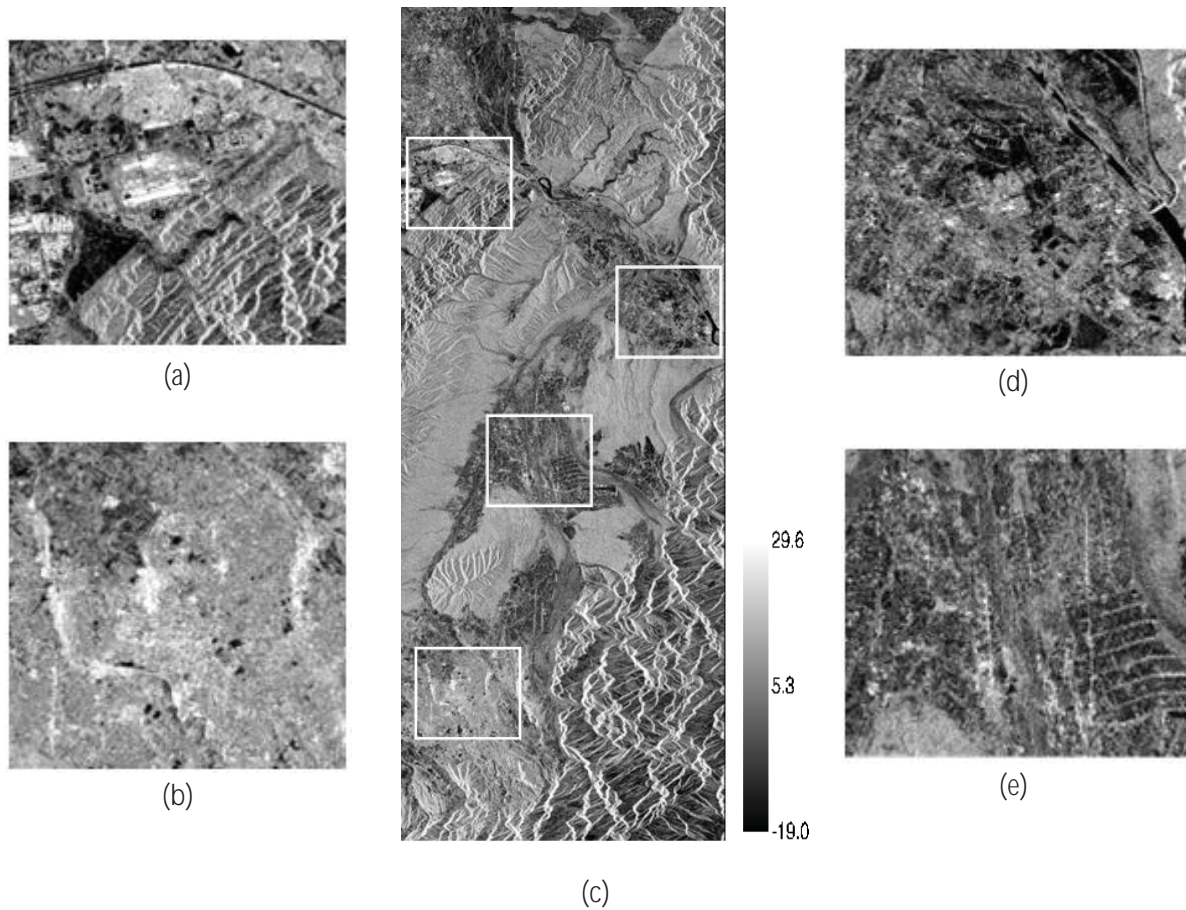
Figure 5-10 (a)Urban area (Haridwar), (b) Dehradun, displaying bright response in wire scattering power image. (c) Wire scattering power. Clearly visible small urban settlements in (d) Rishikesh and, (e) Flat terrain near airport in wire scattering power image.

5.4.   Analysis

The scattering response of the earth features with respect to each decomposed power image obtained from the cosine squared decomposition was analysed by selecting a transect from the image. For analysis of the decomposed results, point samples were extracted from all the decomposed power images utilising the stratified random sampling. Samples containing 100 pixels from each of the three major urban areas – Haridwar, Dehradun and Rishikesh were extracted from the five power images obtained from the three decomposition methods. In addition to these, few more samples were extracted from the forest area to compare the changes in the backscatter on applying cosine squared distribution. In some samples, the pixel values were found to be -NaN (Not a Numeral) and -Infinity (-∞). Such values were replaced by a dummy value (0.001) for carrying out analysis

5.4.1.   Transect Analysis

A transect containing about 500 pixels was selected from an urban patch in the Haridwar region from the geocoded power images. The location of the transect is shown in Figure along with the corresponding location in the Pauli RGB image, MCSM decomposed RGB image and grayscale power image. The backscatter values of the pixels along this transect were plotted. The variations in the power values of the pixels were analysed. The backscatter response was compared to the earth features, represented by the corresponding pixels, using Google Earth. The surface scattering power illustrated varying negative magnitude in general, with very few pixels showing positive power values. Most of pixels with positive values were concentrated between the point 115 to point 139. Few pixels exhibited power values -Infinity (-∞) . The overall magnitude of the surface scattering power along the transect was found in the range of -18 dB to 6 dB. In case of double bounce scattering power, more variation was observed as compared to the surface scattering. Positive power values were displayed by pixels situated between point 104 and 164. Some pixels were also observed with high negative power values. The magnitude of the double bounce power was in the range of -22 dB to 10 dB. The samples from the volume scattering power exhibited interesting behaviour. Firstly, most of the sample pixels had -NaN (Not a Numeral) value but not a single -Infinity (-∞) value. All such values were replaced by a dummy value of 0.001. Secondly, the remaining values were found to have positive magnitude only. The samples from the helix scattering power image had pixels with high negative magnitude with very few pixels displaying low positive magnitude. These positive pixels lied between point 124 to 136. The wire scattering power displayed more positive values with a high concentration between point 107 to 175.
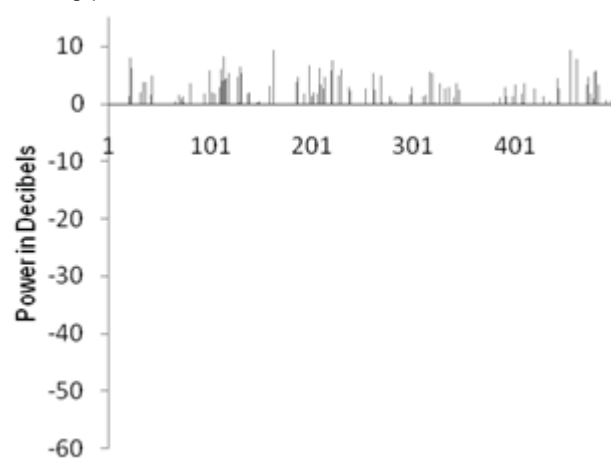
The plots for pixel values from each scattering power obtained from the MCSM decomposition with cosine squared distribution is given in the figure . The vertical axis in the plots represents the decomposed power in decibel scale and the horizontal axis represents the point number of pixels.
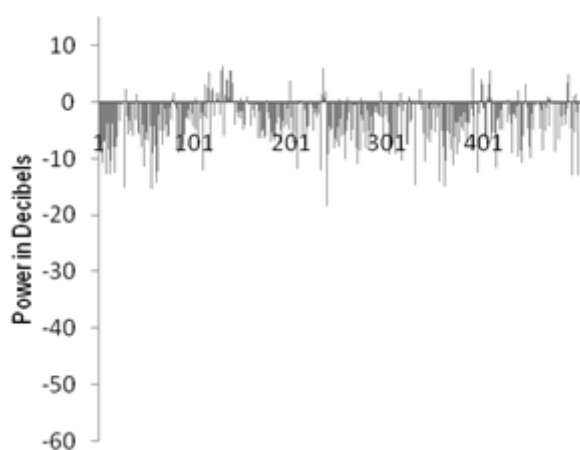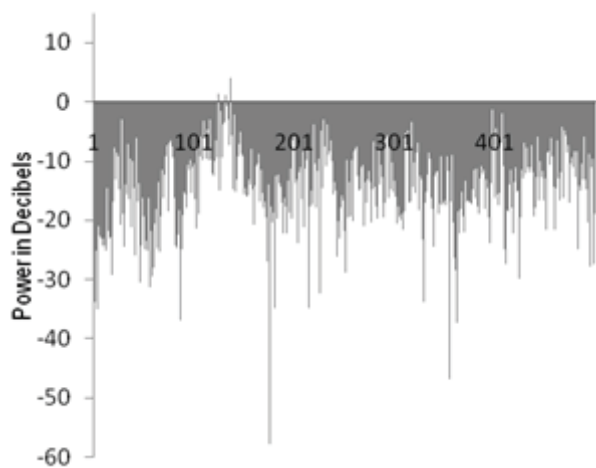
(a)Surface scattering power
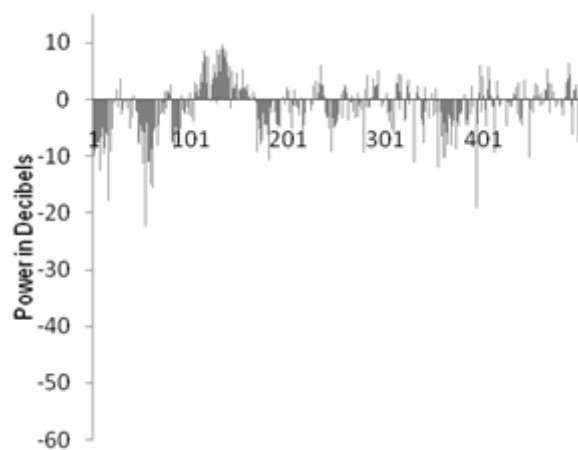
(b) Double bounce scattering power
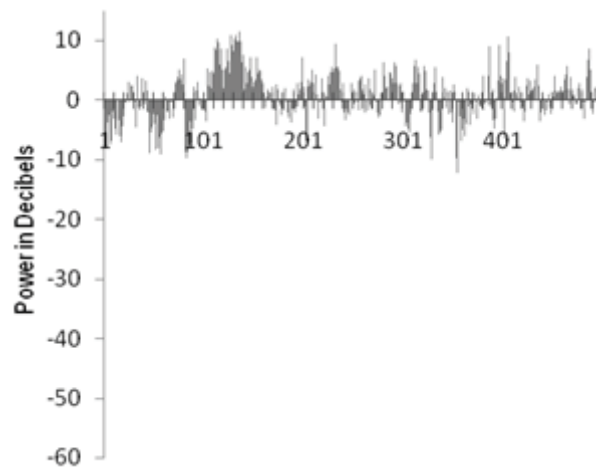

(c) Volume scattering power
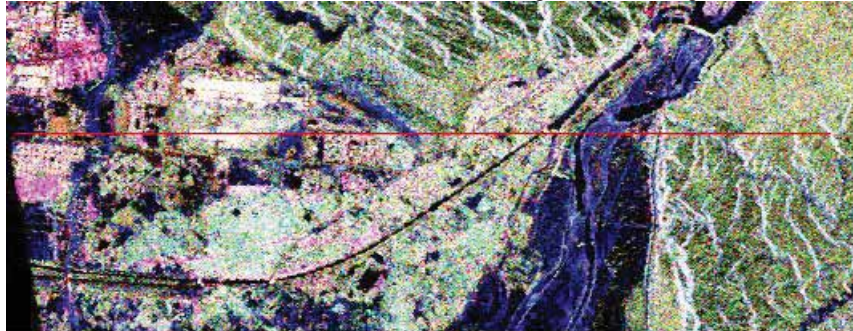

(d) Helix scattering power
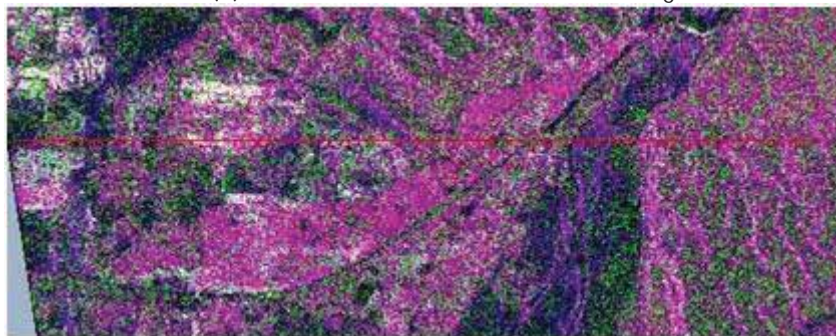
(e) Wire scattering power

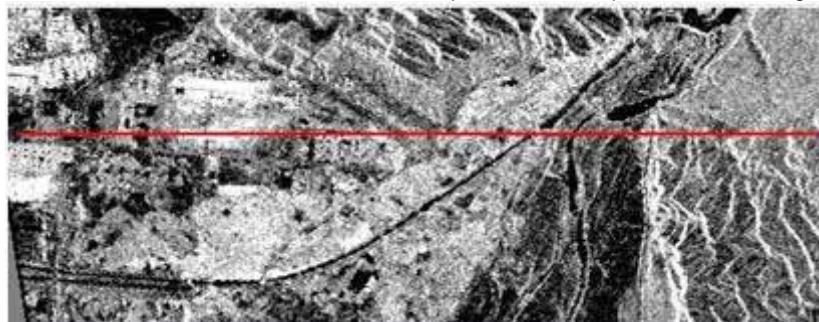Figure 5-11 Scattering powers of the pixels along the transect

(a) Transect location in Google Earth image

(b) Transect location in Pauli RGB image

(c) Transect location in Cosine Squared Decomposed RGB image

(d) Transect location in Decomposed Power image
Figure 5-12 Location of the Transect

5.4.2. Regression Analysis

The co-polarised response from the radar backscatter are related to the surface and double bounce scattering power, whereas the cross-polarised response is related to the volume, helix and wire scattering power. In terms of coherency matrix elements, the T_{11} and T_{22} elements are represent the co-polarised response, related to surface and double bounce power respectively. The T_{33} element represents the cross-polarised response. In this section, the relation between these responses and the corresponding scattering powers has been analysed using regression analysis using linear model. For this analysis, a random sample of 100 pixels were selected from the urban areas, from each of the three diagonal coherency elements and the corresponding scattering power images obtained from the MCSM decomposition using cosine squared distribution.

Figure 5-13 shows the relation between the surface scattering power and the co-pol response (T_{11} element). This relation was analysed using the regression analysis employing linear model. Good correlation was observed with a $R^2 = 0.663$. The residual plots were also analysed for further verification. the sum of the residuals was close to zero and the residual plots were also random. This means that the linear model was appropriate for describing the relation between Similar relation was observed between the double bounce power and the T_{22} element with $R^2 = 0.662$. These plots are given in Figure 5-14.
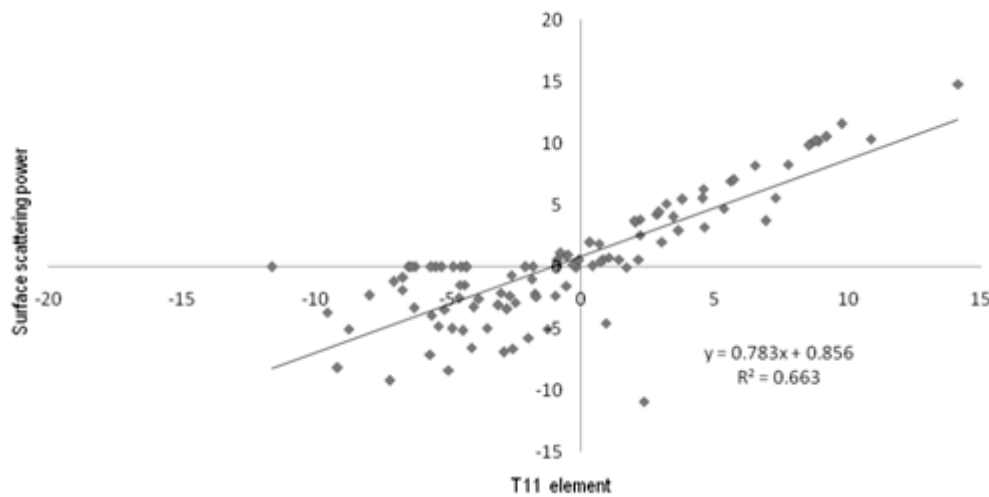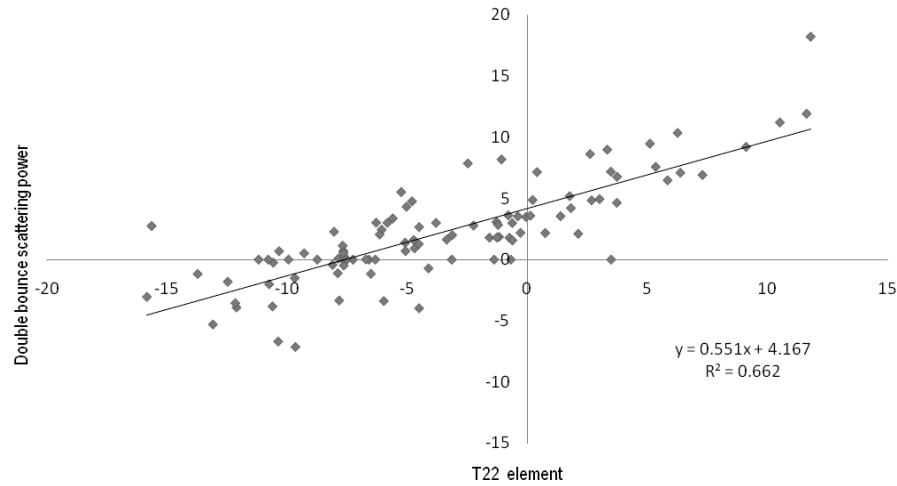

(a) Relation between Surface scattering power and T11 element
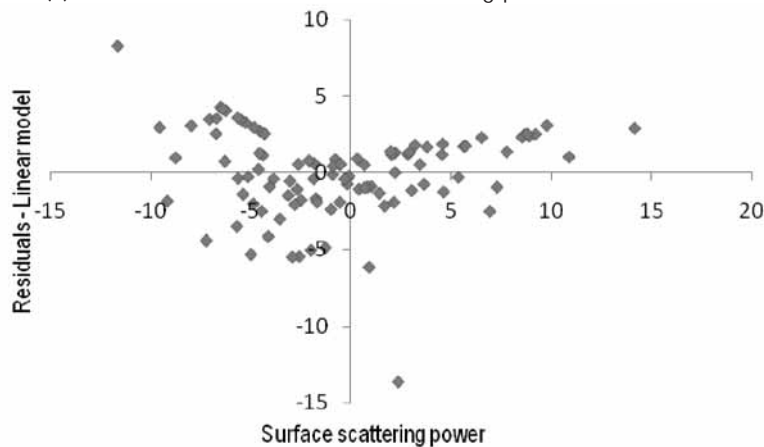
(b) Residual plots for linear model for Surface scattering power
Figure 5-13 Relation between the (a)surface scattering power and T11 element and (b) corresponding residual plots

(a) Relation between Double bounce scattering power and T22 element
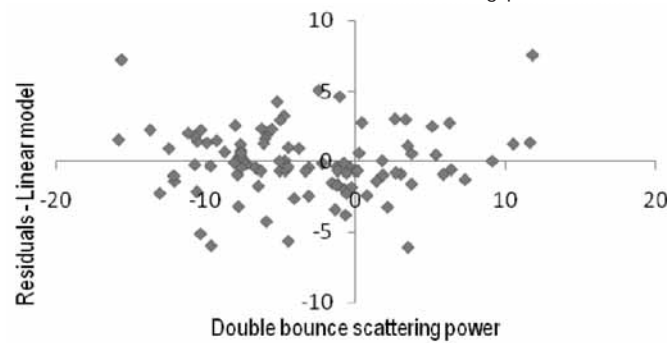
(b) Residual plots for linear model for Double bounce scattering power

Figure 5-14 (a) Relation between Double bounce scattering power and T22 element and (b) the corresponding residual plots

The volume scattering power is obtained from the cross-polarised response from the vegetation canopy. In case of the urban scatterers, the helix and wire scattering power are associated with the cross-polarised response generated from the complex oriented man-made structures and the randomness in distribution of various scatterers. Therefore, the relation between these three scattering powers and the cross pol response was analysed. The model fit employed was linear model which illustrated a very low correlation with R^2 in the range of 0.2 - 0.3 for all the three scattering powers. This indicated that the linear model was not a best fit model for describing this relation. The plots for the regression analysis and the corresponding residual plots are given in Figure 5-14 and 5-15.
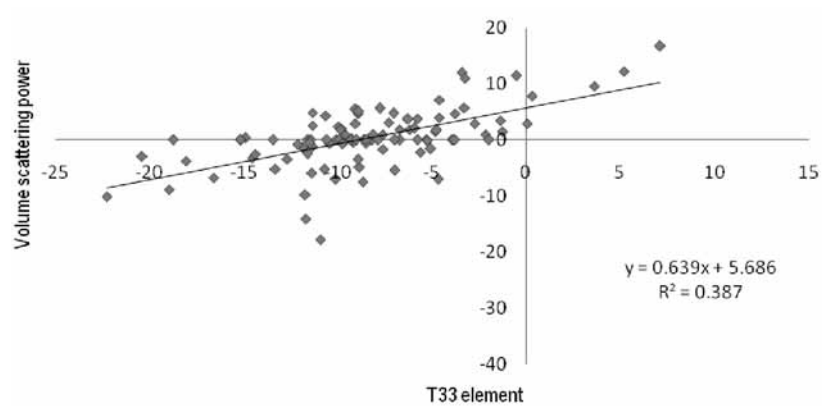
(a)   Relation between Volume scattering power and T33 element
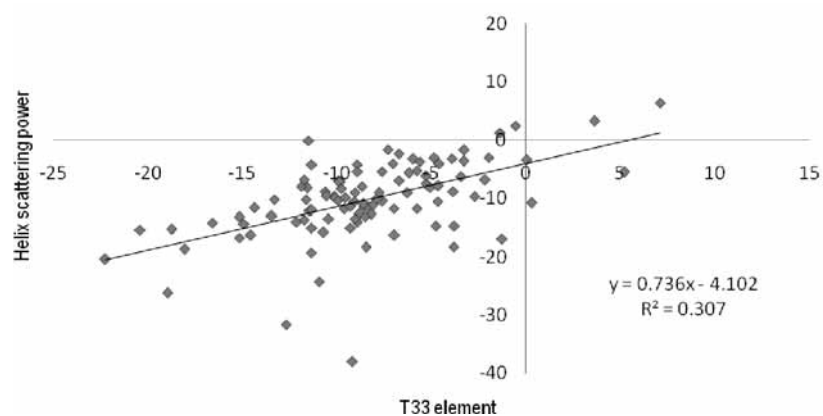
(b)   Relation between Helix scattering power and T33 element
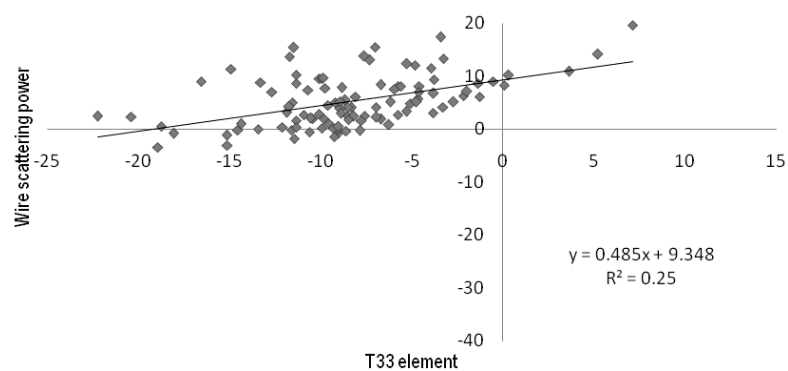
(c)   Relation between Wire scattering power and T33 element

Figure 5-15Relation between the (a)Volume scattering power, (b) Helix scattering power (c) Wire scattering power and T33 element
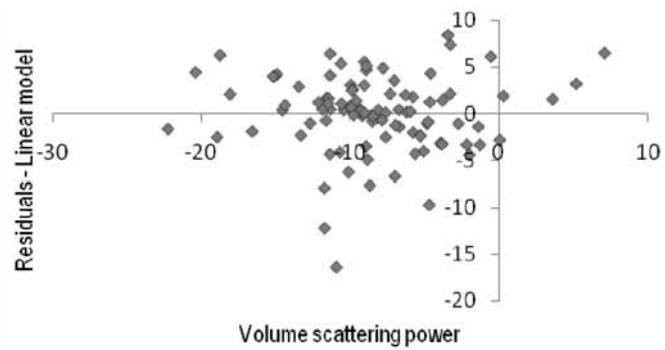
(a) Residual plots for linear model for Volume scattering power
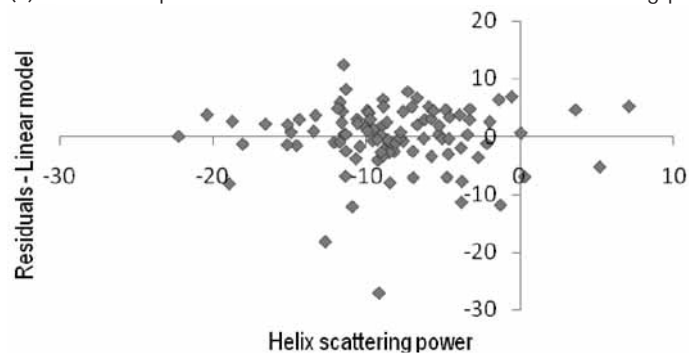
(b) Residual plots for linear model for Volume scattering power
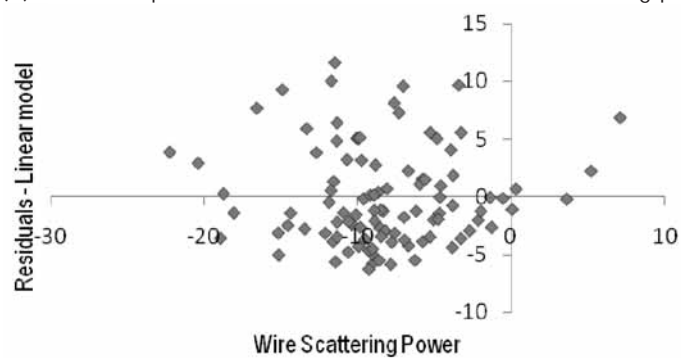
(c) Residual plots for linear model for Volume scattering power
Figure 5-16 Residual plots for the (a)Volume scattering power, (b) Helix scattering power (c) Wire scattering power

5.4.3.   Comparison of Double bounce and Volume Scattering Powers

The decomposed results obtained from the three techniques were compared and analysed for understanding the changes introduced by the cosine squared distribution

On comparison of the samples, as expected by the research, the double bounce scattering power was found to be increased and the volume scattering power was found to be decreased for urban areas with the use of cosine squared distribution. But an interesting observation was that the double bounce power from the forest areas was also found to be increased. In fact, it turned into positive values for cosine squared distribution.
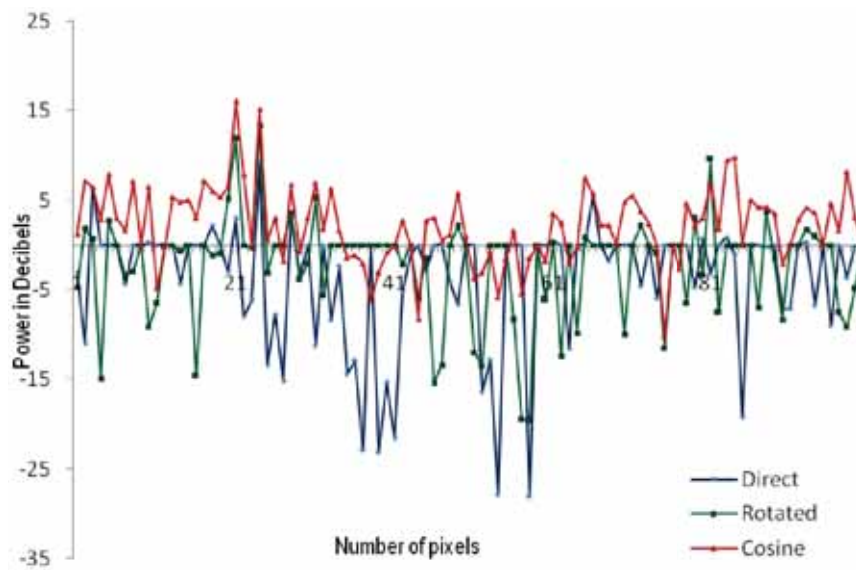
Figure 5-17 Double Bounce power from urban areas
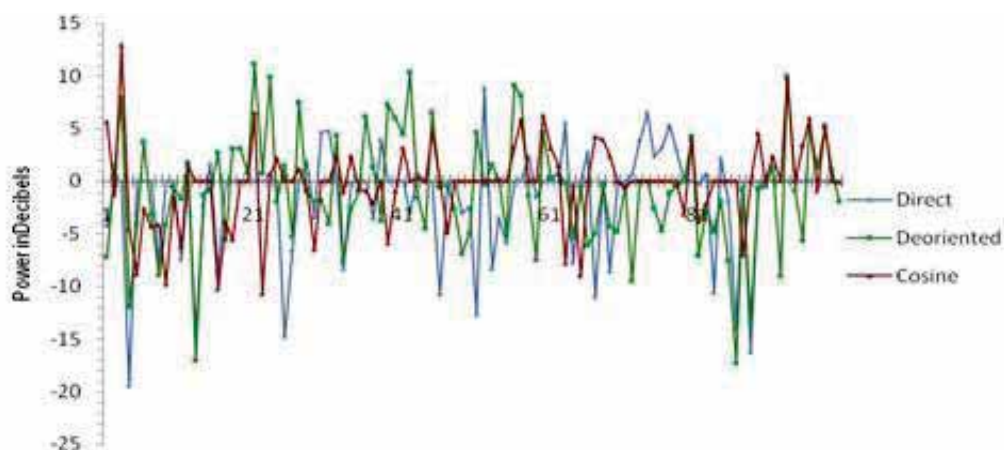
Figure 5-18 Volume power from urban area
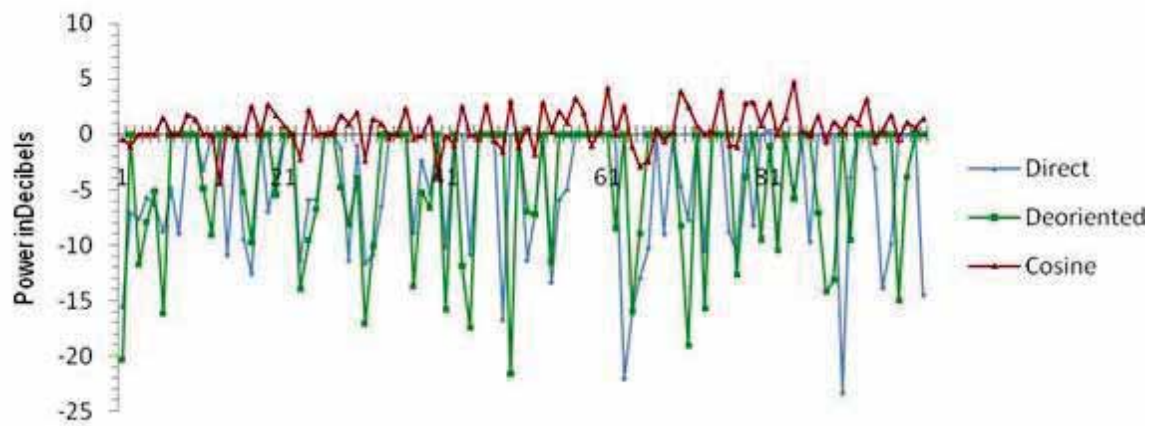
Figure 5-19 Double bounce Power from the forest
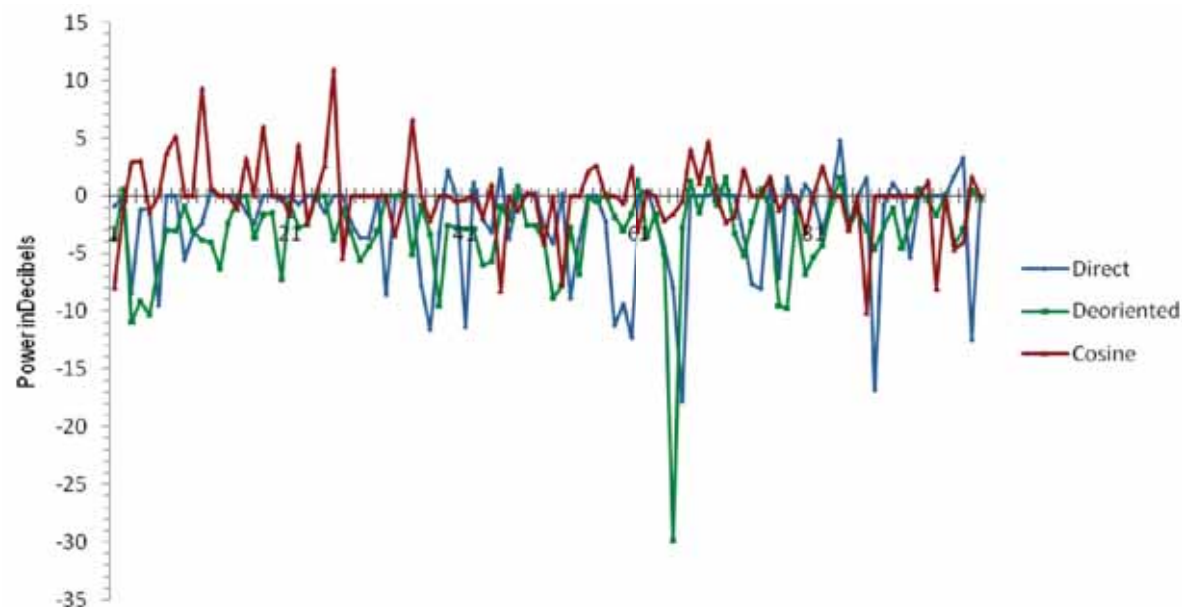
Figure 5-20 Volume power from the forest

5.4.4.   Patch Analysis

A patch was selected from the urban area present in the image. The scattering contribution i.e. the pixel values from each of the five components was extracted from the three decomposition results. The total contribution of the five scattering powers i.e., P_s, P_d, P_v, P_h and P_w from the patch was plotted in the form of a pie chart for the three decomposition methods. These pie charts are displayed in Figure .

(a) Direct MCSM Decomposition

(b) Deoriented MCSM Decomposition

(c) MCSM Decomposition with Cosine squared Distribution
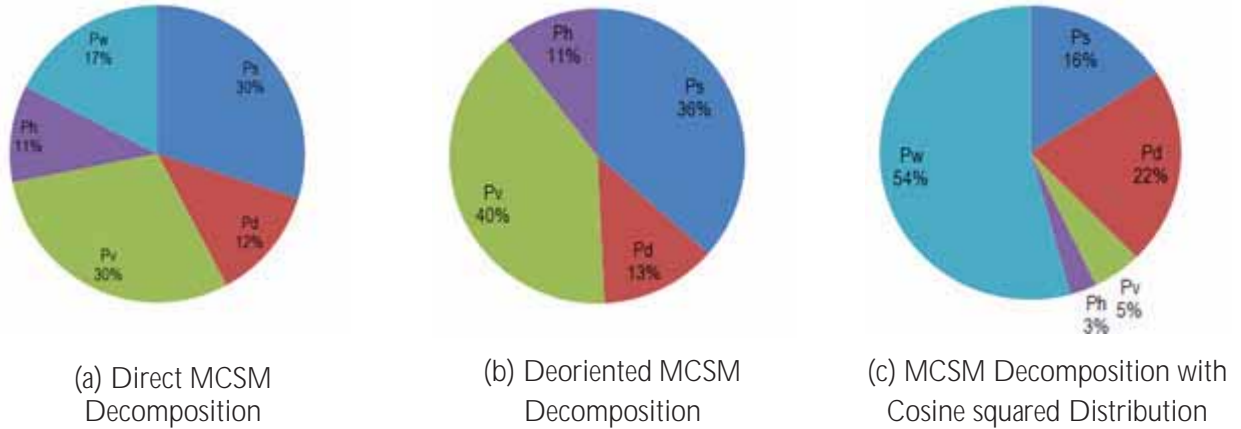
Figure 5-21 Pie charts illustrating power contribution from each scattering power.

It can be observed from the above figure that the contribution of the volume scattering power P_v, which was 30 % for direct decomposition, first increased to 40% on applying deorientation and then decreased to only 5% for the cosine square distribution. The surface scattering power P_v also displayed similar behaviour. It was 30% in the direct decomposed image, and then it increased to 36% in case of deorientation and decreased in case of cosine squared distribution. The double bounce power P_d, displayed an increase of 1% with deorientation whereas in case of the cosine squared distribution it increased to 22%. The contribution of the helix scattering power P_h was found to be same in the direct and the deoriented decomposed results, whereas in case of cosine squared distribution it decreased to only 3%. The wire scattering power P_w illustrated significant variation. P_w contributed to 17% of the total backscatter for direct decomposition. In case of deorientation it reduced to zero. But for cosine squared distribution, it contributed to more than half of the total backscatter, with a percentage of 54.

6. DISCUSSIONS

A detailed discussion of the present research is presented in this chapter. The methodology adopted for this research has been reviewed and the possible limitations have been discussed. This is followed by the discussion of the analysis and interpretation of the obtained results.

6.1. Importance of Orientation Angle Shifts Compensation

The present research is focused on the compensation of the polarisation orientation angle shifts caused by the terrain slopes and oriented scatterers, mostly found in urban areas. Past research has proven that the orientation angle shifts are responsible for high cross-polarisation intensity in the backscattered radar signal. This often results in overestimation of volume scattering power, especially from scatterers which are a cause of orientation angle shifts. In case of urban areas, the compensation of these shifts becomes an essential requirement. The shape, orientation, distribution of buildings and street pattern are some factors that affect the backscatter from the urban areas. As stated in past research, due to the orientation angle shifts observed from the urban areas, it becomes difficult to distinguish between the oriented urban scatterers and the vegetation, as both demonstrate high cross polarised response. Therefore, often the oriented urban scatterers are decomposed into the volume scattering power. This results in errors in the decomposition of polarimetric data containing such areas. Many techniques have been implemented in the past, to reduce the effects of orientation angle shifts. Generally, these are based on rotating the target matrix with the observed orientation angle shifts. In the present research, a different approach is employed. The orientation of the basic matrices is first fixed to a particular orientation by rotating the target scattering vector by angle θ. The corresponding coherency matrices from these rotated scattering matrices are derived. The cosine squared distribution is implemented on each of the derived coherency matrix except for helix scattering because of its roll-invariant nature. This distribution is used to incorporate the variation or randomness in the orientation of the scatterers. Therefore, in this way, all the possible orientations of the scatterers are considered while deriving the coherency matrices for each scattering mechanism. The concept of probability distribution of the orientation of the scatterers has been used previously for the case of volume scattering. However, the orientation of the scatterers can exhibit variations irrespective of the scattering mechanisms demonstrated by them. The variations in the orientations of the surface scatterers can be caused by the terrain slopes. In case of urban scatterers, dihedral and trihedral corner reflectors, similar variations can occur due to the orientation of these structures. The wire scattering in itself is described by the orientation of a dipole around the radar line of sight. Therefore, wire component also displays orientation variations. To consider the orientation variations in all these scattering components, the cosine squared distribution is applied to each of the four coherency matrices- surface, double bounce, volume and wire scattering. The potential of this approach in correctly decomposing oriented urban scatterers is demonstrated well by the obtained results. The accurate decomposition of polarimetric data containing urban areas is expected to enhance the application of SAR polarimetry in urban context.

6.2. Scattering Response of Urban Features

In case of surface scattering power, the positive values were observed from the roofs of the large buildings. The positive power values for the double bounce scattering mechanisms were observed from large building blocks present in the Haridwar region. It also included a small dip in the power values

which was caused by the gap in the building structure where small trees and a road were present. Most of the high negative power values in surface power and double bounce power were observed from the river and its banks, along with some small urban settlements. The pixels displaying -Infinity values, which indicated zero response from the earth feature, contained the response from the water surface as well as response from the barren land. In case of water surface, this response can be easily explained as the water absorbs major portion of the incident radiation. The water surface represents a smooth surface, which is known to exhibit specular reflectance. Therefore, no returns are obtained from water surface which implies zero backscatter value. The edge of the building was found to be responsible for high positive values in the five scattering powers. The volume scattering power also displayed high positive values for the building block, though less than the double bounce power. The large building block in the path of the transect represented a strong urban scatterer for the radar signals and therefore was responsible for observed positive power values.

6.3.   Wire Scattering Power

The most interesting output of this research was the wire scattering power obtained from the MCSM decomposition after implementing the cosine squared distribution. The urban scatterers could be clearly identified in the wire scattering power image. Even the minute urban features present in the image were clear and bright. In addition to this, high backscatter response was also observed from the forest areas. This might be due to the fact that the wire scattering was actually modelled from a thin wire or dipole target described by the orientation angle about the radar line of sight. The concept of wire target was originally developed for coherent or isolated scatterers, generally found in urban scenarios. But if the forest or vegetation canopy is considered, then the branches of a tree may also act as a wire scatterer for the incident radar wave. In fact, the volume scattering power is modelled from a cloud of randomly oriented dipoles. Therefore, the high wire scattering power from the forest can be explained by the above concepts.

6.4.   The five scattering mechanisms and the co-pol and cross-pol response

The surface scattering power and the double bounce scattering power can be directly related to the co-pol response represented by the T_{11} and T_{22} elements of the coherency matrix. This can also be explained by the physics behind these scattering mechanisms. The surface scattering is modelled from Bragg's scattering from slightly rough surface. Such surfaces are known to generate the HH response. Similarly, vertical structure such as a wall of a building gives more response in VV polarisation. The double bounce is also generated from such structures. The relation between the cross-pol response and the volume, helix and wire scattering response could not be describes by a linear model. The complex interactions which give rise to these scattering mechanisms can be the reason for this.

6.5.   Effect of Cosine Squared Distribution

On comparison of the decomposition results generated by the cosine squared distribution and the direct and deoriented results, the expected variations were observed. The double bounce power in the urban areas was found to be increased along with a decrease in the volume scattering power. On careful analysis, most of the urban settlements were decomposed into double bounce, helix and wire components. But some unexpected results were also obtained on using the cosine squared distribution. This was the increase in the double bounce power in the forest region as well as the high contribution of wire scattering power

6.6.   The -NaN and -Infinity Values

The pixels with negative values illustrated backscatter values as –NaN which implies that the pixel value is recognised as 'Not a Number' according to the specified data format. In this study, the data is specified as double floating point precision value. When the linear scale decomposed images are converted to the decibel scale, which involves the logarithm of the linear value, then the pixels with negative values generate complex values and the pixels with zero values results in pixel value of negative infinity (- ∞). As the specified data format cannot include complex values, therefore such values are categorised as –NaN while processing the image.

6.7.   Validation

In order to validate the obtained decomposition results from the cosine squared distribution, the scattering response of the urban features was observed in the decomposed power images. The bridge present near Rishikesh and Haridwar were selected for this purpose, as these two sites were perfect for illustrating high double bounce scattering power. Moreover, these two sites also generated high orientation angle shifts in the order of 20º to 40º. On comparing the pixel values of these two sites, the dominance of double bounce power over the volume scattering power was verified. This can also be visualised from the RGB color coded decomposed images from the three decomposition results. The double bounce power is coded as Red, Volume power as green and surface power as blue. In the direct decomposition results, there was no clear discrimination between the bridge and the surroundings due to presence of different colored pixels. In case of the deoriented decomposition, few green pixels can be observed indicating the dominance of volume scattering power. For the cosine squared decomposition, the white pixels represent the higher double bounce as compared to volume and surface scattering. The bright green pixels were obtained as the values of double bounce and single bounce turned to -NaN and - Infinity.
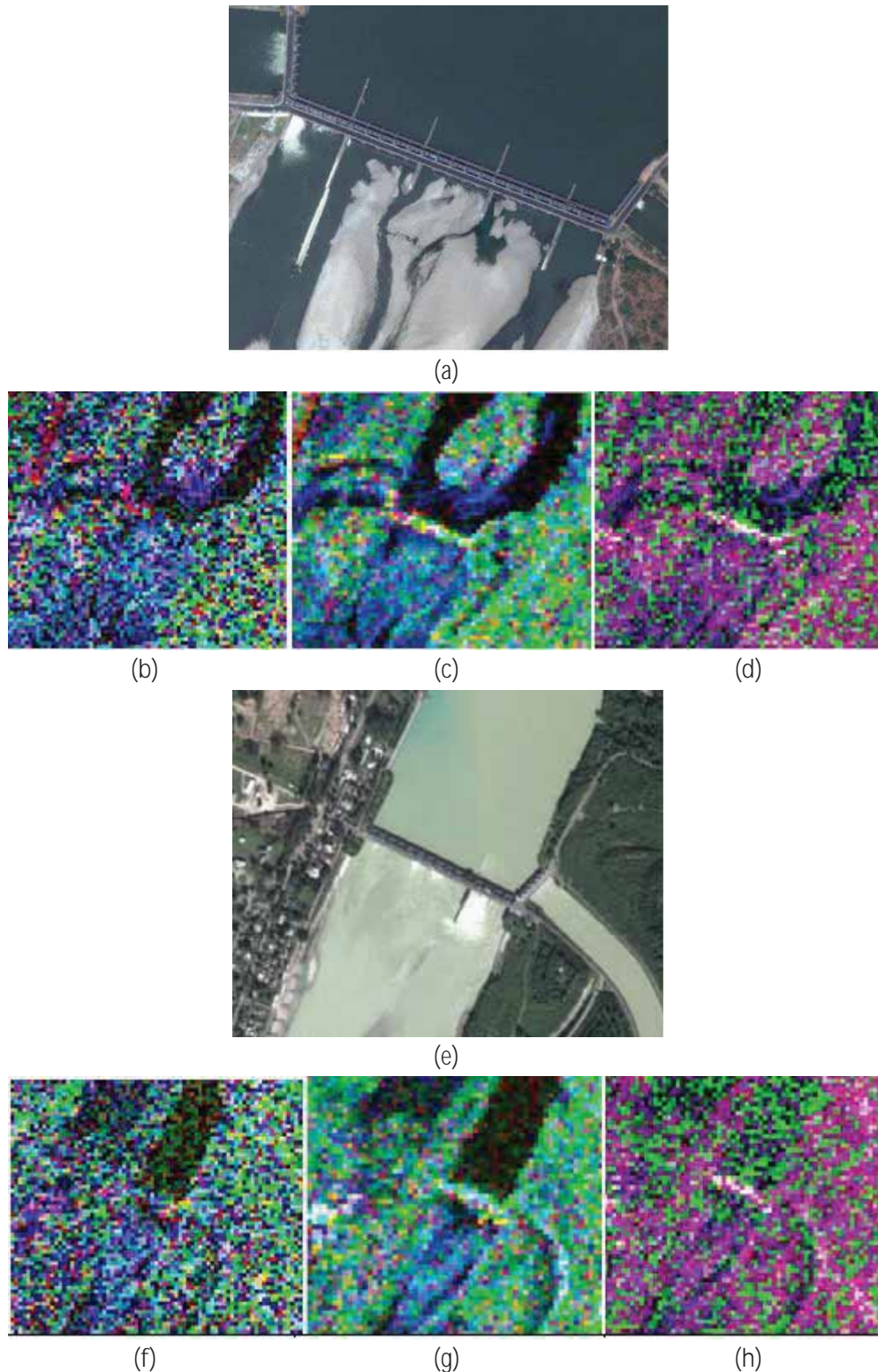
Figure 6-1 Bridge near Haridwar city(Ram jhoola)(a)in Google Earth, in RGB color coded image with Pd as Red, Pv as Green, Ps as Blue of (b)Direct MCSM Decomposition (c)Deoriented MCSM Decomposition (c) Cosine squared MCSM Decomposition. Bridge near Rishikesh city(Laxman jhoola)(e)in Google Earth, in RGB color coded image of (f)Direct MCSM Decomposition (g)Deoriented MCSM Decomposition (h) Cosine squared MCSM Decomposition.

Similar observations were made from some other urban areas which represented small settlements. Such areas are highlighted in the Figure 6-2. These settlements were earlier decomposed into volume scattering power, but with the use of cosine squared distribution, these were correctly decomposed into double bounce.
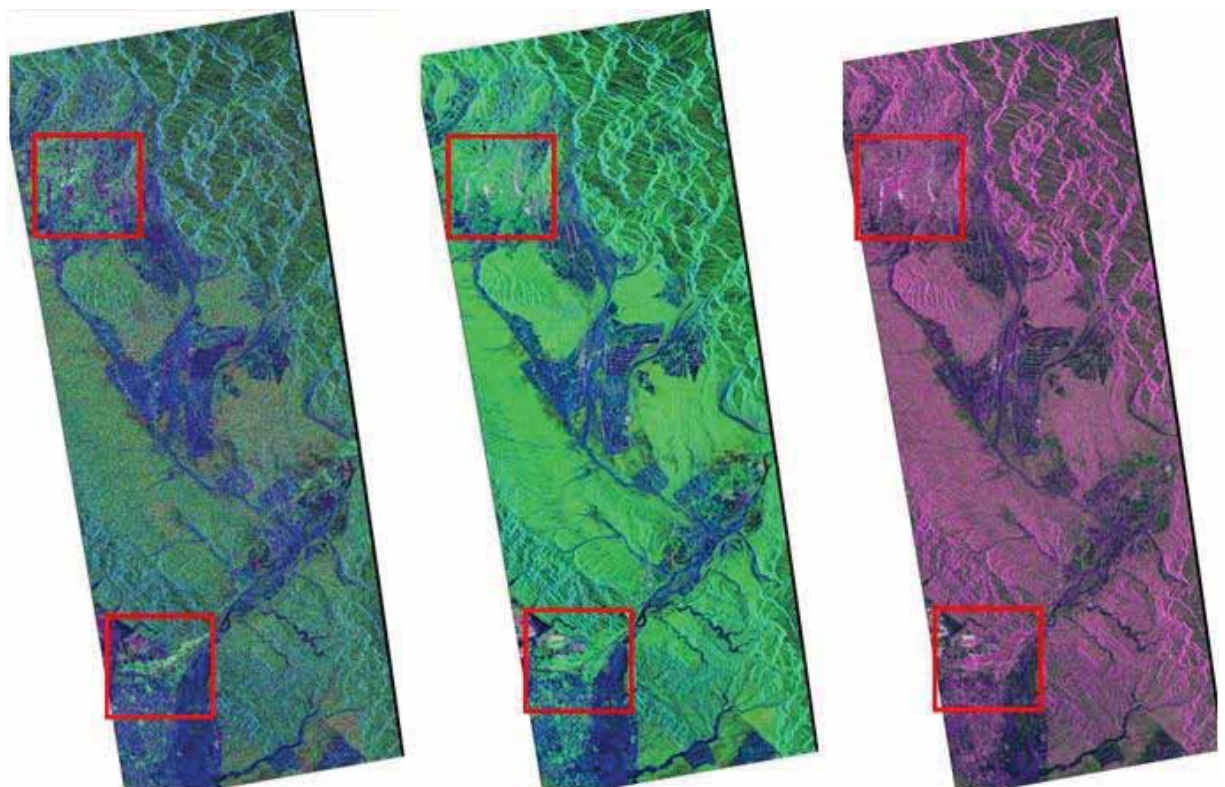
(a) Direct MCSM Decomposition

(b) Deoriented MCSM Decomposition

(c) MCSM Decomposition with Cosine Squared Distribution

Figure 6-2 RGB color coded images with double bounce power as Red, volume power as Green, surface power as Blue for (a) direct (b)deoriented (c) Cosine squared MCSM decomposition
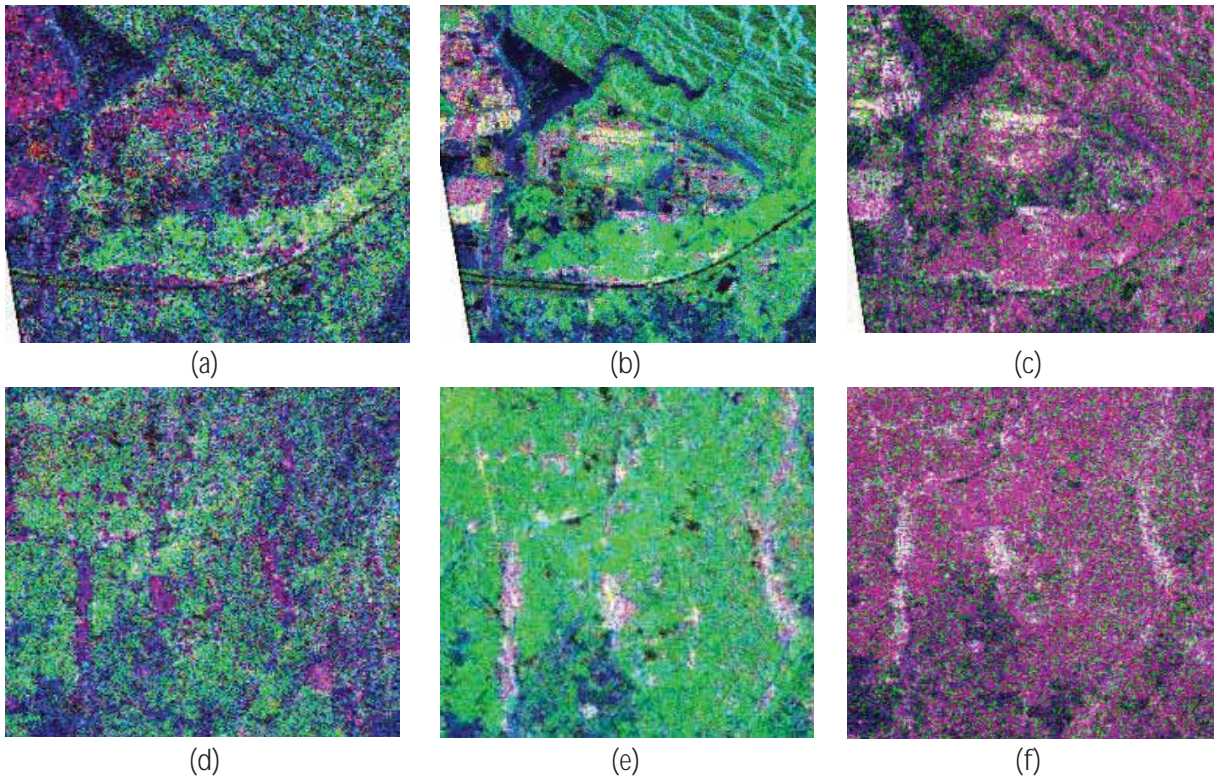
Figure 6-3 Changes observed in the urban areas of Haridwar in (a) direct, (b) deoriented, (c) cosine squared MCSM decomposition and , Dehradun in (d) direct, (e) deoriented, (f) cosine squared MCSM decomposition.

The Figure 6-3 displays the changes observed in the decomposed results. The Haridwar urban area is presented in the Figure 6-3 (a) direct, (b) deoriented, (c) cosine squared MCSM decomposition. It can be easily observed that the small urban settlements are correctly decomposed into the double bounce power (pink pixels) in the cosine squared decomposition. Similar observations can be made from the Dehradun city in the (d) direct, (e) deoriented, (f) cosine squared MCSM decomposition.

7.   CONCLUSIONS AND RECOMMENDATIONS

Following conclusions with respect to the research questions can be made on the basis of the analysis of the obtained results.

7.1.   How the cosine squared distribution describes the prominent scattering mechanisms in urban areas i.e., double bounce, helix and wire?

The double bounce and the wire scattering powers were well described by the cosine squared distribution. This can be observed from the increased response of these scattering powers from the urban scatterers, oriented as well as parallel with respect to radar line of sight. This increase in the response can be associated to the physical characteristics of such urban scatterers. In case of helix scattering, the cosine squared distribution is not required, as the helix component is roll-invariant. Therefore it is not affected by the orientation angle shifts.

7.2.   What is the relation between the different polarimetric response (co-pol and cross-pol) and the five scattering mechanisms?

The surface scattering and the double bounce scattering can be directly related to the T_{11} and T_{22} elements or the co-pol response. But in case of the volume, helix and wire components, their relation with the cross-pol response require deep analysis to characterise certain behaviour. As these three scattering mechanisms involve complex interactions, therefore it requires the understanding of such interactions and the structures responsible for it.

7.3.   Does the cosine squared distribution improve the information content and accuracy of the results of the Multiple Component Scattering Model decomposition?

From the observed results and their analysis, it can be concluded that the cosine squared distribution improved the information content and the accuracy of the MCSM decomposition in the context of urban scatterers. Less number of negative pixels was observed for the three prominent scattering mechanisms in urban areas- double, helix and wire. Most of the urban settlements were correctly dominated by the above three scattering powers, rather than volume scattering power.

7.4.   How to validate the obtained results from the Multiple Component Scattering Model decomposition?

The objective of using cosine squared distribution was to compensate the effect of the orientation angle shifts produced by the urban scatterers, in order to prevent the inaccurate decomposition of scattering response from the urban features. Since the urban scatterers are discreet in nature and can be easily identified in the backscatter power image due to their characteristic bright response, scattering response from such urban scatterers in the decomposed power images was analysed.

7.5.   Recommendations

Further improvement of the decomposition approach given in this research may be achieved by-

- Compensating the orientation angle shifts on the basis of orientation angle shifts observed from each pixel, rather than the mean orientation angle shift for the whole image. This can result in more accurate compensation of these shifts.

- Using the nth-power cosine squared distribution, as proposed by Arii. The randomness of the orientation of the scatterer can be described by 'n'. As different features have different randomness, therefore 'n' can be applied on the basis of each feature class.
- Analysing the cause of the negative pixels and reducing the number of such pixels. The negative pixels usually in the radar backscattered power. However the reasons for occurrence of such pixels are still an active topic for research. An attempt for this has been recently made in Yamaguchi et al.

LIST OF REFERENCES

[1]   J. A. Richards, *Remote Sensing with Imaging Radar*. Springer, 2009.

[2]   Canada Centre for Remote Sensing, "Advanced Radar Polarimetry Tutorial," *www.ccrs.nrcan.gc.ca*. [Online]. Available: http://www.ccrs.nrcan.gc.ca/resource/tutor/polarim/pdf/polarim_e.pdf. [Accessed: 25-Dec-2011].

[3]   Canada Centre for Remote Sensing, "Educational Resources for Radar Remote Sensing," *www.ccrs.nrcan.gc.ca*, 18-Oct-2011. [Online]. [Accessed: 14-Feb-2012].

[4]   European Space Agency, "SAR Polarimetry Advanced concepts EPottier," *www.earth.eo.esa.int*, 16-Oct-2011. .

[5]   European Space Agency, "Single Multi Polarization SAR data," *www.envisat.esa.int*, 18-Sep-2011. .

[6]   A. Freeman and S. L. Durden, "A three-component scattering model for polarimetric SAR data," IEEE Transactions on Geoscience and Remote Sensing, vol. 36, no. 3, pp. 963-973, May 1998.

[7]   J.-S. Lee and E. Pottier, *Polarimetric Radar Imaging: From Basics to Applications*, 1st ed. CRC Press, 2009.

[8]   Y. Yamaguchi, T. Moriyama, M. Ishido, and H. Yamada, "Four-component scattering model for polarimetric SAR image decomposition," *IEEE Trans. Geosci. Remote Sensing*, vol. 43, no. 8, pp. 1699-1706, Aug. 2005.

[9]   H. Kimura, K. P. Papathanassiou, and I. Hajnsek, "Polarization orientation effects in urban areas on SAR data," in *Geoscience and Remote Sensing Symposium, 2005. IGARSS '05. Proceedings. 2005 IEEE International*, 2005, vol. 7, pp. 4863- 4867.

[10] Y. Yamaguchi, A. Sato, W. Boerner, R. Sato, and H. Yamada, "Four-Component Scattering Power Decomposition With Rotation of Coherency Matrix," *IEEE Transactions On Geoscience And Remote Sensing*, vol. 49, no. 6, pp. 2251-2258, 2011.

[11] Lamei Zhang, Bin Zou, Hongjun Cai, and Ye Zhang, "Multiple-Component Scattering Model for Polarimetric SAR Image Decomposition," *IEEE Geoscience and Remote Sensing Letters*, vol. 5, no. 4, pp. 603-607, Oct. 2008.

[12] M. Arii, J. J. van Zyl, and Yunjin Kim, "A General Characterization for Polarimetric Scattering From Vegetation Canopies," *IEEE Transactions on Geoscience and Remote Sensing*, vol. 48, no. 9, pp. 3349-3357, 2010.

[13] U. Soergel, "Review of Radar Remote Sensing on Urban Areas," in *Radar Remote Sensing of Urban Areas*, vol. 15, U. Soergel, Ed. Dordrecht: Springer Netherlands, 2010, pp. 1-47.

[14] D. Massonnet and J.-C. Souyris, *Synthetic Aperture Radar Imaging*. EFPL Press, 2008.

[15] J. S. Lee, T. L. Ainsworth, D. L. Schuler, D. Kasilingam, and W. M. Boerner, "Interpreting off-diagonal terms in polarimetric coherency matrix," in *Geoscience and Remote Sensing Symposium, 2001. IGARSS '01. IEEE 2001 International*, 2001, vol. 2, pp. 913-915 vol.2.

[16] J. S. Lee, D. L. Schuler, T. L. Ainsworth, and W.-M. Boerner, "Polarization orientation estimation and applications: a review," in *IGARSS 2003. 2003 IEEE International Geoscience and Remote Sensing Symposium. Proceedings (IEEE Cat. No.03CH37477)*, Toulouse, France, pp. 428-430.

[17] H. Kimura, "Radar Polarization Orientation Shifts in Built-Up Areas," *IEEE Geoscience and Remote Sensing Letters*, vol. 5, no. 2, pp. 217-221, Apr. 2008.

[18] K. Iribe and M. Sato, "Analysis of polarization orientation angle shifts by artificial structures," *IEEE TRANSACTIONS ON GEOSCIENCE AND REMOTE SENSING*, vol. 45, no. 11, pp. 3417-3425, Nov. 2007.

[19] Jong-Sen Lee, D. L. Schuler, and T. L. Ainsworth, "Polarimetric SAR data compensation for terrain azimuth slope variation," *IEEE Trans. Geosci. Remote Sensing*, vol. 38, no. 5, pp. 2153-2163, Sep. 2000.

[20] Feng Xu and Ya-Qiu Jin, "Deorientation theory of polarimetric scattering targets and application to terrain surface classification," *IEEE Transactions on Geoscience and Remote Sensing*, vol. 43, no. 10, pp. 2351- 2364, Oct. 2005.

[21] J.-S. Lee and T. L. Ainsworth, "The Effect of Orientation Angle Compensation on Coherency Matrix and Polarimetric Target Decompositions," *IEEE Trans. Geosci. Remote Sensing*, vol. 49, no. 1, pp. 53-64, Jan. 2011.

[22] M. Arii, "Retrieval of soil moisture under vegetation using polarimetric radar," Thesis, CALIFORNIA INSTITUTE OF TECHNOLOGY, Pasadena, California, 2009.

[23] S. R. Cloude and E. Pottier, "A review of target decomposition theorems in radar polarimetry," *IEEE Trans. Geosci. Remote Sensing*, vol. 34, no. 2, pp. 498-518, Mar. 1996.

[24] A. Freeman and S. L. Durden, "Three-component scattering model to describe polarimetric SAR data," *Proceedings of SPIE*, vol. 1748, no. 1, pp. 213-224, Feb. 1993.

[25] E. Krogager, W. Boerner, and S. Madsen, "Feature-motivated Sinclair matrix (sphere/diplane/helix) decomposition and its application to target sorting for land feature classification," *WIDEBAND INTERFEROMETRIC SENSING AND IMAGING POLARIMETRY*, vol. 3120, pp. 144-154, 1997.

[26] T. Moriyama, "Polarimetric SAR Image Analysis Using Model Fit for Urban Structures," *IEICE Transactions on Communications*, vol. E88–B, no. 3, pp. 1234-1243, Mar. 2005.

[27] Lamei Zhang, Bin Zou, Hongjun Cai, and Ye Zhang, "Multiple-Component Scattering Model for Polarimetric SAR Image Decomposition," *IEEE Geoscience and Remote Sensing Letters*, vol. 5, no. 4, pp. 603-607, Oct. 2008.

[28] Haijian Zhang, Wen Yang, Jiayu Chen, and Hong Sun, "Improved Classification of Polarimetric SAR Data Based on Four-component Scattering Model," in *International Conference on Radar, 2006. CIE '06*, 2006, pp. 1-4.

[29] J. S. Lee, D. L. Schuler, T. L. Ainsworth, and W.-M. Boerner, "Polarization orientation estimation and applications: a review," in *Geoscience and Remote Sensing Symposium, 2003. IGARSS '03. Proceedings. 2003 IEEE International*, 2003, vol. 1, pp. 428- 430 vol.1.

APPENDIX I

7.6. Basis matrices for each scattering mechanism

7.6.1. Surface scattering

It consists of a first order Bragg surface scatterer modelling [6] from slightly rough surface in which the cross-polarized component is negligible. The scattering matrix for single bounce or surface scattering is given by

$$[S_s] = \begin{bmatrix} R_H & 0 \\ 0 & R_V \end{bmatrix}$$

where R_H, R_V are the Fresnel reflection coefficients for horizontally and vertically polarized wave, given by

$$R_H = \frac{\cos \theta_i - \sqrt{\varepsilon_r - \sin^2 \theta_i}}{\cos \theta_i + \sqrt{\varepsilon_r - \sin^2 \theta_i}} \ , \quad R_V = \frac{(\varepsilon_r - 1) - \left(\sin^2 \theta_i - \varepsilon_r(1 + \sin^2 \theta_i)\right)}{\left(\varepsilon_r \cos \theta_i + \sqrt{\varepsilon_r - \sin^2 \theta_i}\right)^2}$$

Here θ_i represents the incidence angle and ε_r represents the relative dielectric constant of the scattering surface.

In case of the urban scatterers, similar scattering matrix is used for representing the odd bounce scattering which involves single bounce and triple bounce scattering. The single bounce scattering is observed from the building roofs and vertical walls. The trihedral structures formed by wall-ground-wall exhibit triple bounce scattering. These two scattering mechanisms can be modelled together as odd bounce scattering which is represented by following scattering matrix.

$$[S_{odd}] = \begin{bmatrix} b & 0 \\ 0 & 1 \end{bmatrix}$$

where b represents the ratio of the HH and VV backscatter.

The coherency matrix obtained from the above scattering matrix is given by

$$\langle [T_s] \rangle = \begin{bmatrix} 1 & \beta^* & 0 \\ \beta & |\beta|^2 & 0 \\ 0 & 0 & 0 \end{bmatrix} , \quad \text{where } \beta = \frac{R_H - R_V}{R_H + R_V} \text{ and } |\beta| < 1$$

Here, $\langle \, \rangle$ represents the average over the whole data.

7.6.2. Double bounce scattering

This type of scattering behaviour is displayed by a dihedral corner reflector such as ground-tree trunk backscatter [6]. For double bounce scattering mechanism,

$$[S_d] = \begin{bmatrix} e^{2j\gamma_H} R_{GH} R_{TH} & 0 \\ 0 & e^{2j\gamma_V} R_{GV} R_{TV} \end{bmatrix}$$

where R_{GH}, R_{TH} and R_{GV}, R_{TV} represents the reflection coefficients of the ground and tree trunk surface for horizontal and vertical polarization. This model is generalized by incorporating propagation factors $e^{2j\gamma_H}$, $e^{2j\gamma_V}$, where the complex coefficients γ_H and γ_V represent any propagation attenuation and phase change effects [7].

The coherency matrices is given by

$$\langle [T_d] \rangle = \begin{bmatrix} |\alpha|^2 & \alpha & 0 \\ \alpha^* & 1 & 0 \\ 0 & 0 & 0 \end{bmatrix} , \quad \text{where } \alpha = \frac{e^{2j\gamma_H} R_{TH} R_{GH} + e^{2j\gamma_V} R_{TV} R_{GV}}{e^{2j\gamma_H} R_{TH} R_{GH} - e^{2j\gamma_V} R_{TV} R_{GV}} \quad \text{and } |\alpha| < 1$$

7.6.3.   Volume scattering

Volume scattering mechanism corresponds to the multiple scattering processes occurring within a medium such as vegetation or forest canopy. This scattering is modelled by considering the vegetation canopy as a cloud of randomly oriented thin cylinder like scatterers [6]. For volume scattering mechanism,

$$[S_v] = \begin{bmatrix} S_H & 0 \\ 0 & S_V \end{bmatrix}$$

where S_H and S_V are the complex scattering coefficients.

Assuming that the scatterers are randomly oriented about the radar look direction with an angle θ from the vertical, the scattering matrix from a particular scatterer can be found out by rotating into a coordinate system with vertical along the scatterer's standard orientation. The scattered field can be estimated by rotating back to the radar coordinate system.

$$\begin{bmatrix} S_{HH} & S_{HV} \\ S_{VH} & S_{VV} \end{bmatrix} = \begin{bmatrix} \cos\theta & -\sin\theta \\ \sin\theta & \cos\theta \end{bmatrix} S \begin{bmatrix} \cos\theta & \sin\theta \\ -\sin\theta & \cos\theta \end{bmatrix}$$

$$\begin{bmatrix} S_{HH} & S_{HV} \\ S_{VH} & S_{VV} \end{bmatrix} = \begin{bmatrix} S_H \cos^2\theta + S_V \sin^2\theta & (S_H - S_V)\cos\theta\sin\theta \\ (S_H - S_V)\cos\theta\sin\theta & S_H \sin^2\theta + S_V \cos^2\theta \end{bmatrix}$$

The probability density function describing the scatterer's orientation is $p(\theta)$. The expected value of any function $f(\theta)$ is given by

$$\langle f \rangle = \int_0^{2\pi} f(\theta)\, p(\theta)\, d\theta$$

Therefore, the covariance matrix statistics are

$$|S_{HH}|^2 = I_1|S_H|^2 + 2I_2 \text{Re}(S_H S_V{}^*) + I_3|S_V|^2$$
$$|S_{VV}|^2 = I_1|S_V|^2 + 2I_2 \text{Re}(S_H S_V{}^*) + I_3|S_H|^2$$
$$|S_{HV}|^2 = I_2|S_H|^2 - 2I_2 \text{Re}(S_H S_V{}^*) + I_2|S_V|^2$$
$$\langle S_{HH} S_{VV}{}^* \rangle = (I_1 + I_3)\text{Re}(S_H S_V{}^*) + I_2(|S_H|^2 + |S_V|^2) + \iota(I_1 - I_3)\text{Im}(S_H S_V{}^*)$$
$$\langle S_{HH} S_{HV}{}^* \rangle = I_4(|S_H|^2 - S_H S_V{}^*) + I_5(S_V S_H{}^* - |S_V|^2)$$
$$\langle S_{HV} S_{VV}{}^* \rangle = I_4(S_H S_V{}^* - |S_V|^2) + I_5(|S_H|^2 - S_V S_H{}^*)$$

where,

$$I_1 = \int_0^{2\pi} \cos^4\theta\, p(\theta)\, d\theta$$

$$I_2 = \int_0^{2\pi} \cos^2\theta \sin^2\theta\, p(\theta)\, d\theta$$

$$I_3 = \int_0^{2\pi} \sin^4\theta\, p(\theta)\, d\theta$$

$$I_4 = \int_0^{2\pi} \cos^3\theta \sin\theta\, p(\theta)\, d\theta$$

$$I_5 = \int_0^{2\pi} \cos\theta \sin^3\theta\, p(\theta)\, d\theta$$

The coherency matrix $[T]$ can be derived from the covariance matrix $[C]$ by using following relation

$$[T] = [A] \times [C] \times [A^T]$$

where $[A]$ is a similarity transformation matrix given by

$$[A] = \begin{bmatrix} \dfrac{1}{\sqrt{2}} & \dfrac{1}{\sqrt{2}} & 0 \\ 0 & 0 & 1 \\ \dfrac{1}{\sqrt{2}} & -\dfrac{1}{\sqrt{2}} & 0 \end{bmatrix}$$

The coherency matrix for volume scattering obtained from above method is given by

$$[T_v] = \begin{bmatrix} 2 & 0 & 0 \\ 0 & 1 & 0 \\ 0 & 0 & 1 \end{bmatrix}$$

7.6.4. Helix scattering

This type of scattering behaviour is observed from the complex shapes of the man-made structures and sharp targets [8]. A complete circular polarised return is generated from a set of four dipoles oriented at an angle of 45° with a spacing of λ/8 wavelength in the range direction or a pair of dihedral corner reflectors oriented at 45° with a spacing of λ/4 wavelength in the range direction. A left handed and a right handed circular polarization are generated by a helix target. The corresponding scattering matrices are

$$[S_{lh}] = \frac{1}{2}\begin{bmatrix} 1 & j \\ j & -1 \end{bmatrix} \quad , \quad [S_{rh}] = \frac{1}{2}\begin{bmatrix} 1 & -j \\ -j & -1 \end{bmatrix}$$

where $[S_{lh}]$ and $[S_{rh}]$ represent the left handed and the right handed scattering matrix. This can also be written as

$$[S_h] = \begin{bmatrix} 1 & \pm j \\ \pm j & -1 \end{bmatrix}$$

The corresponding coherency matrix is given by

$$\langle[T_h]\rangle = \frac{1}{2}\begin{bmatrix} 0 & 0 & 0 \\ 0 & 1 & \pm j \\ 0 & \mp j & 1 \end{bmatrix}$$

7.6.5. Wire scattering

The edges of the buildings and other structures in urban areas contribute to the wire scattering component [27]. Wire scattering is modelled from the response of thin wire or dipole target describes by the function of the orientation angle about the radar line of sight. For wire scattering mechanism,

$$[S_w] = \begin{bmatrix} \gamma & \rho \\ \rho & 1 \end{bmatrix}, \text{ where } \gamma = \frac{S_{HH}}{S_{VV}}, \ \rho = \frac{S_{HV}}{S_{VV}}$$

$$\langle[T_w]\rangle = \frac{1}{2}\begin{bmatrix} |\gamma + 1|^2 & (\gamma + 1)(\gamma - 1)^* & 2(\gamma + 1)\rho^* \\ (\gamma - 1)(\gamma + 1)^* & |\gamma - 1|^2 & 2(\gamma - 1)\rho^* \\ 2(\gamma + 1)^*\rho & 2\rho(\gamma - 1)^* & 4|\rho|^2 \end{bmatrix}$$

7.7. Direct Multiple Component Scattering Model Decomposition

The Multiple Component Scattering Model describes the total backscatter as a linear combination of the five elementary scattering mechanisms - surface, double bounce, volume, helix and wire scattering. The coherency matrix $[T]$ obtained from the fully polarimetric data can be expressed as a weighted sum of the elementary coherency matrices representing each scattering mechanism.

$$[T] = f_s [T_s] + f_d[T_d] + f_v [T_v] + f_h[T_h] + f_w [T_w]$$

where $[T_s], [T_d], [T_v], [T_h], [T_w]$ are the individual coherency matrices of the five scattering mechanisms. Here, f_s, f_d, f_v, f_h, f_w represent the expansion coefficients for each scattering component.

By substituting the values from equations, following expression is obtained.

$$[T] = f_s \begin{bmatrix} 1 & \beta^* & 0 \\ \beta & |\beta|^2 & 0 \\ 0 & 0 & 0 \end{bmatrix} + f_d \begin{bmatrix} |\alpha|^2 & \alpha & 0 \\ \alpha^* & 1 & 0 \\ 0 & 0 & 0 \end{bmatrix} + \frac{f_v}{4} \begin{bmatrix} 2 & 0 & 0 \\ 0 & 1 & 0 \\ 0 & 0 & 1 \end{bmatrix} + \frac{f_h}{2} \begin{bmatrix} 0 & 0 & 0 \\ 0 & 1 & \pm j \\ 0 & \mp j & 1 \end{bmatrix}$$

$$+ \frac{f_w}{2} \begin{bmatrix} |\gamma + 1|^2 & (\gamma + 1)(\gamma - 1)^* & 2(\gamma + 1)\rho^* \\ (\gamma - 1)(\gamma + 1)^* & |\gamma - 1|^2 & 2(\gamma - 1)\rho^* \\ 2(\gamma + 1)^*\rho & 2\rho(\gamma - 1)^* & 4|\rho|^2 \end{bmatrix}$$

Comparing the individual elements of the matrices, following equations are obtained

$$[T_{11}] = f_s + f_d|\alpha|^2 + \frac{f_v}{2} + \frac{f_w}{2}|\gamma + 1|^2$$

$$[T_{22}] = f_s|\beta|^2 + f_d + \frac{f_v}{4} + \frac{f_h}{2} + \frac{f_w}{2}|\gamma - 1|^2$$

$$[T_{33}] = \frac{f_v}{4} + \frac{f_h}{2} + 2f_w|\rho|^2$$

$$[T_{12}] = f_s\beta^* + f_d\alpha + \frac{f_w}{2}(\gamma + 1)(\gamma - 1)^*$$

$$[T_{13}] = f_w(\gamma + 1)\rho^*$$

$$[T_{23}] = \pm j\frac{f_h}{2} + f_w(\gamma - 1)\rho^*$$

The total backscattered power or the Span is given by the sum of the diagonal elements of the coherency matrix.

$$P = T_{11} + T_{22} + T_{33}$$

$$P = f_s(1 + |\beta|^2) + f_d(1 + |\alpha|^2) + f_v + f_h + f_w(1 + |\gamma|^2 + 2|\rho|^2)$$

The individual scattering powers for the five scattering mechanisms can be obtained from the above equation as

$$P_s = f_s(1 + |\beta|^2)$$
$$P_d = f_d(1 + |\alpha|^2)$$
$$P_v = f_v$$
$$P_h = f_h$$
$$P_w = f_w(1 + |\gamma|^2 + 2|\rho|^2)$$

The expansion coefficients for each scattering mechanism can be obtained by solving the equations

$$f_h = 2\,Im(T_{23}) \text{ and } f_w = \frac{Re(T_{23})}{(\gamma - 1)\rho^*}$$

$$P_h = f_h \text{ and } P_w = \frac{Re(T_{23})}{(\gamma - 1)\rho^*}(1 + |\gamma|^2 + 2|\rho|^2)$$

The volume scattering power is determined depending upon the magnitude balance of the copolarized component HH verses VV

$$10\,\log\left[\frac{\langle|S_{VV}|^2\rangle}{\langle|S_{HH}|^2\rangle}\right] \implies 10\,\log\left[\frac{T_{11} + T_{22} - 2Re(T_{12})}{T_{11} + T_{22} + 2Re(T_{12})}\right]$$

For $10\log(\langle|S_{VV}|^2\rangle/\langle|S_{HH}|^2\rangle) < -2dB$

$$\langle[T_v]\rangle = \frac{1}{30} \begin{bmatrix} 15 & 5 & 0 \\ 5 & 7 & 0 \\ 0 & 0 & 8 \end{bmatrix}$$

For $-2dB < 10\log(\langle|S_{VV}|^2\rangle/\langle|S_{HH}|^2\rangle) < 2dB$

$$\langle[T_v]\rangle = \frac{1}{4} \begin{bmatrix} 2 & 0 & 0 \\ 0 & 1 & 0 \\ 0 & 0 & 1 \end{bmatrix}$$

For $10\log(\langle|S_{VV}|^2\rangle/\langle|S_{HH}|^2\rangle) > 2dB$

$$\langle [T_v] \rangle = \frac{1}{30} \begin{bmatrix} 15 & -5 & 0 \\ -5 & 7 & 0 \\ 0 & 0 & 8 \end{bmatrix}$$

Depending upon the coherency matrix used for the volume scattering model, P_v can be obtained from following expressions.

$P_v = 4T_{33} - 2P_h - 8f_w|\rho|^2$ or $P_v = \frac{15}{4}T_{33} - \frac{15}{8}P_h - \frac{15}{2}f_w|\rho|^2$

Once the helix, wire and volume scattering powers are known, the remaining equations containing the coefficients for surface and double bounce power can be written as

$$S = f_s + f_d|\alpha|^2 = T_{11} - \frac{P_v}{2} - \frac{f_w}{2}(|\gamma + 1|^2)$$

$$D = f_s|\beta|^2 + f_d = T_{22} - T_{33} - \frac{f_w}{2}(|\gamma - 1|^2 - 4|\rho|^2)$$

$$C = f_s\beta^* + f_d\alpha = T_{12} - \frac{f_w}{2}(\gamma + 1)(\gamma - 1)^*$$

The expression for D and C also changes according to the coherency matrix used for volume scattering. The surface scattering and the double bounce scattering power is estimated by using assumptions based on the sign of the $\text{Re}\langle S_{HH} S_{VV}^* \rangle$ term. In terms of coherency matrix elements, the $\text{Re}\langle S_{HH} S_{VV}^* \rangle$ term can be estimated from the expression

$C_0 = T_{11} - T_{22} - T_{33} + P_h$

If the surface scattering is dominant, then $\text{Re}\langle S_{HH} S_{VV}^* \rangle > 0$ i.e. $C_0 > 0$. In this case the double bounce scattering is considered to be negligible. Therefore, α is assumed to be zero. The values of S and C changes to $S = f_s$ and $C = f_s\beta^*$. The surface scattering power and the double bounce power is given by

$$P_s = f_s(1 + |\beta|^2) = S + \frac{|C|^2}{S}$$

$$P_d = f_d(1 + |\alpha|^2) = D - \frac{|C|^2}{S}$$

Similarly, if $Re\langle S_{HH} S_{VV}^* \rangle < 0$, then $\beta = 0$ (zero surface scattering), as the double bounce scattering is dominant. Therefore, the surface scattering power P_s and the double bounce scattering power P_d are estimated as

$$P_s = f_s(1 + |\beta|^2) = S - \frac{|C|^2}{D}$$

$$P_d = f_d(1 + |\alpha|^2) = D + \frac{|C|^2}{D}$$

In this way, all the five decomposed scattering power images are obtained.

APPENDIX II

Derivation of terms including γ and ρ

The coherency matrix is given by

$$[T] = \frac{1}{2}\begin{bmatrix} \langle |S_{HH} + S_{VV}|^2 \rangle & \langle (S_{HH} + S_{VV})(S_{HH}^* - S_{VV}^*) \rangle & 2\langle (S_{HH} + S_{VV})S_{HV}^* \rangle \\ \langle (S_{HH} - S_{VV})(S_{HH}^* + S_{VV}^*) \rangle & \langle |S_{HH} - S_{VV}|^2 \rangle & 2\langle (S_{HH} - S_{VV})S_{HV}^* \rangle \\ 2\langle S_{HV}(S_{HH}^* + S_{VV}^*) \rangle & 2\langle S_{HV}(S_{HH}^* - S_{VV}^*) \rangle & 4\langle S_{HV} S_{HV}^* \rangle \end{bmatrix}$$

On the basis of this matrix, following expressions can be derived

1. $2|S_{VV}|^2 = T_{11} + T_{22} - 2\text{Re}(T_{12})$

2. $|\gamma + 1|^2 = \dfrac{2T_{11}}{T_{11} + T_{22} - 2\text{Re}(T_{12})}$

   as $|\gamma + 1|^2 = \left|\dfrac{S_{HH}}{S_{VV}} + 1\right|^2 = \dfrac{|S_{HH} + S_{VV}|^2}{|S_{VV}|^2}$

3. $(\gamma - 1)\rho^* - \rho(\gamma - 1)^* = \dfrac{2\text{Im}(T_{13})}{T_{11} + T_{22} - 2\text{Re}(T_{12})}$

   as

   $(\gamma - 1)\rho^* - \rho(\gamma - 1)^* = \left(\dfrac{S_{HH}}{S_{VV}} - 1\right)\dfrac{S_{HV}^*}{S_{VV}} - \dfrac{S_{HV}}{S_{VV}}\left(\dfrac{S_{HH}}{S_{VV}} - 1\right)^* = \dfrac{(S_{HH} - S_{VV})S_{HV}^* - S_{HV}(S_{HH} - S_{VV})^*}{|S_{VV}|^2}$

   $$(\gamma - 1)\rho^* - \rho(\gamma - 1)^* = \dfrac{2\,\text{Im}\big((S_{HH} + S_{VV})S_{HV}^*\big)}{|S_{VV}|^2}$$

4. $(\gamma + 1)(\gamma - 1)^* = \dfrac{2T_{12}}{T_{11} + T_{22} - 2\text{Re}(T_{12})}$

   as $(\gamma + 1)(\gamma - 1)^* = \left(\dfrac{S_{HH}}{S_{VV}} + 1\right)\left(\dfrac{S_{HH}}{S_{VV}} - 1\right)^* = \dfrac{(S_{HH} + S_{VV})(S_{HH}^* - S_{VV}^*)}{|S_{VV}|^2}$

5. $(\gamma - 1)\rho^* = \dfrac{2T_{23}}{T_{11} + T_{22} - 2\text{Re}(T_{12})}$

   as $(\gamma - 1)\rho^* = \left(\dfrac{S_{HH}}{S_{VV}} - 1\right)\dfrac{S_{HV}^*}{S_{VV}} = \dfrac{2\big((S_{HH} - S_{VV})S_{HV}^*\big)}{|S_{VV}|^2}$

6. $(\gamma + 1)\rho^* = \dfrac{2T_{13}}{T_{11} + T_{22} - 2\text{Re}(T_{12})}$

   as $(\gamma + 1)\rho^* = \left(\dfrac{S_{HH}}{S_{VV}} + 1\right)\dfrac{S_{HV}^*}{S_{VV}} = \dfrac{2\big((S_{HH} + S_{VV})S_{HV}^*\big)}{|S_{VV}|^2}$

7. $(1 + |\gamma|^2 + 2|\rho|^2) = \dfrac{2(T_{11} + T_{22} + T_{33})}{T_{11} + T_{22} - 2\text{Re}(T_{12})}$

   as $(1 + |\gamma|^2 + 2|\rho|^2) = (1 + \left|\dfrac{S_{HH}}{S_{VV}}\right|^2 + 2\left|\dfrac{S_{HV}}{S_{VV}}\right|^2) = \dfrac{|S_{VV}|^2 + |S_{HH}|^2 + 2|S_{HV}|^2}{|S_{VV}|^2}$

8. $\dfrac{|\gamma - 1|^2 - 4|\rho|^2}{2} = \dfrac{T_{22} - 2T_{33}}{T_{11} + T_{22} - 2\text{Re}(T_{12})}$

   as $\dfrac{|\gamma - 1|^2 - 4|\rho|^2}{2} = \dfrac{1}{2}\left(\left|\dfrac{S_{HH}}{S_{VV}} - 1\right|^2 - 4\left|\dfrac{S_{HV}}{S_{VV}}\right|^2\right) = \dfrac{1}{2}\left(\dfrac{|S_{HH} - S_{VV}|^2 - 4|S_{HV}|^2}{|S_{VV}|^2}\right)$